

EFFECTS OF TRANSCATHETER
INTERVENTION ON HEMODYNAMICS OF
COARCTATION OF THE AORTA

EFFECTS OF TRANSCATHETER INTERVENTION ON
HEMODYNAMICS OF COARCTATION OF THE AORTA

BY

NAJMEH GHORBANI, M.A.Sc.

A THESIS

SUBMITTED TO THE DEPARTMENT OF MECHANICAL ENGINEERING

AND THE SCHOOL OF GRADUATE STUDIES

OF MCMASTER UNIVERSITY

IN PARTIAL FULFILMENT OF THE REQUIREMENTS

FOR THE DEGREE OF

MASTER OF APPLIED SCIENCE

© Copyright by Najmeh Ghorbani, January 2021

All Rights Reserved

Master of Applied Science (2021)
(Mechanical Engineering)

McMaster University
Hamilton, Ontario, Canada

TITLE: Effects of transcatheter intervention on hemodynamics of
coarctation of the aorta

AUTHOR: Najmeh Ghorbani
M.A.Sc. (Mechanical Engineering),
Isfahan University of Technology, Isfahan, Iran

SUPERVISOR: Dr. Zahra Keshavarz Motamed

NUMBER OF PAGES: xix, 127

Abstract

Coarctation of the aorta (CoA) is a congenital heart disease in which the aorta witnesses localized obstruction. CoA can be fatal if left untreated. Endovascular stenting of CoA is an attractive treatment of choice in adolescents and adults; however, it can be associated with problems like stent malapposition and inappropriate stent expansion. The main objective of this study is to investigate the effects of stent implantation on the hemodynamic factors in a patient with mild coarctation.

Computational fluid dynamics was utilized to illustrate the hemodynamic factors like velocity distribution, wall shear stress, and trans-coarctation pressure drop in pre- and post-intervention states. These factors were used to assess the success of stent deployment in this patient. Large Eddy Simulation (LES) model is employed in this work to provide detailed information on hemodynamics in patient-specific pre- and post-intervention geometries of the aorta. The results of an in-house lumped parameter code, in which its input parameters are obtained from patient-specific clinical data, were applied as the boundary conditions in this study.

Acknowledgements

First, I would like to thank Dr. Zahra Keshavarz Motamed for her supervision and financial support during my research. By working under her supervision, I learned patience and hard work to reach my goals. I learned a lot from her amazing scientific skills and tireless endeavors. Doing this research was not possible without her supports.

I am very honored to have Dr. Chan Y. Ching and Dr. Tohid Didar on my Master's defence committee. I have been very fortunate to have their invaluable comments, and patient guidance.

My special thanks go to the Department Chair, Dr. Marilyn Lightstone, for her time, help, and support. I also thank all the department staff, particularly Nicole McLean, Leslie Kocsis, John Colenbrander, and Rob Sluban, for all their help.

I would also like to thank my friends and colleagues at McMaster University for all their help, especially Reza Sadeghi, for helping me with my thesis. They gave me a valuable vision of this research area and helped me through my graduate study.

This work was supported by NSERC Discovery Grant (RGPIN-2017-05349) and NSERC CRD Grant (CRDPJ 537352 - 18). I also acknowledge Compute Canada (www.computecanada.ca) to provide resources, and Compute Canada technical support group for their guidance and consultation.

My sincere appreciation goes to my family. This work would not have been performed without their help and support. I especially thank my parents, Zeinab and Nourmohammad, for their unconditional love and encouragement. My warm gratitude goes to my beloved husband, Mahdi, for all his supports and kindness. I am extremely grateful to have my wonderful daughter, Sana, who always gives me incredible love and motivation.

NOMENCLATURE and ABBREVIATION

Nomenclature

| | |
|-------------|--|
| Re | Reynolds number |
| Co | Courant number |
| ρ | Density [kg/m ³] |
| μ | Dynamic viscosity [Pa.s] |
| V | Velocity [m/s] |
| P | Pressure [mmHg] |
| Q | Volumetric flow rate [m ³ /s] |
| A | Cross-section surface area [m ²] |
| θ | Angle [°] |
| \vec{A}_i | Face normal vector [m ²] |

| | |
|-------------|---|
| \vec{f}_i | Vector from the centroid of the cell to the centroid of the face [m] |
| \vec{c}_i | Vector from the centroid of the cell to the centroid of the adjacent cell [m] |
| y | Normal distance to the wall [m] |
| u_τ | Friction velocity [m/s] |
| ν | Kinematic viscosity [m ² /s] |
| τ_w | Wall shear stress [Pa] |
| T | Cardiac cycle period [s] |
| t | Time instant [s] |
| A_{Ao} | Total area of the aortic wall [m ²] |
| A_{mi} | Area of the <i>i</i> th mesh surface [m ²] |

Abbreviation

| | |
|------------|------------------------------|
| <i>CoA</i> | Coarctation of the aorta |
| <i>LES</i> | Large Eddy Simulation |
| <i>CFD</i> | Computational Fluid Dynamics |
| <i>LPM</i> | Lumped parameter modeling |

| | |
|-------------|---------------------------------|
| <i>ODEs</i> | Ordinary differential equations |
| <i>FSI</i> | Fluid-structure interaction |
| <i>cP</i> | Centipoise |
| <i>D</i> | Dimensional |
| <i>LBM</i> | Lattice Boltzmann method |
| <i>WSS</i> | Wall shear stress |
| <i>MRI</i> | Magnetic resonance imaging |
| <i>RANS</i> | Reynolds Averaged Navier-Stokes |
| <i>DNS</i> | Direct numerical simulation |
| <i>SGS</i> | Subgrid scales |
| <i>LDL</i> | Low-density lipoproteins |
| <i>TKE</i> | Turbulent kinetic energy |
| <i>LA</i> | Left atrium |
| <i>LV</i> | Left ventricle |
| <i>RA</i> | Right atrium |
| <i>RV</i> | Right ventricle |
| <i>MV</i> | Mitral valve |
| <i>AV</i> | Aortic valve |

| | |
|-----------------|---|
| <i>TV</i> | Tricuspid valve |
| <i>PV</i> | Pulmonary valve |
| <i>BCA</i> | Brachiocephalic artery |
| <i>LC</i> | Left common carotid artery |
| <i>LS</i> | Left subclavian artery |
| <i>DAo</i> | Descending Aorta |
| <i>CHD</i> | Congenital heart defects |
| <i>PDA</i> | Patent ductus arteriosus |
| <i>DE</i> | Doppler echocardiography |
| <i>BAV</i> | Bicuspid aortic valve |
| <i>CA</i> | Cardiac catheterization and angiography |
| <i>CT</i> | Computed tomography |
| <i>CMRI</i> | Cardiac magnetic resonance imaging |
| <i>PC – MRI</i> | Phase-contrast magnetic resonance imaging |
| <i>4D</i> | Four-dimensional |
| <i>BSA</i> | Body surface area |
| <i>TAWSS</i> | Time-averaged wall shear stress |
| <i>ECs</i> | Endothelial cells |

SA – TAWSS Spaced-averaged time-averaged wall shear stress

Contents

| | |
|---|------------|
| Abstract | iii |
| Acknowledgements | iv |
| NOMENCLATURE and ABBREVIATION | vi |
| List of Figures | xiv |
| List of Tables | xix |
| 1 Introduction and Problem Statement | 1 |
| 2 Literature Review | 3 |
| 2.1 Introduction | 3 |
| 2.2 Blood Rheology in CFD Models | 3 |
| 2.3 Boundary Condition in CFD Models | 7 |
| 2.3.1 Idealized Boundary Condition | 7 |
| 2.3.2 Patient-specific Boundary Condition | 11 |
| 2.4 CFD Modeling Techniques | 14 |
| 2.4.1 Modeling Techniques Using Laminar Flow Assumption | 15 |

| | | |
|----------|--|-----------|
| 2.4.2 | Modeling Techniques Using Turbulence Flow Assumption . . . | 17 |
| 2.5 | Summary | 23 |
| 3 | Clinical Background | 25 |
| 3.1 | The Heart and Circulatory System | 25 |
| 3.2 | Anatomy and Function of the Aorta | 29 |
| 3.3 | Coarctation of the Aorta | 31 |
| 3.3.1 | Definition and Prevalence | 31 |
| 3.3.2 | Pathogenesis | 33 |
| 3.3.3 | Various Types | 34 |
| 3.3.4 | Clinical Features | 36 |
| 3.3.5 | Diagnostic Principles | 37 |
| 3.3.6 | Methods of Treatment: Surgical Treatments | 39 |
| 3.3.7 | Methods of Treatment: Interventional Treatments | 43 |
| 3.4 | Summary | 44 |
| 4 | Modeling and Methodology | 45 |
| 4.1 | Patient-Specific Pre- and Post-intervention Geometries | 46 |
| 4.2 | Initial and Boundary Conditions | 49 |
| 4.3 | Meshing | 53 |
| 4.4 | Grid and Timestep Independence | 58 |
| 4.4.1 | Timestep Independence: Pre-intervention Case | 59 |
| 4.4.2 | Timestep Independence: Post-intervention Case | 61 |
| 4.4.3 | Grid Independence: Pre-intervention Case | 63 |
| 4.4.4 | Grid Independence: Post-intervention Case | 63 |

| | | |
|----------|---|------------|
| 4.5 | Summary | 68 |
| 5 | Results and Analysis | 72 |
| 5.1 | Velocity Distribution | 74 |
| 5.1.1 | Trans-plane Instantaneous Velocity Distribution | 74 |
| 5.1.2 | Instantaneous Blood Flow Streamline | 75 |
| 5.2 | Wall Shear Stress Distribution | 78 |
| 5.2.1 | Time-varying Spatial Distribution of Wall Shear Stress | 80 |
| 5.2.2 | Spatial Distribution of time-averaged Wall Shear Stress | 81 |
| 5.2.3 | Space-averaged Time-averaged Wall Shear Stress | 83 |
| 5.3 | Pressure Distribution | 85 |
| 5.3.1 | Trans-plane Time-varying Spatial Pressure Distribution | 86 |
| 5.3.2 | Maximum Trans-coarctation Pressure Gradient | 87 |
| 5.4 | Summary of Results | 89 |
| 6 | Conclusions and Recommendations | 90 |
| 6.1 | Conclusions | 90 |
| 6.2 | Limitations and Future work | 92 |
| A | Mesh Skewness and Orthogonal Quality | 94 |
| B | y^+ Distribution | 96 |
| C | Maximum Courant Number | 99 |
| | Bibliography | 101 |

List of Figures

| | | |
|-----|---|----|
| 2.1 | Inlet pulsatile velocity profile in the ascending aorta [2] | 8 |
| 2.2 | Schematic of flow pattern in the aorta during early systole (a), mid to late systole (b), and end systole and diastole (c) [2] | 11 |
| 3.1 | Schematic drawing of the systemic and pulmonary systems | 27 |
| 3.2 | Schematic cross-section view of the human heart, picture adapted from [123] | 28 |
| 3.3 | Pressure-volume diagram of the LV over one cardiac cycle | 29 |
| 3.4 | Pressure, volume, and flow changes in the aorta, left ventricle, and left atrium during one cardiac cycle [125] | 30 |
| 3.5 | Anatomy of the aorta and aortic arch branches, picture adapted from [129] | 32 |
| 3.6 | Pathogenesis of CoA: (a) bloodstream during fetal life in ductus arteriosus and aorta, (b)1 dilating the aortic isthmus, and bypassing the obstruction of the posterior shelf due to the increase in left ventricular output in late fetal life, (b)2 infantile/preductal coarctation type with patent ductus arteriosus caused by the failure in the dilation of the aortic isthmus in late fetal life, (c) closure of ductus arteriosus after birth, (d) formation of the juxtaductal coarctation due to failure in the involution of the posterior shelf [135] | 35 |
| 3.7 | CoA with (a) and without (b) PDA [135] | 36 |

| | | |
|------|---|----|
| 3.8 | Schematic of classic end-to-end anastomosis for surgical repair of CoA [145] | 40 |
| 3.9 | Schematic of extended end-to-end anastomosis for surgical repair of CoA: (a) incision for surgical repair, (b) repaired coarctation [145] | 41 |
| 3.10 | Schematic of patch graft aortoplasty repair for CoA: (a) site of the incision for patch graft aortoplasty shown by a dashed line, (b) incising the site of stenosis, (c) suturing prosthetic graft for patch aortoplasty [145] | 42 |
| 3.11 | Schematic of the subclavian flap aortoplasty for the treatment of CoA: (a) site of incision shown by a dashed line, (b) repaired coarctation by flap aortoplasty treatment [145] | 42 |
| 3.12 | A schematic of stent deployment for the treatment of the CoA: (a) insertion of a balloon catheter with a stent in the coarctation site, (b) balloon expansion for widening the obstruction, (c) balloon deflation and retrieving the catheter, picture adapted from [153] | 44 |
| 4.1 | Front view (a) and back view (b) of the patient's aortic geometries before the intervention - front view (c) and back view (d) of the patient's aortic geometries after the intervention using ANSYS Workbench 2020 R | 48 |
| 4.2 | Input flow boundary condition in pre-intervention case obtained from our in house LPM algorithm [60,41,59,63] | 50 |
| 4.3 | Input flow boundary condition in post-intervention case obtained from our in house LPM algorithm [60,41,59,63] | 51 |
| 4.4 | Schematic of input and output flow boundary conditions for pre-intervention (a) and post-intervention (b) cases | 52 |
| 4.5 | Meshing style used in pre- and post intervention geometries | 55 |
| 4.6 | Mesh skewness for mesh No.1 pre-intervention case | 57 |

| | | |
|------|---|----|
| 4.7 | Mesh orthogonal quality for mesh No.1 pre-intervention case | 57 |
| 4.8 | Meshing style used in pre- and post-intervention geometries | 58 |
| 4.9 | Simulation results of the TAWSS for the pre-intervention case using the coarse and fine timesteps | 60 |
| 4.10 | Simulation results of the velocity profile in two planes for the pre- intervention case using the coarse and fine timesteps | 62 |
| 4.11 | Simulation results of the TAWSS for the post-intervention case using the coarse and fine timesteps | 64 |
| 4.12 | Simulation results of the velocity profile in two planes for the post- intervention case using the coarse and fine timesteps | 65 |
| 4.13 | Simulation results of the TAWSS for the pre-intervention case using the coarse and fine grids | 66 |
| 4.14 | Simulation results of the velocity profile in two planes for the pre- intervention case using the coarse and fine grids | 67 |
| 4.15 | Simulation results of the TAWSS for the post-intervention case using the coarse and fine grids | 69 |
| 4.16 | Simulation results of the velocity profile in two planes for the post- intervention case using the coarse and fine grids | 70 |
| 5.1 | Simulation results of instantaneous velocity distribution in the longi- tudinal cutting plane for pre- and post-intervention states - velocity magnitude ranges from 0 to 1.5 ($\frac{m}{s}$) in all the images presented here. | 76 |
| 5.2 | Simulation results of instantaneous velocity streamlines in three various time instants for pre- and post-intervention states - velocity magnitude ranges from 0 to 1.5 ($\frac{m}{s}$) in all the images presented here. | 79 |

| | | |
|-----|---|----|
| 5.3 | Simulation results of WSS in three various time instants for pre- and post-intervention states – WSS magnitude ranges from 0 to 100 ($\frac{dyn}{cm^2}$) in all the images presented here. | 82 |
| 5.4 | Simulation results of a) TAWSS in the pre-intervention state, b) TAWSS in the post-intervention state, and c) spatial distribution of TAWSS in areas shown by dash lines for pre- and post-intervention states – WSS magnitude ranges from 0 to 50 ($\frac{dyn}{cm^2}$) in all the images presented here. | 84 |
| 5.5 | Simulation results of SA-TAWSS in ascending aorta, aortic arch, and descending aorta for pre- and post-intervention cases | 85 |
| 5.6 | Simulation results of instantaneous pressure distribution in in longitudinal cutting plane for pre- and post-intervention states - pressure magnitude ranges from 0 to 15 ($mmHg$) in early systole and peak systole, and from 0 to 10 ($mmHg$) in late systole | 88 |
| 5.7 | Simulation results for the pressure gradient across the coarctation site over a cardiac cycle for pre- and post-intervention cases | 89 |
| A.1 | Mesh Skewness for Pre-intervention Case, Mesh No. 2 | 94 |
| A.2 | Mesh Orthogonal Quality for Pre-intervention Case, Mesh No. 2 | 94 |
| A.3 | Mesh Skewness for Post-intervention Case, Mesh No. 1 | 95 |
| A.4 | Mesh Orthogonal Quality for post-intervention Case, Mesh No. 1 | 95 |
| A.5 | Mesh Skewness for Post-intervention Case, Mesh No. 2 | 95 |
| A.6 | Mesh Orthogonal Quality for post-intervention Case, Mesh No. 2 | 95 |
| B.1 | y+ Distribution for Pre-intervention state, Mesh No. 1, Time Step = 0.8E-6 s - y+ ranges from 0 to 1 in all the images presented here. | 97 |

| | | |
|-----|--|-----|
| B.2 | y_+ Distribution for Post-intervention state, Mesh No. 1, Time Step = 0.8E-6 s - y_+ ranges from 0 to 1 in all the images presented here. . . | 98 |
| C.1 | Maximum Courant Number for Pre-intervention state, Mesh No. 1, Time Step = 0.8E-6 s | 99 |
| C.2 | Maximum Courant Number for Post-intervention state, Mesh No. 1, Time Step = 0.8E-6 s | 100 |

List of Tables

| | | |
|-----|--|----|
| 2.1 | Review of the blood viscosity and density used in CFD simulations | 5 |
| 2.2 | Various phases of the cardiac cycle and their corresponding mechanical events, table adapted from [76] | 13 |
| 4.1 | Typical dimensions of the aorta in adults [3] | 47 |
| 4.2 | Surface areas and their corresponding diameter for boundaries in pre- and post-intervention | 49 |
| 4.3 | Percentage of the input volume flow rate exiting through outlets in pre- and post-intervention cases | 53 |
| 4.4 | Percentage of the input volume flow rate exiting through outlets in CFD studies | 53 |
| 4.5 | Characteristics of meshes resulted from discretizing the pre- and post-intervention geometries | 56 |
| 5.1 | Peak WSS in the aortic arch and branches in the pre-intervention, and post-intervention states in current study, as well as the typical values of WSS in a healthy thoracic aorta model (as reported in [4]) | 81 |

Chapter 1

Introduction and Problem Statement

Aorta is the largest arterial trunk in the body. It is responsible for delivering the blood from the ventricle to the branch arteries in order to supply the body organs with oxygen-rich blood. Aorta can be affected by diseases such as the tear in the innermost layer of the aorta (aortic dissection), abnormal bulging (aneurysm), plaque build-up in the inside wall (atherosclerosis), and abnormal narrowing (stenosis). Coarctation of the aorta (CoA), also known as aortic coarctation or aortic narrowing, is a congenital heart disease in which aorta witnesses localized constriction. Coarctation of the aorta can be fatal if left untreated. Although surgical resection of the CoA is a treatment of choice in neonates, infants, and young children, this method of treatment involves the risks associated with the invasive nature of the surgical procedure. Transcatheter treatment can be applied to older children and adults. Residual obstruction and post-surgical recoarctation associated with balloon angioplasty are issues that make the employment of endovascular stenting of CoA an attractive choice in adolescents and

adults. However, failure in stent deployment can occur due to problems like malaposition of the stent and inappropriate stent expansion. In this regard, Computational Fluid Dynamics (CFD) models can provide detailed spatio-temporal information on the blood flow that may be difficult, or even impossible, to capture by imaging modalities. This information can help assess the success or failure of stent deployment in patients with CoA, develop the patient-specific treatment strategies, and predict the timing of the intervention by monitoring the disease progression.

This study aims to investigate the effects of the intervention on a patient with repaired coarctation. To this aim, Large Eddy Simulation (LES) model is employed to provide detailed spatial and temporal information of blood flow in patient-specific geometries of the aorta before and after the intervention. The results of a unique lumped parameter modeling (LPM) code are used as the boundary conditions in both pre- and post-intervention cases to ensure applying the realistic boundary condition. The assumption of the rigid wall is considered in this thesis. This assumption is proved to be a realistic one in literature, especially in patients with CoA who are usually subject to hypertension and reduced compliance in the aorta.

Chapter 2

Literature Review

2.1 Introduction

This chapter aims to provide a literature review on the rheology of the blood, boundary condition, and modeling techniques used in existing CFD studies of the aorta. In this regard, the assumptions of Newtonian or non-Newtonian fluid for the blood simulation in literature will be discussed, and studies in which idealized boundary conditions were utilized are presented against those in which patient-specific boundary conditions were used. In addition, CFD studies with laminar flow assumption are mentioned alongside those with turbulence flow assumption.

2.2 Blood Rheology in CFD Models

Viscosity is defined as the fluid resistance to deformation. In Newtonian fluids, viscosity value can only be influenced by the temperature. So, at a constant temperature, the viscosity of a Newtonian fluid is constant. While, in a non-Newtonian fluid, the

viscosity value will change by altering the shear rate.

Blood contains cellular substances comprising red blood cells (erythrocytes), white blood cells (leukocytes), and platelets (thrombocytes) that are suspended in Plasma. Plasma is an aqueous polymer solution that includes electrolytes and organic molecules. Although plasma exhibit Newtonian behavior, the whole blood shows non-Newtonian physical property [1]. It is reported that the blood viscosity depends on two parameters: hematocrit, which is the volume percentage of red blood cells in the blood, and temperature [2]. The blood viscosity increases as a result of increasing the hematocrit or decreasing the temperature [2]. The blood non-Newtonian behavior results in the nonlinear relation between the shear stress and shear rate. Studies show the non-Newtonian blood flow behavior in vessels with an internal diameter of less than 1 mm. In contrast, in large arteries like the aorta, blood can be considered as a homogenous incompressible fluid with the Newtonian behavior [1, 3, 4, 5, 6].

There are some studies on the hemodynamics in the aorta with the assumption of non-Newtonian fluid. For example, Xu and colleagues investigated the influence of aortic valve disease on blood flow in the dilated aorta with this assumption in 2020 [7]. However, many of these works with the assumption of non-Newtonian blood rheology were done in small arteries [8, 9, 10, 11]. Table 2.1 shows the blood viscosity and density in some CFD models assuming the blood as a Newtonian fluid.

Table 2.1: Review of the blood viscosity and density used in CFD simulations

| <i>Author(s)</i> | <i>Reference Number</i> | <i>Blood Dynamic Viscosity (cP)</i> | <i>Blood Density (kg/m³)</i> | <i>Date of Publication</i> |
|--------------------------|-----------------------------|---|---|--------------------------------|
| Wood et al. | [12] | 4 | 1050 | 2001 |
| Leuprecht et al. | [13] | 3.65 | 1044 | 2003 |
| Morris et al. | [5] | 3.5 | 1050 | 2005 |
| Figueroa et al. | [14] | 4 | 1060 | 2006 |
| Gao et al. | [15] | 3.5 | 1050 | 2006 |
| Greve et al. | [16] | 4 | 1060 | 2006 |
| Spilker et al. | [17] | 4 | 1060 | 2007 |
| Paul et al. | [18] | 3.71 | 1060 | 2009 |
| Tan et al. | [19] | 2.56 | 1060 | 2009 |
| Cheng et al. | [20] | 4 | 1060 | 2010 |
| Wen et al. | [21] | 3.8 | 1121 | 2010 |
| Keshavarz-Motamed et al. | [22] | 3.5 | 1050 | 2011 |
| Lantz et al. | [23] | 2.56 | 1080 | 2011 |
| Stalder et al. | [24] | 4.5 | 1050 | 2011 |
| Brown, A. et al. | [25] | 3.5 | 1056 | 2012 |
| Lantz et al. | [26] | 3.5 | 1080 | 2012 |
| Midulla et al. | [27] | 4 | 1050 | 2012 |

Continued on the next page

Table 2.1–Continued from previous page

| <i>Author(s)</i> | <i>Reference Number</i> | <i>Blood Dynamic Viscosity (cP)</i> | <i>Blood Density (kg/m³)</i> | <i>Date of Publication</i> |
|--------------------------|-------------------------|-------------------------------------|---|----------------------------|
| Brown, S. | [4] | 3.9 | 1060 | 2013 |
| Keshavarz-Motamed et al. | [28] | 3.5 | 1050 | 2013 |
| Reymond et al. | [29] | 3.5 | 1000 | 2013 |
| Tse et al. | [30] | 3.71 | 1060 | 2013 |
| Sughimoto et al. | [31] | 4.9 | 1055 | 2014 |
| Callington et al. | [32] | 4 | 1060 | 2015 |
| Numata et al. | [33] | 4 | 1060 | 2016 |
| Feng et al. | [34] | 3.2 | 1005 | 2017 |
| Madhavan and Kemmerling | [35] | 4 | 1060 | 2018 |
| Romarowski et al. | [36] | 3.5 | 1060 | 2018 |
| Zakaria et al. | [37] | 4.2 | 1050 | 2019 |
| Bäumler et al. | [38] | 4 | 1060 | 2020 |
| Liang et al. | [39] | 3.5 | 1056 | 2020 |
| Pons et al. | [40] | 3.5 | 1050 | 2020 |
| Sadeghi et al. | [41] | 3.5 | 1050 | 2020 |
| Swanson et al. | [42] | 4 | 1060 | 2020 |

2.3 Boundary Condition in CFD Models

Cardiovascular system contains a huge closed loop of connected vessels; however, only a small area of this system is being considered for modeling the hemodynamics in the aorta. Therefore, applying the proper boundary conditions at the inlet (ascending aorta) and outlets (aortic arch branches and descending aorta) is of paramount importance to truly compensate the absent parts of the cardiovascular system in the mentioned simulation and plays a crucial role in CFD simulation results. The inlet velocity profile can be an idealized or generic one, or a time-varying patient-specific profile obtained from the imaging modalities [2]. The idealized velocity profile can be in the shape of a flat (plug) or a fully developed (parabolic) profile. The two following sub-sections summarize some CFD studies based on applying the idealized and patient-specific boundary condition.

2.3.1 Idealized Boundary Condition

The most preferred idealized inlet velocity boundary condition in the ascending aorta used in the literature is the combination of spatial plug profile and temporal waveform pattern. The data obtained from the experiment reported in [43] is generally utilized for forming the pulsatile waveform. Figure 2.1 shows the accelerating, decelerating, reversed, and no-flow parts of the pulsatile velocity waveform. Several in vivo studies performed using the hot-film anemometry can be referred to as the verification of the tendency of the blood flow in ascending aorta to shape a flat velocity profile [44, 45].

Flat velocity profiles have been used in many studies as the boundary condition in CFD simulations. Mori and Yamaguchi [46] imposed the flat inlet velocity profile to investigate the hemodynamics in the aortic arch. Kim and colleagues [47] applied

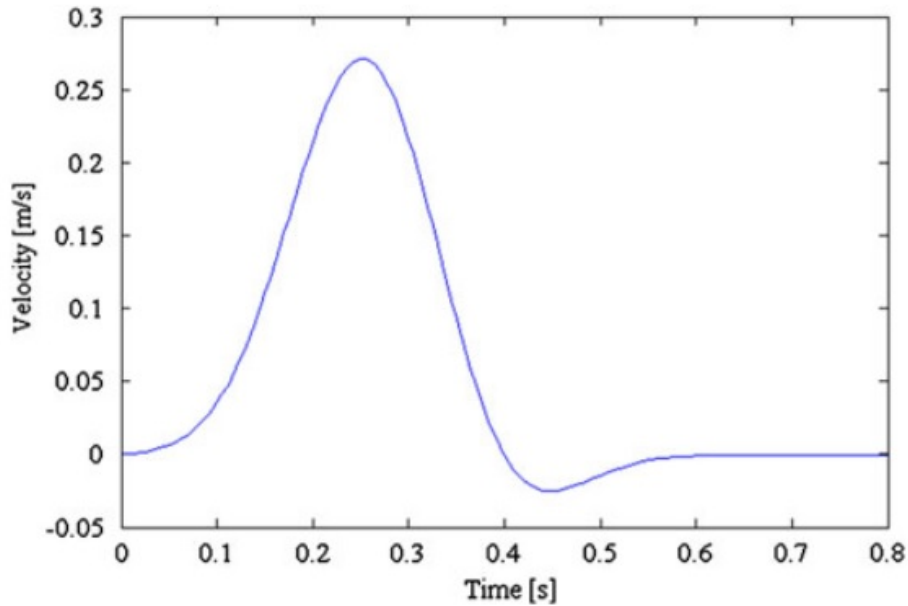


Figure 2.1: Inlet pulsatile velocity profile in the ascending aorta [2]

the uniform inlet velocity profile using the waveform presented in [43]. Cheng and co-workers [48] used the flat velocity profile at the inlet of the computational domain. They obtained the velocity waveform based on the patient’s cine phase-contrast MRI data.

To investigate the effects of the interaction of the computational domain and the heart non-invasively, lumped parameter models are utilized to couple the reduced-order heart models as inlet boundary conditions in the simulation. These models use the patient-specific clinical data as the input parameters to solve the ordinary differential equations (ODEs) and show the global characteristics of the heart. They are referred to as 0D models as they are predicting the global time-varying flow and pressure changes by solving ODEs. Some researchers studies on global hemodynamics using LPM for healthy and pathological cases. Segers and co-workers, in a series of studies [49, 50, 51], utilized the LPM to investigate the global blood hemodynamics

in the human cardiac system. This approach was also used by Garcia and colleagues in 2005 [52], and by Tanné and co-workers in 2008 [53]. Lantz and colleagues [23] studied the effects of the rigid and fluid-structure interaction (FSI) model of the aortic wall on the hemodynamic parameters using the LPM coupled to the outflow boundaries. Alongside studies on healthy and pathological cases like aortic stenosis, LPM technique has also been utilized to study the coarctation of the aorta in some of the scientific works. Engvall et al. in 1991 [54] and 1994 [55] investigated the influence of arterial stenosis on global hemodynamics using LPM. Kim et al. [56] in 2009 coupled a lumped parameter heart model and a 3D finite element model of the patient's aorta. They declared that they could obtain the physiologically realistic pressure and flow of the aorta. They used the LPM as the inflow boundary condition and could assess the aortic hemodynamics via the coupled models. Alimohammadi et al. [57] employed the Windkessel model to the boundaries of the computational domain. They utilized invasive patient-specific pressure measurements to tune the Windkessel parameters. Keshavarz-Motamed and colleagues used LPM to assess the cardiovascular hemodynamics in their studies extensively [58, 59, 60, 28, 61, 62, 63, 64, 65, 41, 66, 67]. Their works contain studies on the global and local hemodynamics of the heart and circulatory system in pathological conditions like mixed valvular diseases, coarctation of the aorta, aortic aneurysm, valve replacement, and ventricular diseases. In 2013, Coogan et al. [68] investigated the importance of aortic coarctation and hypoplasia to measure the cardiac workload. Coogan et al. [69] also reported another study on the effects of various aortic arch obstructions on the ventricular workload using LPM. In 2017, Mínguez et al. [70] employed a lumped parameter model of the fetal circulation to assess the hemodynamic alterations in fetuses with coarctation

of the aorta to improve the diagnosis of this disease. Recently, Sadeghi et al. [41] in 2020 used the results of LPM as the input flow boundary condition to model the aortic hemodynamics in the patient aorta using Lattice Boltzmann method (LBM). They developed the fast non-invasive model of coupled lumped parameter network and computational framework to quantify the local and global hemodynamics of the coarctation of the aorta. Mirramezani and Shaden [71] proposed a distributed lumped parameter modeling framework to quantify the global hemodynamic characteristics efficiently in the current year. They compare the results of their framework with that of the CFD simulation results and found good agreement in terms of flow rate and pressure distribution for various hemodynamic conditions and vascular geometries. As the lumped parameter modeling solves the ODEs, they have less computational and time costs, and thus, they are easier to utilize than the conventional CFD models.

The other form of the inlet boundary condition is time-varying pressure waveforms obtained from catheter data. Park and co-workers applied the inlet profile of cardiac pressure in their study [72]. In another work, pulsatile pressure was used in the inlet boundary by Vasava and colleagues to model the idealized human aortic arch [73]. This type of boundary condition is less frequently applied in the literature. The reason may be due to the high sensitivity of the blood flow rate to the pressure gradient between the inlet and the outlets in a way that a small error in the applied pressure gradient leads to a high deviation of the blood flow rate from the realistic values [2]. It is reported that catheter data acquisition is associated with errors like catheter whip artifact, which is the excessive oscillation of the catheter tip resulting from blood flow, that make this type of inlet boundary condition challenging to implement [2].

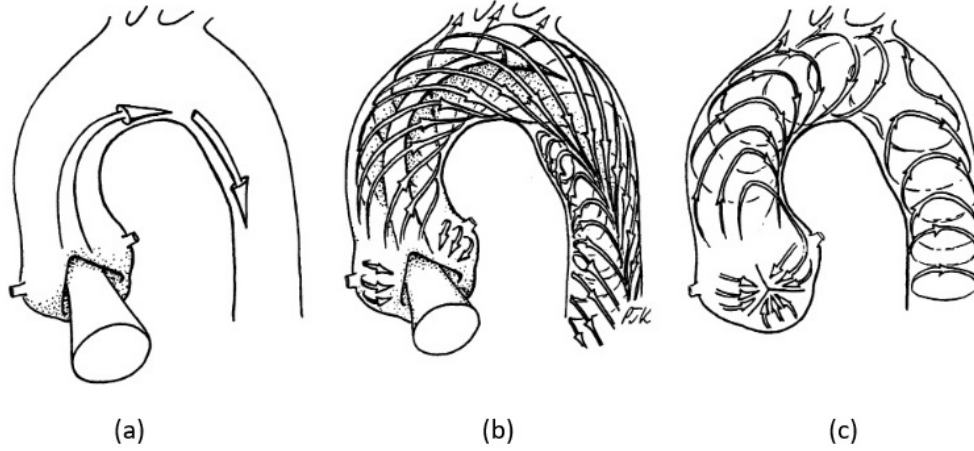


Figure 2.2: Schematic of flow pattern in the aorta during early systole (a), mid to late systole (b), and end systole and diastole (c) [2]

2.3.2 Patient-specific Boundary Condition

Although idealized boundary conditions have been utilized in many studies to investigate the aortic hemodynamics, the exact nature of the spatial velocity profile in the aorta exhibits a complex time-varying 3D pattern. Figure 2.2 illustrated the development of the flow pattern in a healthy aorta during the cardiac cycle. As shown in this figure, the blood flow during early systole shows an axial pattern. Then, the flow pattern exhibits the helical shapes in the mid to late systolic phase. Finally, this pattern turns into the complex flow recirculation during the end systole and diastole. It is hypothesized that various factors contribute to the formation of the helical flow pattern during the mid to late systole: 1) arrangement of the muscle fibers resulting in counterclockwise torsional deformation of the LV during systole, and then clockwise return during diastole; 2) asymmetric shape of the aortic valve leaflets and their opening and closure; and 3) the non-planar arterial geometry and its curvature. [2]

Different mechanical events in the heart cause various phases during the cardiac

cycle. These phases and their corresponding events are described in Table 2.2. As these events make the inlet velocity profile to deviate from the idealized profile, some studies compared the influence of assuming the idealized inlet flow boundary conditions on the simulation results with that of using the realistic boundary conditions. In 2009, Renner and colleagues compared the result of wall shear stress (WSS) distribution in nine healthy subjects using the subject-specific inlet velocity profile measured through MRI with that of using flat profile considering subject specific mass flow rate [74]. Their findings indicated that using measured subject specific boundary conditions is a must as the results of WSS distribution using this boundary condition differed between 8-34% in their cases with that of the flat velocity profile. They also indicated that the minimum difference in the WSS between the two mentioned boundary conditions was seen in the peak velocity in the cardiac cycle. In another work, Morbiducci and co-workers [75] investigated the effects of inlet velocity profile assumptions on WSS distribution and flow structure. They compared the CFD modeling results using the inlet subject-specific 3D velocity profile obtained from Phase-contrast magnetic resonance imaging (MRI) data with that of using the inlet axial or idealized velocity profile. The results of their work show that imposing the axial inlet velocity profile may capture accurate WSS distribution; however, helical flow structures are highly influenced by the boundary condition assumptions. They concluded that enough attention should be considered while setting the idealized or axial MRI inlet velocity profile as the input boundary condition.

Recently, Pirola and colleagues [77] presented a methodology for hemodynamic simulation of aortic dissection using fully patient-specific boundary condition. They used 4D flow MRI and Doppler-wire pressure measurements for pre- and post-operation

Table 2.2: Various phases of the cardiac cycle and their corresponding mechanical events, table adapted from [76]

| <i>Phase of cardiac cycle</i> | <i>Mechanical event</i> |
|-------------------------------|---|
| End diastole | Atrial contraction |
| Early systole | Isovolumic ventricular contraction, tricuspid motion towards right atrium |
| Mid-systole | Atrial relaxation |
| Late systole | Systolic filling of atrium |
| Early diastole | Early ventricular filling |

cases to specify the patient-specific boundary conditions. More recently, Xu et al. [7] in 2020 extracted time-varying velocity vectors, including the trans-plane normal and in-plane tangential velocity components from patient-specific MRI data. They utilized this patient-specific data as the aortic inlet velocity boundary condition in their work. To insert this velocity profile into the mesh model of the aorta, they applied an in-house code written in MATLAB. They also imposed the volumetric flow rate waveforms obtained from patient's MRI data for each of the aortic arch branches, and Neumann type free outflow boundary condition in the descending aorta. They declared that although the results of the outflow rate at the descending aorta were available via MRI data, they preferred to use the mentioned boundary condition because: 1) Neumann type free outflow boundary condition can absorb potential numerical errors while the Dirichlet boundary conditions are applied on the inlet and three outlet branches, and 2) under in vivo condition, the wall deformation causes the aortic model to tolerate the phase lag between the input flow waveform and the

summation of output flow waveforms, while in their computational model, the aortic wall was assumed to be rigid, and thus this assumption makes this model unable to tolerate the mentioned lag.

As discussed above, some studies mentioned the importance of using the patient-specific boundary conditions in CFD simulation results. However, patient's data acquisition contains challenges like the limitations, pitfalls, and the invasive nature of some of the imaging modalities and clinical tools that hinder utilizing patient-specific boundary conditions to apply in many case studies. The next chapter will shed more light on the pros and cons of imaging modalities used to assess the coarctation of the aorta. In addition, the descending aorta, where the coarctation site of the present study is located, is reported to be less sensitive to the inlet velocity profile [77].

2.4 CFD Modeling Techniques

Improvements in the imaging techniques have enabled researchers to investigate the hemodynamics in the aorta. An *in vivo* feasibility study of the turbulent blood flow in the aorta was first performed by Stein and Sabbah in 1976 [78]. They employed the catheter-tip hot-film velocity probe to measure instantaneous point velocity in the ascending aorta in seven healthy cases and eight patients. In their study, the maximum Reynolds numbers were between 5,700 and 10,000 during peak ejection in normal cases, while the blood flow showed turbulence behavior in almost the whole ejection period in each of the patients [78]. Despite the sufficient spatial resolution and frequency response of the hot film anemometry, the invasive direction-sensitive nature of this technique encouraged researchers to use the Doppler ultrasound imaging technique [79]. Segadal and Matre investigated the blood velocity profile in the

human ascending aorta using a Doppler ultrasound in 1987 [80]. Magnetic resonance technique has been widely used for the flow assessment in the aorta [81, 82, 83]; however, this imaging technique is associated with some complications such as producing artifacts caused by the implanted metal stent and the need for long breath-holding. More details on various imaging modalities used for assessing hemodynamic properties in the aorta and their pros and cons will be provided in chapter 3. In addition, ex vivo studies [84, 85], as well as in vitro [86] experiments have been performed to provide researchers with a better understanding of the vascular blood flow; however, these models might not accurately represent the in vivo patient-specific criteria. They are also expensive and demanding [87].

Different CFD modeling techniques have been employed to compensate for the limitations and pitfalls of imaging techniques, as well as ex vivo and in vitro studies mentioned above. These techniques have been utilized to study the hemodynamics in the aorta ranging from models with laminar flow assumption to turbulent ones. A review on these techniques will be presented in the following sections.

2.4.1 Modeling Techniques Using Laminar Flow Assumption

Reynolds number ($\rho u D / \mu$), which represents the ratio of the inertial forces (ρu^2) to the viscous forces ($\mu u / D$) is a dimensionless parameter used to specify the flow regime. In this number, ρ , u , D , and μ represent the density, velocity, length scale, and dynamic viscosity, respectively. To study the blood flow in the aorta, D is the arterial diameter. The velocity value used in determining the Reynolds number is the mean velocity value (i.e., volume flux divided by cross-sectional pipe area) [88]. However, in arteries with the unsteady flow, the occurrence of the flow disturbances

near peak velocity makes the determination of the peak Reynolds number based on the peak velocity reasonable [89]. In low Reynolds numbers, i.e. $Re < 2300$, the viscous forces are dominant, and the flow is laminar. It is reported that in large arteries, the blood flow is assumed to be laminar in both steady and unsteady flow conditions as the mean flow velocity is low enough to result in a low Reynolds number [2]. It has also been reported that although the turbulence takes place at the peak flow velocity, laminar flow is seen in the rest of the cardiac cycle [4], justifying the adoption of laminar flow assumption in the hemodynamic modeling of the aorta in literature.

In 2005, Morris et al. applied the laminar flow assumption in three different reconstructed geometries of the aorta to study the influence of these models on aortic hemodynamics [5]. Park et al. [72] in 2007 presented the pseudo-organ boundary conditions in their laminar computational modeling of the blood dynamics in the aorta. In 2012, Gallo and colleagues [90] investigated a hemodynamic study of the aortic blood flow in the human aorta using laminar flow assumption. They employed the 4D phase-contrast MRI to acquire the subject-specific geometry and flow rate boundary conditions. They used Fluent code (ANSYS Inc., USA) to solve the governing equations in the finite volume method. Laminar flow assumption was also adopted in the work of Morbiducci et al. [75] in 2013. They declared that they did not apply the turbulence model in their study, even knowing the occurrence of transitional flow regimes in the aorta. Pirola and co-workers [91] assumed the laminar flow in their patient-specific model of the aorta to investigate the effects of various out-flow boundary conditions on the simulation results compared with the PC-MRI data. Recently, Pirola et al. [77] studied the hemodynamics in aortic dissection, pre- and post-operation cases, using laminar flow assumption and patient-specific boundary

condition obtained from 4D flow MRI. In addition to the studies mentioned above, there exist other studies on the aortic hemodynamics using laminar flow assumption in the literature [20, 92, 93, 94], underscoring the prevalence of adopting this assumption on numerical simulations mainly with the aim of reducing the computational costs.

2.4.2 Modeling Techniques Using Turbulence Flow Assumption

Despite the occurrence of laminar flow in small arteries, turbulence can take place in large arteries like the aorta [4]. The occurrence of turbulent blood flow in the human aorta is of paramount importance as it may cause various pathophysiological effects [78] like the influence of turbulent blood flow on the onset of the platelet deposition [95], hemolysis, and endothelial damage [79, 96].

“A strict definition of turbulent flow is elusive” [78]; however, it is defined (as reported in [74]) by Hinze as “motion in an irregular condition of flow in which the various quantities show a random variation with time and space coordinates so that statistically significant average values can be discerned.” [97] and by Robertson and Herrick as “Turbulence is an irregular eddying motion in which velocity and pressure perturbations occur about their mean values; these perturbations are irregular or random, even chaotic, in time and space with components extending smoothly over an extensive continuous hierarchy of scales or frequencies so that they must be characterized by statistical means” [98].

Reynolds number is generally used for characterizing the transition from laminar to turbulence aortic flow in mammals [99]. The critical Reynolds number for the

occurrence of the transition of a steady flow in a smooth straight pipe is between 2,300 and 4000 [2]. Critical Reynolds number, at which the flow transition from laminar to turbulent occurs, can be affected by the flow and geometrical characteristics. Pulsatile nature of blood flow in the aorta can affect the critical Reynolds number; however, this effect is not fully understood. Some studies report the higher critical Reynolds number in a steady Poiseuille flow than in a pulsating flow upon the same mean pressure gradient [100], while the others consider the pulsating flow more stable than the steady Poiseuille flow [101]. Also, it has been reported that pulsatility decreases the critical Reynolds number to 400 in a circular tube, even without obstruction during the deceleration phase [87]. It is also documented that obstruction in the pipe decreases the critical Reynolds number. Thus, the turbulence flow can be observed in lower Reynolds numbers in the presence of coarctation [78]. It has been concluded from experiments that the critical Reynolds number can be reduced to 1000 in the presence of flow disturbance like occlusion [26]. Another study reports the rise in the possibility of turbulence flow in the presence of arterial stenosis [102]. As a result, it is believed that turbulence models might be the best choice for modeling the aortic hemodynamics [2, 103, 104].

Reynolds Averaged Navier-Stokes (RANS) equations were employed in the first turbulence models. Since a time-averaged solution for the flow is provided by these equations, they do not require high computational resources to run. They also can provide information on the mean flow properties, e.g., mean flow wall shear stress. WSS provided by CFD models acts as an indicator for predicting aneurysm rupture, thrombus formation, and disease progression [105]. More details on the concept and application of WSS will be presented in the following chapters.

Ghalichi and colleagues in 1998 investigated the flow in a pipe with the coarctation indexes of 0.5, 0.75, and 0.86 using Wilcox low-Re $k-\omega$ turbulence model [106]. They employed a steady flow assumption in their work. They justified this assumption by indicating that blood flow during the diastolic phase, which occurs approximately over 75% of the whole cardiac cycle, is relatively constant. They reported that the transitional or turbulent flow could take place after the obstruction, even in mild stenosis. In 2003, Varghese and Frankel [107] employed FLUENT code to solve the pulsatile flow in stenotic vessels. They used four different turbulence models: low Reynolds number $k-\omega$ turbulence model, low and high Reynolds number versions of the renormalization-group theory $k-\epsilon$ model, and the standard $k-\epsilon$ model. They found that the first-mentioned model was in better agreement with the experimental measurements than the other three turbulence models. Ryval et al. [108] studied pulsatile flow in a stenosed tube using Wilcox's $k-\omega$ model In 2004. They chose this model as they believed in its ability to predict the laminar, transitional, and turbulent regimes. In 2009, Xiao and Zhang [87] applied the low Reynolds number $k-\omega$ turbulence model to investigate the effects of geometry on arterial hemodynamics in a cardiac cycle. One year later, Menter's Shear Stress Transport (SST) turbulence model, which is a combination of $k-\omega$ turbulence model used in the inner region of the boundary layer and $k-\epsilon$ model used in the free shear flow, was applied by Cheng et al. [20] using ANSYS CFX. They studied hemodynamics in a patient with aortic dissection and found the qualitative agreement between the WSS distribution of the laminar flow simulation and that of the turbulence model; however, the results of WSS using the turbulence model showed remarkably higher magnitude than that of the laminar flow assumption. SST was also applied by Benim and colleagues [109] in

2011 to study the aortic hemodynamics in an idealized geometry. In this year, Lantz et al. [23] also applied SST model to study the WSS in a subject-specific human aorta. In the same year, Keshavarz-Motamed et al. [22] performed the experimental, numerical, and mathematical study on the hemodynamics of the human aorta in the presence of coexisting models of bicuspid aortic stenosis and coarctation of the aorta. For the experimental study, they investigated the MRI measurements in an in vitro flow model to obtain the instantaneous flow rates. Numerical study was performed using finite volume method and the transitional $k - \omega$ turbulence model. Left ventricular and aortic pressure and stroke work were obtained using LPM in their study. In another work, Keshavarze-Motamed et al. [28] employed $k - \omega$ model to investigate the effects of bicuspid aortic valve on the coarctation of the aorta in vitro.

Despite the ability of RANS models in providing the time-averaged hemodynamics, it lacks the dynamic behavior of complex blood flow in the aorta. It is because the pulsatility of the blood flow, as well as the relatively low Reynolds number, prevent the blood flow in the aorta from the well-developed high-Reynolds-number turbulent flow, while RANS models are well suited for the last mentioned flow [102]. On the other hand, direct numerical simulation (DNS) provides all the spatio-temporal information of the flow; however, they are restricted to simple geometries and require high computational resources. Large eddy simulation (LES), which is a scale-resolving turbulence model, might be more appropriate to model the aortic hemodynamics as it has finer resolution compared with RANS models and less required computational resources compared with the DNS model [2, 102]. In the LES approach, which lies

between DNS and RANS models, only large eddies are resolved temporally and spatially. These large eddies are energy-containing scales separated by explicitly filtering the Navier-Stokes equations from the subgrid scales (SGS) that are required to be modeled [110]. The rise of the computational cost with the increase of the Reynolds number is the limitation of the LES model, restricting the application of this model to moderately high Reynolds number turbulent flows. However, the Reynolds number of blood flow in the aorta is around $O(10^4)$, leading to affordable computational costs using the LES model [102].

LES model was first employed to study the flow behavior in idealized geometries. In 2001, Mittal and colleagues [102] studied the pulsatile flow behavior in a modeled arterial stenosis using the LES model. Their model of stenosis contained a one-sided 50% obstruction in a planar channel. They used the LES model to simulate the flow dynamics resulted from the varied time-varying sinusoidal boundary flux. They discussed the potential implementation of vortex shedding for non-invasive diagnosis of arterial obstruction. They tried to show the ability of the LES model in studying the hemodynamics in arteries. In 2008, Varghese et al. [111] investigated the ability of a host of turbulence models, including LES, to predict the flow behavior through an eccentric stenosed pipe. Their findings indicated the more promising results of the LES model for accurate prediction of the transitional stenotic flows. One year later, Paul et al. [18] reported the study of pulsatile blood flow using the LES model in a 3D model of the stenosed artery. Their findings show the importance of using the LES approach in modeling the blood flow. In another study, Tan and co-workers [112] in 2011 compared the ability of the LES model and RANS models in predicting the transitional flow in the 75% stenosed axisymmetric experimental model of the artery

as well as in an eccentric stenosed model. The results demonstrated the power of LES methods in predicting the transitional flow in a stenosed pipe. Another study was performed in 2015 by Gaedhagen et al. [113] studied the hemodynamics in a generic model of the aorta with CoA and post stenotic dilation. They considered the pulsatile inlet velocity profile in their study. Their focus was on the role of hemodynamics in the successful CoA repair. They indicated that flow disturbances or direct jet impingement on the vessel wall might lead to the post stenotic dilatation.

In 2012, Lantz and colleagues [26] applied the LES model to measure the hemodynamics in a subject specific human aorta. They employed MRI to take the geometry and velocity boundary condition in their study. They found high WSS near the aortic arch branches, while low WSS values were observed in the inner curvature of the descending aorta in their research. In the same year, Lantz et al. [114] investigated the relationship between the WSS and low-density lipoproteins (LDL) surface concentration. It is documented that the increased LDL concentration on the arterial wall promotes the accumulation of cholesterol in the intima later of large arteries [115, 116]. They found that WSS and LDL surface concentration correlate in a way that wall regions with low WSS correspond to areas of high LDL surface concentration and vice versa. One year later, Lantz et al. [117] compared the results of numerical analysis using the LES model with the MRI data in a 63-year old female patient with CoA before and after the catheter intervention. Balloon angioplasty without stent deployment was performed to dilate the coarctation in this patient. A good qualitative and quantitative agreement was found between the CFD results and MRI measurements for turbulent kinetic energy (TKE). Their finding indicated that even with the increase of Reynolds number and flow rate, the total TKE decreased

after the intervention. They found that the flow jet formed at the site of the coarctation was weaker after the intervention. In 2015, Andersson et al. [118] derived the patient-specific geometry and flow conditions from MRI data to study the pulsatile flow by LES method in a CoA patient. They investigated the TKE and flow eccentricity in pre- and several virtual follow-up intervention cases. These evaluations can help to assess the severity of the coarctation through MRI measurements. They found the inverse asymptotic correlation between the total value of TKE and the degree of dilation of the coarctation. They indicated that with the combination of MRI and CFD frameworks, it could be possible to provide a platform for improving the patient-specific CoA therapy. In 2016, Motamed et al. [60] developed a CFD model using the LES and LPM framework by studying 34 patients with mild coarctation of the aorta to investigate the effects of the transcatheter intervention on left ventricular function and aortic hemodynamics. Hemodynamic assessment in human aorta via CFD simulations have been performed in other works like in [119] with the FSI model and in [41] using the Lattice Boltzmann method (LBM). However, limitations of imaging modalities, in vivo measurements, and CFD techniques make it challenging to obtain the fully patient-specific data of the hemodynamics in the human aorta for clinical applications.

2.5 Summary

This chapter was aimed to present a review on the blood rheology, boundary condition, and modeling techniques in CFD studies in the literature. It can be concluded from the literature that: (1) considering the blood as a homogenous incompressible fluid with the Newtonian behavior is a reasonable assumption in large arteries like

aorta, (2) patient-specific geometry, as well as time-varying patient-specific boundary conditions are required to obtain realistic results through modeling the hemodynamics of the patient's aorta, (3) LES, is a suitable approach in terms of computational costs and accuracy to predict the turbulence flow in the human aorta.

Chapter 3

Clinical Background

The objective of this chapter is to provide readers with some background information on the biological aspect of this study. First, the function of the heart and circulatory system are explained, and the cardiac cycle and its various phases are illustrated. Next, the anatomy and function of the aorta are discussed in brief. Then, the coarctation of the aorta is defined, and pathogenesis and various types of this disease are explained. Finally, the current treatments for the coarctation of the aorta and their advantages and risks are described briefly.

3.1 The Heart and Circulatory System

Blood circulatory system and lymphatic system are two main circulatory systems in the human body. They are responsible for transferring dissolved or suspended substances in the liquid from one part of the human body to another part through vessels. In the blood circulatory system, blood is transported from the heart to the capillaries through the arterial system. In contrast, the venous system is responsible for carrying

the blood from the capillaries to the heart. The blood circulatory system comprises three types: systemic circulation, pulmonary circulation, and portal system. The first two mentioned systems need the heart as a pump to push the blood. The systemic system can be divided into two parts: the systemic arterial system, which carries oxygenated blood from the heart to the body organs, and systemic venous system, which carries deoxygenated blood from organs to the heart. The pulmonary system consists of two parts: pulmonary arterial system in which deoxygenated blood is carried from the heart to the lungs, and pulmonary venous system in which oxygenated blood is transferred from the lungs to the heart. In the portal system, specific vascular channels are responsible for carrying the substances by connecting two capillary systems. A schematic illustration of the systemic and pulmonary systems is presented in Figure 3.1. [120]

The heart receives the blood through systemic and pulmonary venous systems and pumps the blood through systemic and pulmonary arterial systems, shown in Figure 3.2. The heart has four chambers: left atrium (LA), left ventricle (LV), right atrium (RA), and right ventricle (RV). On the left side of the heart, LA receives the oxygen-rich blood from the lungs through the pulmonary veins and ejects the blood to the LV through the mitral valve (MV). Then, LV pumps the oxygen-rich blood to the body organs through the aortic valve (AV) and Aorta. On the right side of the heart, returning deoxygenated blood from the body organs fills the RA through vena cava and travels through the tricuspid valve (TV) to the RV. Next, the deoxygenated blood leaves the RV to the pulmonary artery by crossing the pulmonary valve (PV).

The cardiac cycle describes the changes that happen during every heartbeat [121]. A single cardiac cycle consists of two phases: systole and diastole. In the systolic

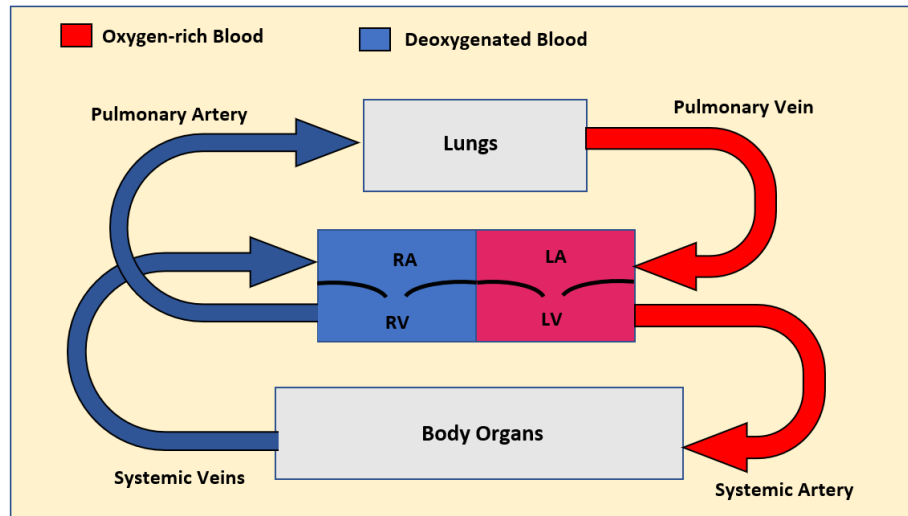


Figure 3.1: Schematic drawing of the systemic and pulmonary systems

phase, the contraction of heart muscles pumps the blood out of the heart, while during the diastolic phase, the blood refills the heart when the heart muscles are relaxed. Figure 3.3 shows the pressure-volume loop of the LV in a cardiac cycle. This diagram can display the ventricular function. However, the shape of the pressure-volume loop may alter with changes in parameters such as myocardial compliance, and valvular and myocardial diseases [122]. Mechanical events that occur in the left ventricle are in correlation with points and stages in the pressure-volume loop of the left ventricle. These events are described in the following.

As illustrated in Figure 3.3, the opening of the MV (point A) in the diastolic phase (filling stage) makes the filling of the LV with the blood from LA possible.

In the rapid-filling phase, the elastic recoil of the ventricle exerts suction and cause pressure to fall. This stage continues by the slow-filling phase (diastasis) in which the pressure increases due to the venous pressure. Then, the atrial contraction fills the ventricle until reaching to the mitral valve closure (point B). [124]

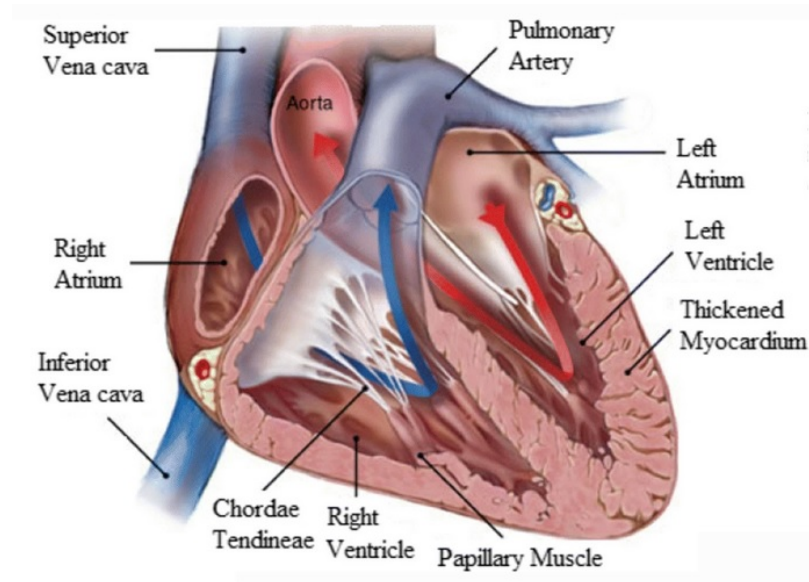


Figure 3.2: Schematic cross-section view of the human heart, picture adapted from [123]

The systolic phase begins with the closure of the MV (point B). In this stage, isovolumic contraction occurs while both AV and MV are closed. The increase in the pressure happens as a result of the contraction of the ventricular muscles [4]. At the end of this stage, the ventricular wall tension reaches the highest value right before the opening of the AV [122].

The opening of the AV (point C) occurs when the blood pressure in the LV reaches that of the artery. In this stage, LV ejects the blood to the aorta, and the blood volume in the LV decreases to reach the point in which AV closes (point D). This point is the end of the systolic phase. Point D is the start of the diastolic phase when the muscles of the LV start to relax. Since both of the AV and MV are closed, no change in the blood volume in the left ventricle occurs. Diastolic phase continues by the pilling phase (point A to point B) as described above.

Figure 3.4 provides more information on the pressure, volume, and velocity changes versus time in the LV, aorta, and LA. As shown in this figure, the blood velocity in the

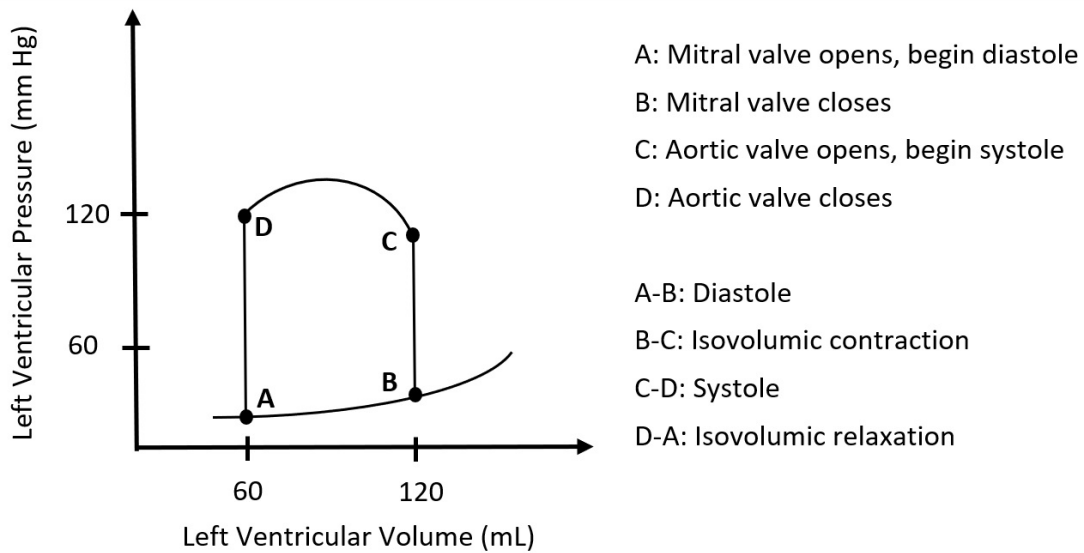


Figure 3.3: Pressure-volume diagram of the LV over one cardiac cycle

aorta first increases in the ejection stage, and then roughly decreases until reaching the isovolumic relaxation stage. While the oscillation in the aortic blood velocity can be seen at the end of the ejection phase in Figure 3.4, other references such as [121] reported similar oscillations in the blood velocity of the aorta even in the isovolumic relaxation and isovolumic contraction stages.

3.2 Anatomy and Function of the Aorta

Aorta is the largest artery in the human body. It is responsible for supplying the oxygenated blood from the left ventricle to the systemic arterial system. It starts from the aortic valve and goes through the abdomen up to the start of the bifurcation of the common iliac arteries [126]. Aorta can be divided into the thoracic and abdominal aorta. Thoracic aorta consists of four parts: aortic root, ascending aorta, aortic arch, and descending aorta. Abdominal aorta comprises suprarenal and infrarenal

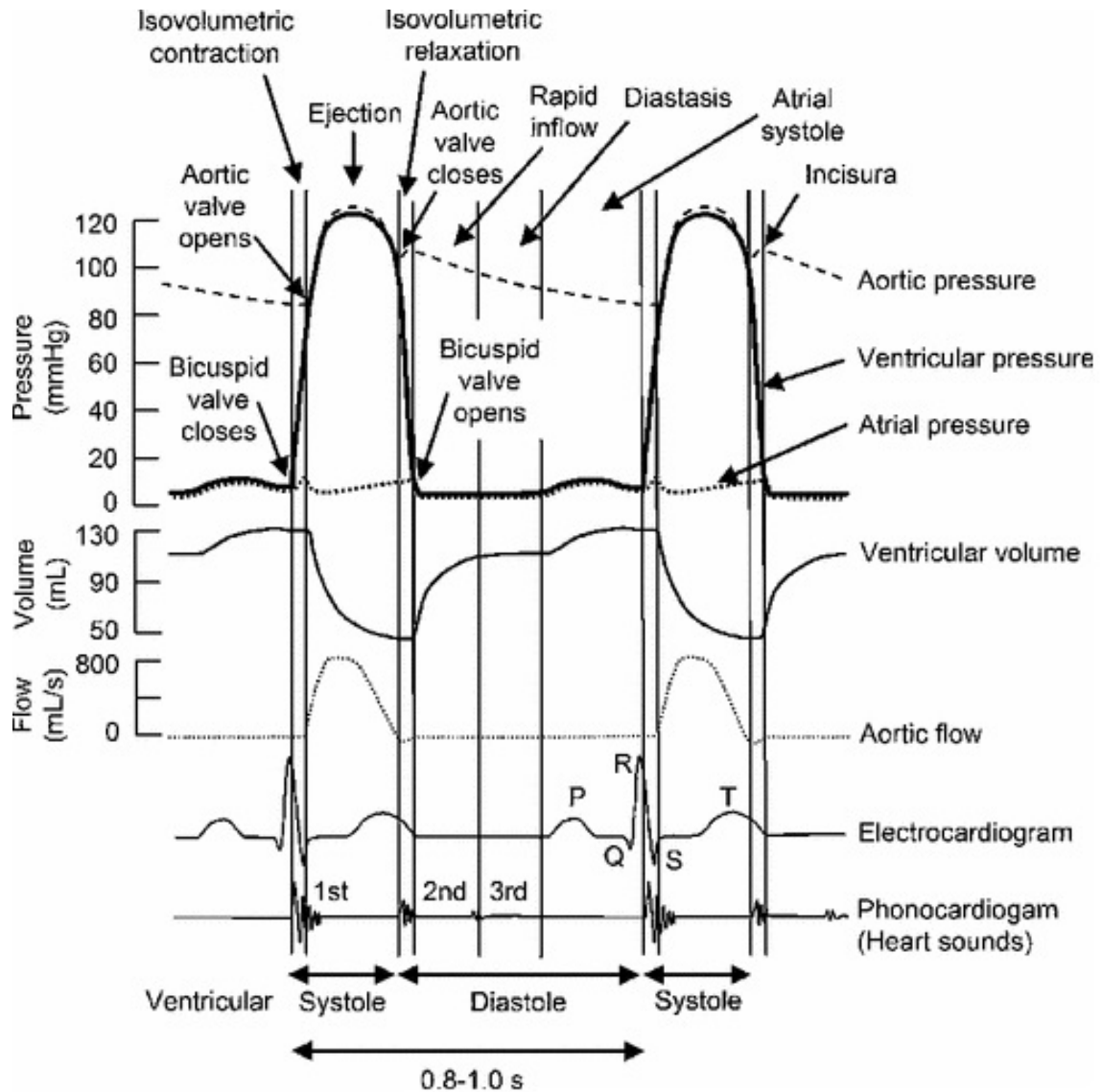


Figure 3.4: Pressure, volume, and flow changes in the aorta, left ventricle, and left atrium during one cardiac cycle [125]

parts [127]. The aortic valve is the starting point of the aortic root, and coronary arteries branch off the aortic root to supply the cardiac muscles with oxygen-rich blood. Ascending aorta starts from the sinotubular junction, which is a boundary that separates the aortic root from the tubular ascending aorta, and ends just prior to the ostium of the brachiocephalic artery (BCA) [127]. The aortic arch starts from the ostium of the brachiocephalic artery and extends to the isthmus [127]. Isthmus of the aorta is the final part of the aortic arch. It gets its name from the narrowing (isthmus) of this part caused by a reduced bloodstream in fetal life. Descending aorta denotes the part of the aorta which begins from distal to the isthmus and expands to the diaphragm. Anatomy of the aorta and aortic arch branches is shown in Figure 3.5.

3.3 Coarctation of the Aorta

Considering the importance of the aorta in supplying the body organs with oxygen-rich blood, malfunctioning of the aorta can be fatal. Coarctation of the aorta is among the aortic diseases that influence the function of the aorta. This section aims to give some information on the coarctation of the aorta, as a congenital heart disease, including its definition, pathogenesis, various types, clinical features, diagnostic principles, and current treatments.

3.3.1 Definition and Prevalence

Congenital heart defects (CHD) are among the most prevalent conditions of birth defects, with an abundance of around 1% of all live births [128]. Coarctation of the aorta (CoA), also known as aortic coarctation or aortic narrowing, is a congenital

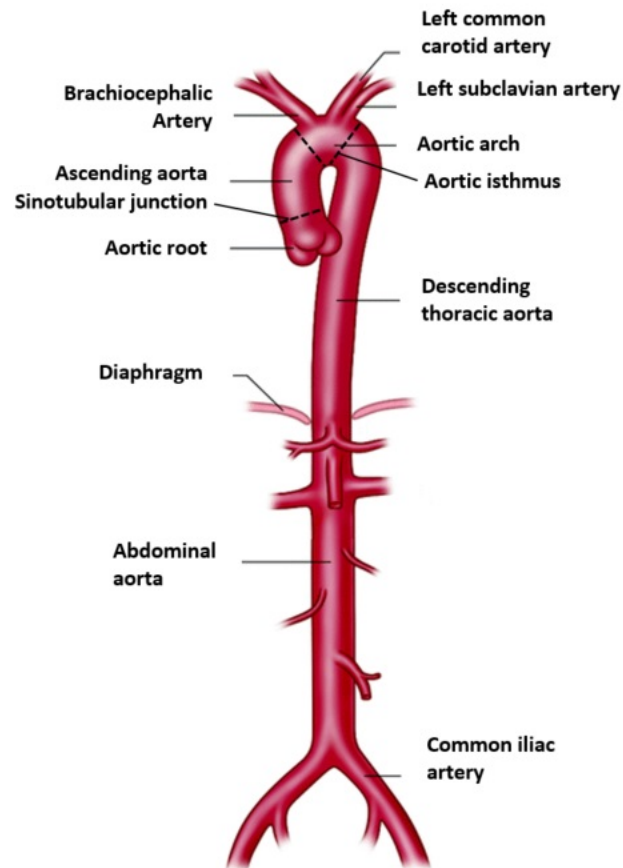


Figure 3.5: Anatomy of the aorta and aortic arch branches, picture adapted from [129]

heart disease whereby ascending aorta, aortic arch, descending aorta, or abdominal aorta witnesses localized constriction. However, the most prevalent site of the presence of CoA is distal to the ostium of the left subclavian artery at the location of ductus arteriosus. It is reported that CoA is commonplace between 5% and 8% among the whole CHD [130, 131, 132, 133].

3.3.2 Pathogenesis

During fetal life, it is not air but amniotic fluid which fills the non-functioning lungs. During this time, oxygenating the blood occurs in the placenta prior to returning to the body. A tiny blood vessel called Ductus arteriosus serves as a connection between the trunk of the pulmonary artery and descending aorta, allowing the oxygenated blood from the right ventricle to bypass the lungs and enter the aorta. Within the first three months after birth, the closure of the lumen of ductus arteriosus turns it into the ligamentum arteriosum, which is a narrow tissue. Patent ductus arteriosus (PDA) is a condition in which ductus arteriosus fails to close after birth. [134]

Despite considerable research on the CoA, the pathogenesis of this disease is not fully understood. However, two classical theories are trying to explain this phenomenon: (1) ductus tissue theory of CoA, and (2) Hemodynamic theory of CoA. These two theories are related to the function of ductus arteriosus. The first theory explains that the CoA is the result of the contraction of the smooth aortic wall muscle that occurs alongside the closure of the ductus arteriosus. The result of this procedure is the tubular contraction of the aortic arch and ascending aorta. The second theory aims to explain the CoA using the hemodynamic pattern during fetal life. At this time, posterior aortic shelf, which is located in front of the orifice of the ductus arteriosus, divides the ductal bloodstream into two parts: cephalad stream that supplies the head and arms by passing through the rather hypoplastic aortic isthmus, and descending stream that transfers the blood to the lower extremities by passing through the descending aorta. Figure 3.6 (a) shows these two bloodstreams via arrows. During late fetal life, the output of the LV increases, which results in the dilation of the aortic isthmus and bypassing the obstruction of the posterior aortic

shelf (Figure 3.6 (b)1). Failure in the dilation of the aortic isthmus leads to preductal coarctation in infants. This type of coarctation is often accompanied by the patent ductus arteriosus (PDA) (Figure 3.6 (b)2). By the expansion of lungs after birth, pulmonary vascular resistance decreases, and systemic vascular resistance rises. These changes result in the closure of ductus arteriosus and turn this trunk into the ligamentum arteriosus (Figure 3.6 (c)). Failure in the involution of the posterior shelf results in a juxtaductal coarctation of the aorta shown in Figure 3.6 (d). This type of CoA can be seen with and without PDA, as shown in Figure 3.7. [135]

3.3.3 Various Types

Various types of the coarctation of the aorta can be classified in two ways: based on the location of the coarctation, and based on the severity of the coarctation. Regarding the classification of CoA based on its location, three different types of coarctation can be considered: (1) preductal type in which coarctation can be seen in the aortic arch and ascending aorta, (2) juxtaductal coarctation wherein the coarctation occurs near the location of ductus arteriosus, and (3) postductal coarctation in which the coarctation is distal to the site of the ductus arteriosus. Coarctation of the aorta can also be categorized in terms of the severity of the obstruction. In this classification method, the coarctation index is defined as the ratio of aortic diameter at the coarctation site to that of at the normal site. In this way, the coarctation severity can be considered as mild, moderate, or severe for the coarctation index of more than 0.65, between 0.5 and 0.65, or less than 0.5, respectively. [136]

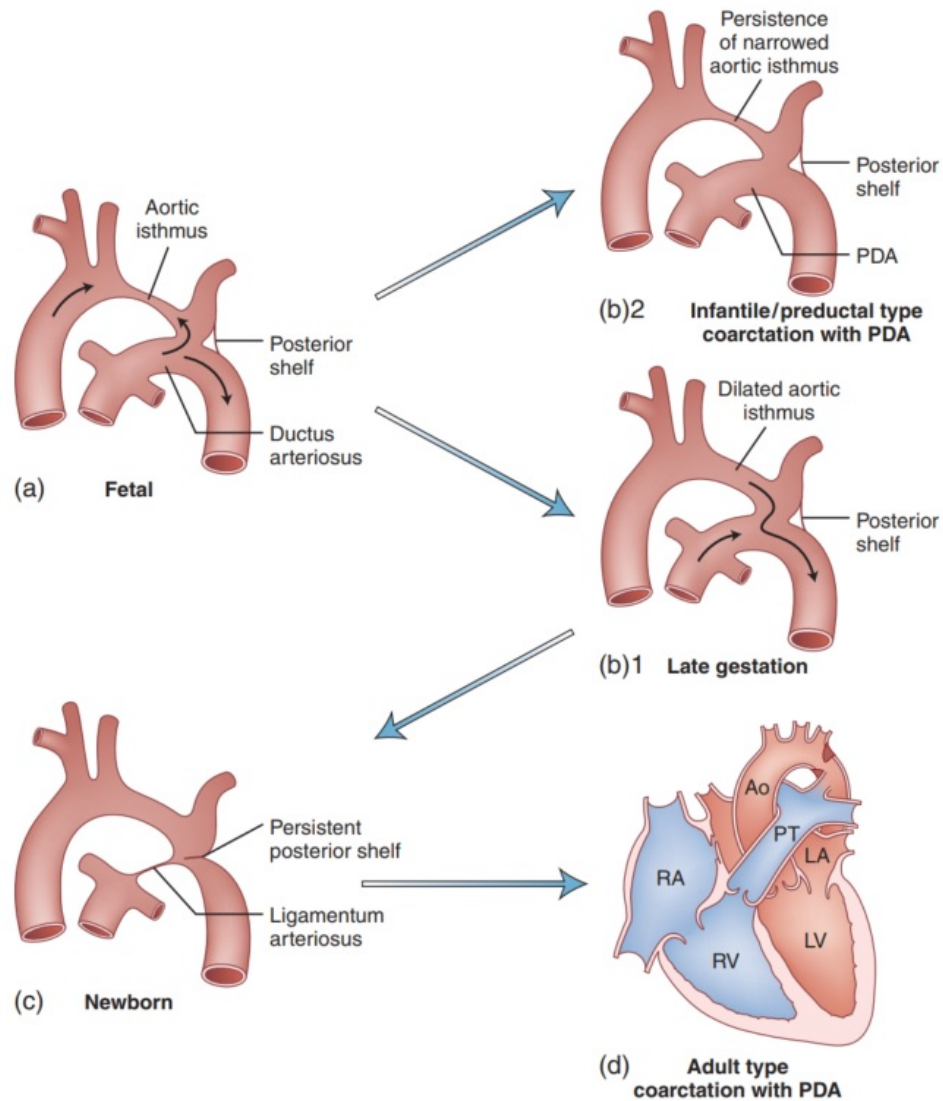


Figure 3.6: Pathogenesis of CoA: (a) bloodstream during fetal life in ductus arteriosus and aorta, (b)1 dilating the aortic isthmus, and bypassing the obstruction of the posterior shelf due to the increase in left ventricular output in late fetal life, (b)2 infantile/preductal coarctation type with patent ductus arteriosus caused by the failure in the dilation of the aortic isthmus in late fetal life, (c) closure of ductus arteriosus after birth, (d) formation of the juxtaductal coarctation due to failure in the involution of the posterior shelf [135]

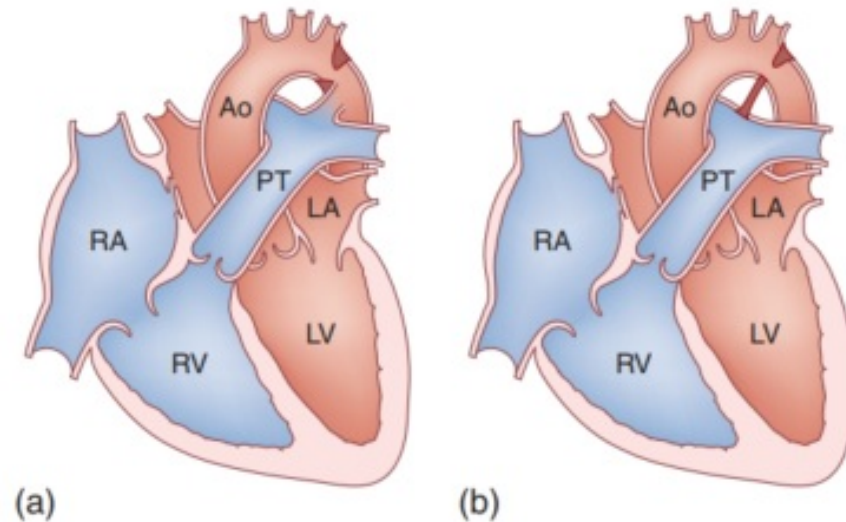


Figure 3.7: CoA with (a) and without (b) PDA [135]

3.3.4 Clinical Features

In coarctation of the aorta, the higher workload is imposed on the left ventricle to push the blood across the coarctation site, resulting in the need for higher pressure in the case of CoA. The pressure gradient along the coarctation site results in hypertension proximal to the obstruction site as well as hypotension below the coarctation site. This pressure discrepancy between the upper and the lower parts of the body leads to bounding pulses in the arms and neck as well as weak pulses in the lower extremities. High blood pressure in upper extremities may cause dizziness, headache, nosebleed, and left ventricular hypertrophy. The latter is the situation in which the left ventricular walls become larger and thicker due to high blood pressure. Low blood pressure after the obstruction site causes weakness, pallor, and coldness in lower parts of the body. Enlargement of collateral vessels, as well as dilation of intercostal arteries, are responses of the body to this situation. The sequelae associated with untreated CoA include a higher risk of stroke and a ruptured aneurysm. [137]

3.3.5 Diagnostic Principles

Diagnosis of the coarctation of the aorta, as the first step towards treatment of this disease, is of paramount importance. The diagnostic methods for the CoA can be divided into two main categories: invasive and non-invasive techniques. The mentioned techniques can assess the severity of the coarctation in terms of the geometry, or the hemodynamics of the aorta. These methods are explained in the following.

Doppler echocardiography (DE) is the first choice of imaging modalities to diagnose the coarctation of the aorta. Through this cheap, non-invasive method, the visualization of the coarctation site is feasible. It can also provide more information on the other potential cardiac pathologies such as left ventricular hypertrophy or bicuspid aortic valve (BAV) [131], which their occurrence with the coexistent CoA is not unusual [130]. DE can also be used for the estimation of the instantaneous peak-to-peak pressure gradient via the simplified Bernoulli equation (equation 3.1). The assumptions of steady, continuous, non-viscous, irrotational flow are used in this equation:

$$\Delta P = 4 (V_2^2 - V_1^2) \quad (3.1)$$

where V_1 and V_2 are the peak flow velocities (with the unit of m/s) proximal and distal to the site of the coarctation, respectively [138, 139, 140]. The number 4 (with the unit of $mmHg \cdot s^2/m^2$) in this equation is used to convert the result of the right-hand side of the equation from Pa to mmHg. Although doppler gradients may be helpful in the diagnosis of CoA via the equation mentioned above, the results of this equation are not reliable due to the collateral blood supply before and after the intervention [136]. Errors associated with the inappropriate position of the image

plane and operator dependence are among the issues that can affect the accuracy of the obtained results through DE [132].

Sphygmomanometry is a non-invasive, cheap, and fast method of choice for the initial assessment of the severity of the CoA. Since the pressure gradient more than 20 mmHg is the hallmark of the presence of the coarctation, this device is being employed to measure the arm-to-leg pressure difference. In this way, the pressure difference of more than 20 mmHg between the maximum systolic blood pressures in arms and legs is considered as an indicator of the CoA. However, studies report the inaccuracy of this method of choice in the assessment of the severity of the CoA and restenosis due to issues like collateral circulation [141, 142].

The gold standard for assessing pressure gradient across the coarctation site is cardiac catheterization and angiography (CA). High-resolution images of the aorta can be provided through this invasive method. The indicator for the presence of coarctation is the peak systolic pressure gradient of more than 20 mmHg [131, 133, 143, 144]. Aortic angiography can be utilized to specify the coarctation site, severity, and other related vascular abnormalities [144]. Although a high prevalence of recurrent aortic coarctation (in up to 42% of patients [142]) underscores the importance of frequent follow-up examinations, the invasive nature of this procedure makes multiple uses of this method difficult or even impossible for follow-up tests.

Computed tomography (CT) is another technique in which the acquisition of high spatial resolution data allows for assessing the anatomic characteristics of the aorta such as site, severity, and extent of the coarctation. It also enables us to reconstruct the vascular anatomy. However, this is an invasive method of choice containing radiations that makes the multiple uses of this method for follow-up purposes problematic.

Besides, hemodynamic information of the blood flow can not be obtained by CT. [132]

Cardiac Magnetic resonance imaging (CMRI) is the preferred non-invasive technique for the diagnosis and follow-up of the coarctation of the aorta. Three-dimensional gadolinium-enhanced CMR angiography can provide accurate information on the morphology of the aorta as well as the site and severity of the obstruction. It can also determine the formation of the collateral blood vessel. Analysis of LV function and myocardial mass is feasible through cine MRI, while the estimation of trans-coarctation pressure gradient and collateral flow calculation can be obtained using phase-contrast magnetic resonance imaging (PC-MRI). Recently, flow and pressure fields can be obtained using four-dimensional flow cardiac magnetic resonance (4D flow CMR). However, the need for the breath-holds during long acquisition time in CMR hampers its utilization in small children and claustrophobic patients. Furthermore, artifacts produced by the implanted metal stent is another restriction of this imaging modality for follow-up examinations. [132]

3.3.6 Methods of Treatment: Surgical Treatments

Coarctation of the aorta is fatal if it remains untreated. It is reported that it leads to death in 75% of unoperated cases by the age of 46, with a mean survival of 35 years [133], underscoring the importance of therapy in CoA patients. One of the main methods of treatment for CoA is surgical repair. Surgical treatment of the CoA comprises three main methods: resection of the obstruction with end-to-end anastomosis, patch graft aortoplasty, and subclavian flap aortoplasty. The patient's age, the anatomy of the aorta and coarctation, and the surgeon's preference are parameters that determine the type of surgical treatment [145].



Figure 3.8: Schematic of classic end-to-end anastomosis for surgical repair of CoA [145]

The introduction of surgical repair of CoA was in 1944 through direct end-to-end anastomosis [146]. During classical resection of the obstruction with end-to-end anastomosis, the distal and proximal parts of the blockage are excised and then connected together, as shown in Figure 3.8. In this method, the subclavian artery remains unchanged; thus, it can function normally. For many young infants and neonates, severe aortic arch hypoplasia coexists with CoA. For them, the extended end-to-end anastomosis is employed in which two longitudinal cuts are made on the undersurface of the aortic arch and lateral aspect of the lower aorta. Then, two ends of the aorta are connected together. This method of treatment is illustrated in Figure 3.9. Using this method, obstruction and hypoplasia can be treated without the need for the prosthetic material that cannot grow. [145]

Patch graft aortoplasty was first introduced in 1957 [147]. This procedure is useful in cases with long-segment stenosis. During this procedure, the aorta is incised from the ostium of the left subclavian artery and through the obstruction site to the proximal descending aorta. Then, a prosthetic graft is placed in the region of

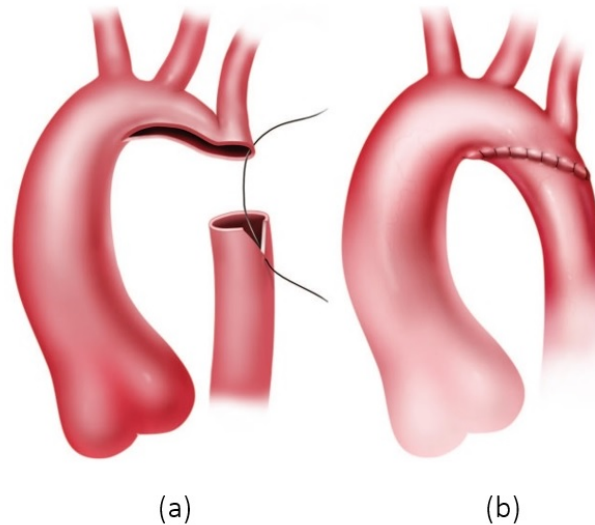


Figure 3.9: Schematic of extended end-to-end anastomosis for surgical repair of CoA: (a) incision for surgical repair, (b) repaired coarctation [145]

the removed segment (Figure 3.10). However, this method of treatment is associated with a rise in the risk of post-operation aneurysm formation. [145]

Subclavian flap aortoplasty is another surgical treatment for CoA (Figure 3.11) proposed in 1966 [148]. In this procedure, the left subclavian artery is ligated before the ostium of the vertebral artery. Next, the left subclavian artery is incised through the coarctation to the lower aorta. Then, the incised flap of the left subclavian artery is utilized to augment the incised segment of the aorta. This method of treatment has the ability to repair the long-segment stenosis without using a prosthetic graft. However, this procedure is associated with the decreased flow to the left upper organs due to ligating the left subclavian artery [145].

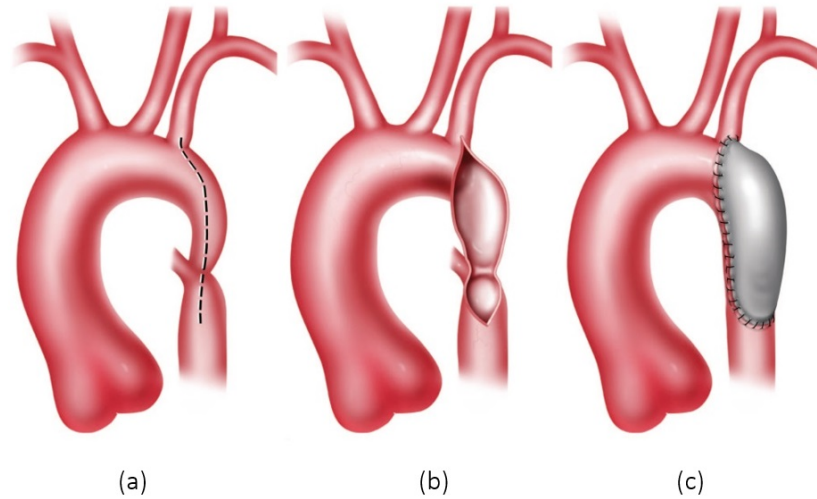


Figure 3.10: Schematic of patch graft aortoplasty repair for CoA: (a) site of the incision for patch graft aortoplasty shown by a dashed line, (b) incising the site of stenosis, (c) suturing prosthetic graft for patch aortoplasty [145]

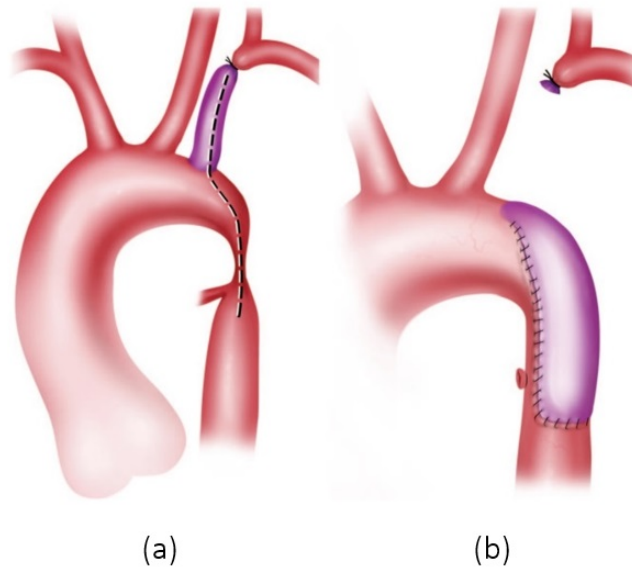


Figure 3.11: Schematic of the subclavian flap aortoplasty for the treatment of CoA: (a) site of incision shown by a dashed line, (b) repaired coarctation by flap aortoplasty treatment [145]

3.3.7 Methods of Treatment: Interventional Treatments

Interventional treatments for repairing CoA include balloon angioplasty and stent deployment. Balloon angioplasty is a common method of choice in the treatment of recoarctation that has shown promising results. It was first proposed to treat the native coarctation in 1982 [149]. Although this method of treatment is considered safer in repairing the recoarctation than in the native coarctation, some studies indicate similar results in both categories [150]. Balloon angioplasty is a minimally invasive procedure in which a long thin hollow tube called catheter is inserted into the artery and guided to the coarctation site. The catheter is accompanied by a balloon that is inflated to widen the coarctation. Then the balloon is deflated, and the catheter is removed from the artery. The complications associated with balloon angioplasty are similar for both native and recurrent coarctation. These complications include early complications like site injury and aneurysm formation, and late complications such as aneurysm formation and development of hypertension [145].

Stent deployment is the newest treatment of choice in patients with recurrent coarctation after surgical treatment or balloon angioplasty, long-segment obstruction, or patients with a high risk of surgery. It was first introduced in 1991 to repair the CoA [151]. Figure 3.12 illustrates the procedure of stent placement. During this procedure, a stent, which is a small wire-mesh tube, is inserted into the artery using a catheter. This stent is expanded by the expansion of the balloon and left inside the vessel wall to help keep the wall open. Stent deployment causes less damage to the vessel wall in comparison with balloon angioplasty. That is because the stent does not need to overdilate the vessel to eliminate the obstruction, and also it supports the vessel wall structure [152]. However, this method of treatment is not recommended

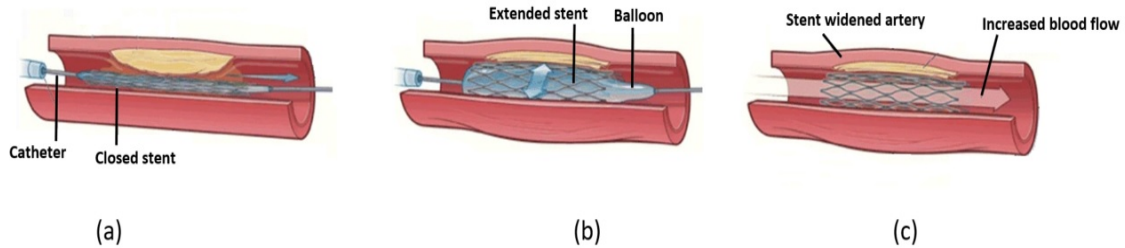


Figure 3.12: A schematic of stent deployment for the treatment of the CoA: (a) insertion of a balloon catheter with a stent in the coarctation site, (b) balloon expansion for widening the obstruction, (c) balloon deflation and retrieving the catheter, picture adapted from [153]

for children due to growth issues. Aortic rupture or dissection, stent fracture, incomplete stent expansion, stent migration, and aneurysm formation are among the complications associated with stent placement, necessitating long-term follow-up to assess the treatment outcome [145].

3.4 Summary

In this chapter, the blood circulatory system and anatomy of the aorta were described to provide readers with some background knowledge on the clinical aspects of this thesis. Next, the coarctation of the aorta and available treatment of choices for this disease were discussed. Also, the advantages and risks associated with these treatments were explained. The limitations of each imaging modality of choice were discussed to underscore the importance of CFD study in assessing the severity of CoA, evaluating treatments, and deciding about the timing of intervention. The next chapters are allocated to show the ability of a CFD model in this regard.

Chapter 4

Modeling and Methodology

This chapter is allocated to present the geometries, initial conditions, and boundary conditions utilized in this study. Next, the meshing method is illustrated, and the numerical errors are investigated for the pre- and post-intervention cases. ANSYS Workbench 2020 R was used to generate the mesh, and all the simulations were run on a Compute Canada's national cluster called Graham using OpenFoam and swak4Foam library. OpenFoam is an open-source CFD tool in which the cell-centered finite volume method is used to formulate the governing equations. swak4Foam is a library used for importing the patient-specific transient pulsatile boundary condition. The name of this library stands for SWiss Army Knife for Foam. Large Eddy Simulation (LES) – one equation model is utilized in this study to solve the governing equations. This model can simulate flows with large recirculation zones. As the blood flow in the aorta is dominated by the separation and recirculation regions, this model is an appropriate one to simulate the transient blood hemodynamics in the aorta. In this method, filtered conservation equations are used to resolve eddies larger than the grid scale. On the other hand, the motions below the size of the mesh are modeled

using a sub-grid scale model called one equation model. In this model, viscosity in the Navier-Stokes equations consists of molecular viscosity (ν) and sub-grid scale viscosity (ν_{sgs}). Molecular viscosity is a property of the fluid material, while the sub-grid scale viscosity is a property of the turbulent flow. Sub-grid scale turbulent kinetic energy (k_{sgs}), which is a function of velocity oscillations below the grid size, is utilized in the calculation of sub-grid scale viscosity. k_{sgs} is defined by sub-grid scale model. In one equation model, a transport equation for (k_{sgs}) is used by the solver to find the Sub-grid scale turbulent kinetic energy. The backward time scheme, which is a second-order implicit scheme, was applied for the temporal discretization. Also, discretization in space was performed using the second-order scheme. Segregated PISO algorithm was used to solve the mass-momentum equations in this study.

4.1 Patient-Specific Pre- and Post-intervention Geometries

Obtaining the computational domain is the first stage in the CFD study of hemodynamics in the human aorta. There are some studies on the hemodynamics in the aorta using the idealized geometries. In some of them, the blood flow is simulated in the pipe [154, 155, 156]. However, in most of the computational works with idealized geometries, patient-specific geometries obtained from the medical imaging data with some assumptions were employed to model the blood flow in the aorta. These assumptions consist of disregarding the aortic arch branches, considering the constant diameter throughout the trunk and circular cross-section area [2]. However, most recent computational studies utilized patient-specific geometries of the aorta obtained

Table 4.1: Typical dimensions of the aorta in adults [3]

| | <i>Diameter (mm)</i> | <i>Length (cm)</i> |
|----------------------------|----------------------|--------------------|
| Ascending aorta | 25 in the inlet | 5 |
| Aortic Arch | - | 4-5 |
| Brachiocephalic Artery | 12 in the ostium | - |
| Left Common Carotid Artery | 7 in the ostium | - |
| Left Subclavian Artery | 9 in the ostium | - |
| Thoracic Aorta | 15 in the outlet | 20 |

from medical imaging data. In this work, the aorta’s patient-specific geometries before and after the intervention are employed without any simplification using the CT images.

Dimensions of the aorta are in strong correlation with parameters like age, body surface area (BSA), height, and weight [157, 158]. However, the approximate dimensions related to this study for various parts of the aorta in adults (obtained from [4]) are listed in Table 4.1 for the sake of comparison with the patient-specific dimensions in the present study. The areas related to the inlet (Ascending aorta) and outlet boundaries (Outlet 1: Brachiocephalic Artery(BCA), Outlet 2: Left Common Carotid Artery (LC), Outlet 3: Left Subclavian Artery (LS), and Outlet 4: Descending Aorta (DAo)) for the patient’s aorta before and after the intervention and their corresponding diameters are summarized in Table 4.2. Figure 4.1 shows front and back views of the patient’s aorta in pre- and post-intervention states using the ANSYS Workbench 2020 R.

The coarctation index, defined as the ratio of aortic diameter at the coarctation site to that of at the normal site, is utilized to assess the severity of the obstruction. The coarctation severity can be considered as mild, moderate, or severe for

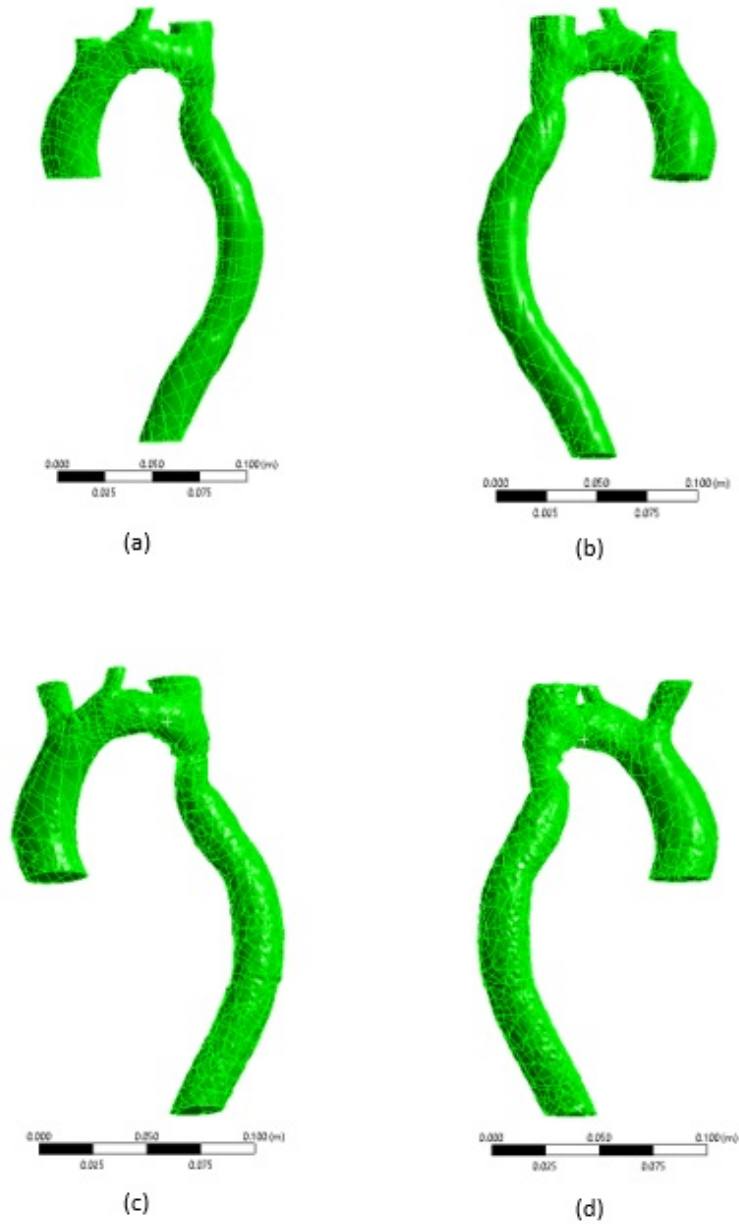


Figure 4.1: Front view (a) and back view (b) of the patient's aortic geometries before the intervention - front view (c) and back view (d) of the patient's aortic geometries after the intervention using ANSYS Workbench 2020 R

Table 4.2: Surface areas and their corresponding diameter for boundaries in pre- and post-intervention

| | <i>Pre-intervention</i> | | <i>Post-intervention</i> | |
|-----------------|-----------------------------|------------------------------------|-----------------------------|------------------------------------|
| | <i>Area (m²)</i> | <i>Corresponding Diameter (mm)</i> | <i>Area (m²)</i> | <i>Corresponding Diameter (mm)</i> |
| <i>Inlet</i> | 6.4222 E-4 | 28.59 | 6.2559 E-4 | 28.22 |
| <i>Outlet 1</i> | 1.5861 E-4 | 14.21 | 2.0295 E-4 | 16.07 |
| <i>Outlet 2</i> | 5.8432 E-5 | 8.62 | 5.0643 E-5 | 8.03 |
| <i>Outlet 3</i> | 3.2333 E-4 | 20.29 | 3.2315 E-4 | 20.28 |
| <i>Outlet 4</i> | 3.6557 E-4 | 21.57 | 4.0579 E-4 | 22.73 |

the coarctation index of more than 0.65, between 0.5 and 0.65, or less than 0.5, respectively [136]. Based on this definition, the coarctation indexes for the pre- and post-intervention cases are roughly 0.86 and 0.85, respectively. So, the coarctations in both pre- and post-intervention cases studied here are categorized as mild coarctation, and that the post-intervention state is accompanied by the residual stenosis.

4.2 Initial and Boundary Conditions

In the present study, aortic inlet flow enters the ascending aorta, and the outlet flow leaves the aorta via four outlets: the brachiocephalic artery, left common carotid artery, left subclavian artery, and descending aorta. The aortic input volumetric flow rates over one cardiac cycle for the pre-intervention and post-intervention cases obtained from our in house LPM algorithm [60, 41, 59, 63] are presented in Figures 4.2 and 4.3, respectively. As shown in these graphs, the aortic input flow in pre- and post-intervention cases are different in several terms: start of the ejection time in which

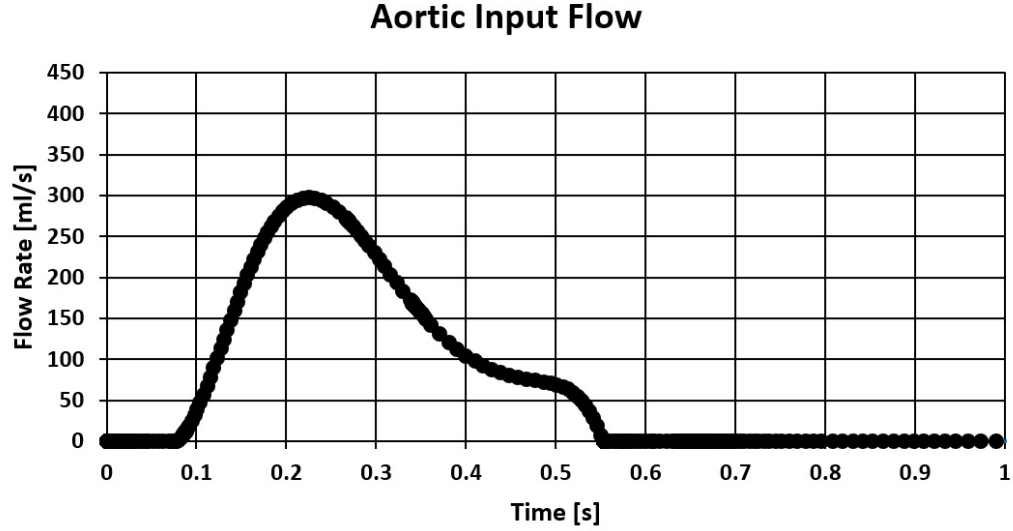


Figure 4.2: Input flow boundary condition in pre-intervention case obtained from our in house LPM algorithm [60, 41, 59, 63]

the blood is ejected to the aorta, maximum flow rate, the total ejection time, overall shape of the diagrams, and the time duration for one cardiac cycle. Presented initial boundary conditions result in the maximum Reynolds numbers of 4412 and 6199 for pre- and post-intervention states, respectively. The flat spatial velocity profile is applied to the boundaries in this study.

Our in house LPM algorithm [60, 41, 59, 63] provides the percentage of the flow exiting from three aortic arch branches, so the rest of the blood flow rate leaves the trunk of the descending aorta, as shown in equation 4.1.

$$Q_{total} = Q_1 + Q_2 + Q_3 \quad (4.1)$$

where Q_{total} is the volumetric flow rate leaving the three aortic arch branches provided by our in house LPM algorithm [60, 41, 59, 63]. In the above equation, Q_1 , Q_2 , Q_3 represents the flow rates exiting the brachiocephalic artery, left common carotid

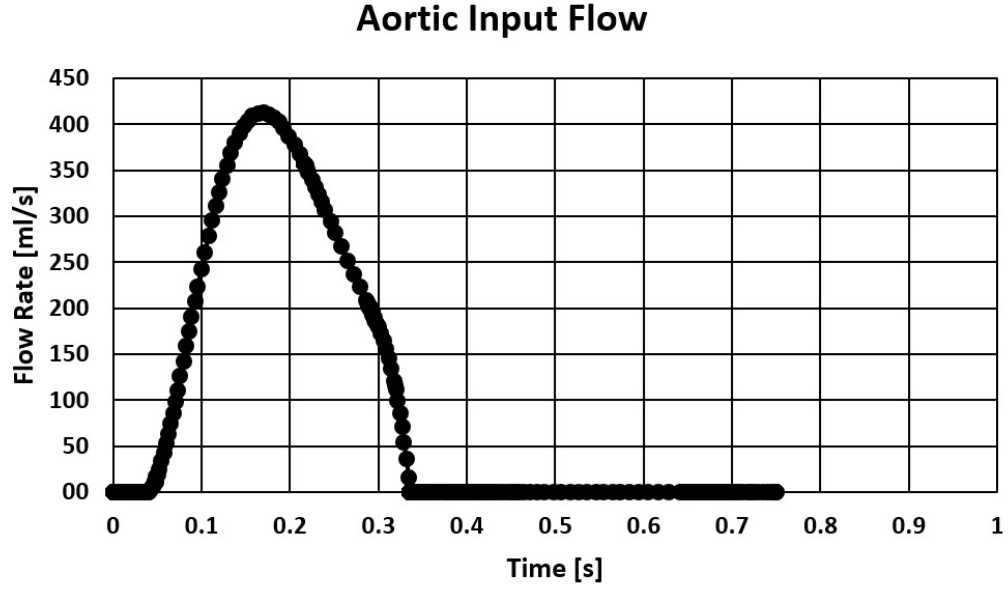


Figure 4.3: Input flow boundary condition in post-intervention case obtained from our in house LPM algorithm [60, 41, 59, 63]

artery, and left subclavian artery, respectively. As our in house LPM algorithm [60, 41, 59, 63] does not show the amount of blood flow rate exiting from each of the three branches in the aortic arch separately, the output flow rate of each of these branches is calculated using the assumption of equal uniform flow velocity in the mentioned branches. So, the following equation can be used to measure flow rate in each of the branches (Q_i):

$$Q_i = \frac{Q_{total}}{A_1 + A_2 + A_3} A_i \quad (4.2)$$

where A_i is the cross-section surface area of the desired branch. Figure 4.4 shows a schematic of dividing the aortic input flow between aortic arch branches and the descending aorta for both pre- and post-intervention cases. As this figure shows, the output aortic flow differs between pre- and post-intervention cases.

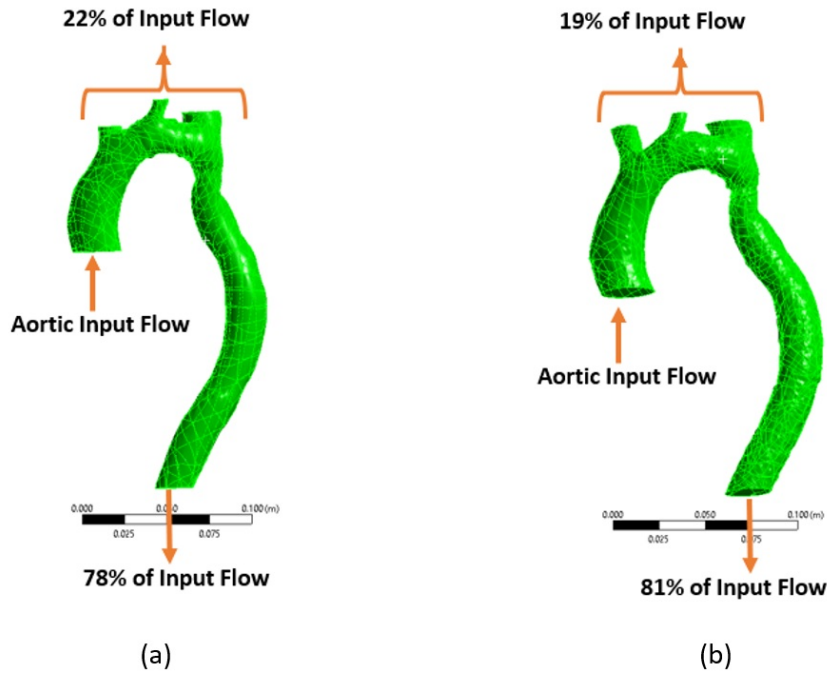


Figure 4.4: Schematic of input and output flow boundary conditions for pre-intervention (a) and post-intervention (b) cases

The results of the output flow rate for each of the aortic arch branches using equation 4.2, as well as the output flow rate of the descending aorta are presented in Table 4.3.

The assumption of equal velocity value between three aortic arch branches agrees with the literature in which the aortic arch branches have different outflow rates; however, equal flow rate assumption in three aortic arch branches have also been used in some studies [6, 28]. Table 4.4 summarizes the outflow rates in the outputs in some of the CFD works on the aorta.

Blood is assumed as a Newtonian fluid with a density of 1050 kg/m^3 and dynamic viscosity of 3.15 E-3 Pa.s in the simulation. Initial pressure and velocity over the computational domain for both pre- and post-intervention cases are set to zero. Wall is assumed to be non-permeable and rigid. The no-slip boundary condition is applied

Table 4.3: Percentage of the input volume flow rate exiting through outlets in pre- and post-intervention cases

| | <i>BCA</i> | <i>LC</i> | <i>LS</i> | <i>DAo</i> |
|--------------------------------|------------|-----------|-----------|------------|
| <i>Pre-intervention State</i> | 6.46% | 2.38% | 13.16% | 78% |
| <i>Post-intervention State</i> | 6.68% | 1.67% | 10.65% | 81% |

Table 4.4: Percentage of the input volume flow rate exiting through outlets in CFD studies

| <i>Author(s)</i> | <i>Reference Number</i> | <i>Date of Publication</i> | <i>BCA</i> | <i>LC</i> | <i>LS</i> | <i>DAo</i> |
|------------------|-------------------------|----------------------------|------------|-----------|-----------|------------|
| Svensson et al. | [159] | 2006 | 15% | 5% | 10% | 70% |
| Wen et al. | [21] | 2010 | 11.3% | 6.8% | 4.5% | 77.4% |
| Brown, A. et al. | [25] | 2011 | 27% | 6% | 12% | 55% |
| Brown, S. et al. | [119] | 2012 | 13% | 4% | 5% | 78% |
| Sadeghi et al. | [41] | 2020 | - | - | - | - |

on the rigid wall for the velocity field. Zero gradient pressure is utilized in the inlet and wall, and output pressure in aortic arch branches and descending aorta are set to zero.

4.3 Meshing

To solve the governing equations over the computational domain, the domain should first be discretized into the limited number of subdomains called elements or cells.

The style and the number of these elements over which the equations are being solved greatly influence the accuracy, efficiency (i.e., how fast is the simulation), robustness (i.e., how reliably the solver converges) of the simulation results. More elements are required in the case of complex computational domains, like patient-specific aortic geometry; however, the number of elements used in the simulation directly correlates with the computational costs. In other words, smaller cells or larger mesh size will require more memory and CPU time to run. So, a balance between the accuracy and the resources should be considered.

Choosing a proper meshing style or meshing topology is crucial while doing spatial discretization of the computational domain. In idealized geometries, structured hexahedral elements are the first preference [2]. This type of mesh requires very low memory and CPU time per node. However, in the complex patient-specific geometries, discretizing the domain via unstructured meshes is inevitable. In the present work, an unstructured hybrid mesh was generated for both pre- and post-intervention cases. This hybrid mesh consists of prism elements that start from the rigid wall with the first layer height of $15\text{E-}6$ m and growth rate of 1.2, tetrahedral (tet.) elements that fill the rest of the geometry in post-intervention case, and a small number of pyramids elements in pre-intervention geometry. This mesh topology utilized in one of the cases in this study is shown in Figure 4.5. The first layer thickness and the total number of prism layers are chosen so that near-wall resolution is fine enough for accurately resolving the shear layer. In each of the pre- and post-intervention cases, the above-mentioned prism mesh characteristics were kept unchanged, and the difference between different mesh sizes is mainly due to the different number of tetrahedral cells. More details on the two mesh sizes employed in this study for each pre- and

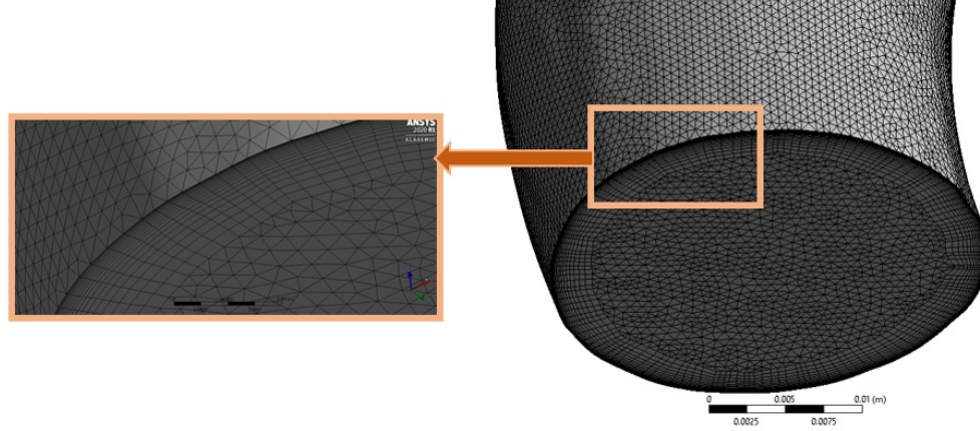


Figure 4.5: Meshing style used in pre- and post intervention geometries

post-intervention cases are summarized in Table 4.5. Growth factor of prism cells for all the meshes is set to 1.2.

All the meshes summarized in Table 4.5 were checked for mesh quality in terms of their mesh skewness and orthogonality. In ANSYS, skewness is defined as follows:

$$Skewness = \max \left[\frac{\theta_{max} - \theta_e}{180 - \theta_e}, \frac{\theta_e - \theta_{min}}{\theta} \right] \quad (4.3)$$

where θ_e is the equiangular face/cell, and is 60° for tetrahedral and triangular meshes and 90° for quadrilateral and hexahedral meshes. θ_{max} and θ_{min} are maximum and minimum angles in each cell, respectively. Based on this definition, cells with the skewness of 0 has the best mesh quality and those with the skewness of 1 has the worst mesh quality.

Mesh orthogonal quality in ANSYS is defined as follows:

$$Orthogonal\ quality = \min \left[\frac{\vec{A}_i \cdot \vec{f}_i}{|\vec{A}_i| \cdot |\vec{f}_i|}, \frac{\vec{A}_i \cdot \vec{c}_i}{|\vec{A}_i| \cdot |\vec{c}_i|} \right] \quad (4.4)$$

Table 4.5: Characteristics of meshes resulted from discretizing the pre- and post-intervention geometries

| | <i>Mesh No.</i> | <i>First Layer Height (E-6m)</i> | <i>No. of Prism Layers</i> | <i>Total No. of Cells</i> | <i>No. of prism Cells</i> | <i>No. of Pyramid Cells</i> | <i>No. of Tet. Cells</i> |
|--|---------------------|--|--|-----------------------------------|---------------------------------------|---|--------------------------------------|
| <i>pre- interven- tion Geometry</i> | 1 | 15 | 20 | 6,959,518 | 3,087,860 | 26,289 | 3,845,369 |
| | 2 | 15 | 20 | 23,377,281 | 6,673,043 | 56,603 | 16,647,635 |
| <i>post- interven- tion Geometry</i> | 1 | 15 | 10 | 10,743,464 | 2,195,040 | - | 8,548,424 |
| | 2 | 15 | 10 | 17,803,815 | 3,165,460 | - | 14,638,355 |

where \vec{A}_i is the face normal vector, \vec{f}_i is the vector from the centroid of the cell to the centroid of the face, and \vec{c}_i is the vector from the centroid of the cell to the centroid of the adjacent cell. Based on this definition, cells with the orthogonal quality of the 0 have the worst orthogonal quality and cells with the orthogonal quality of 1 have the best orthogonal quality. The results of mesh skewness and orthogonal quality for mesh No.1 pre-intervention case are presented in Figures 4.6 and 4.7, respectively. It is worth mentioning that the Tet4, Wed6, and Pyr5 elements in figures showing the mesh skewness and orthogonal quality are representatives of tetrahedral, prism, and pyramid elements, respectively. The results of mesh skewness and orthogonal quality for other meshes are presented in Appendix A.

Each of the generated meshes is divided between 64 processors to be run by the Graham cluster. To split the computational domain, the “scotch” algorithm was employed in this study through which the mesh cells are divided almost equally

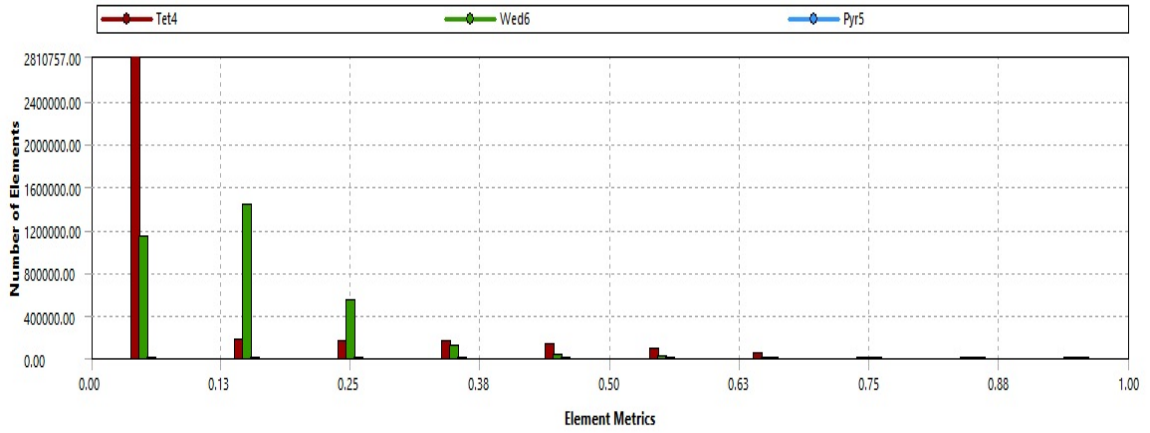


Figure 4.6: Mesh skewness for mesh No.1 pre-intervention case

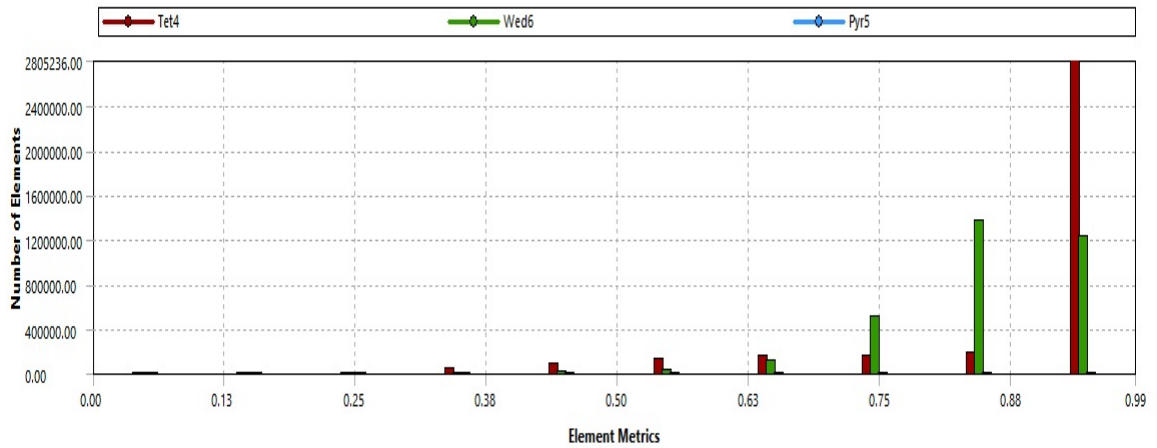


Figure 4.7: Mesh orthogonal quality for mesh No.1 pre-intervention case

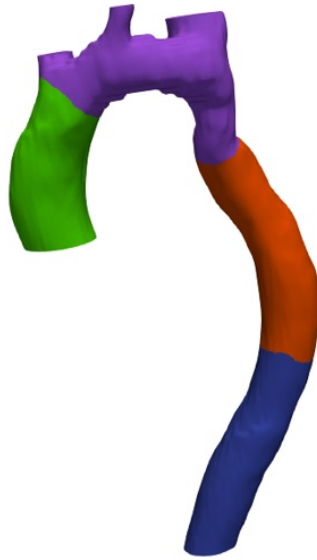


Figure 4.8: Meshing style used in pre- and post-intervention geometries

between different processors. Figure 4.8 shows different regions of the computational domain distinguished by different colors that are allocated to 4 processors via this method.

4.4 Grid and Timestep Independence

Spatial discretization of the computational domain through meshing and then solving the governing equations on that mesh using the proper timestep are inevitable parts of the CFD simulations. Since spatial and temporal discretization schemes can remarkably influence the simulation results, Grid and timestep dependence studies are of paramount importance to assess the effects of these schemes and quantify the numerical errors associated with them. In the present work, the timestep and grid independence were studied to assure that the simulation results are independent of the mesh size and timestep. The following sections are allocated to quantifying the

errors associated with timestep and grid size. However, detailed information on the definition of the parameters and the explanation of the simulation results will be discussed in the next chapter.

4.4.1 Timestep Independence: Pre-intervention Case

Timestep independence study guarantees that the simulation results are independent of the selected timestep for that simulation. This study was performed for mesh No. 1 pre-intervention case. For this mesh, simulations were done for two timesteps of $8\text{E-}6$ s (coarse timestep) and $4\text{E-}6$ s (fine timestep). Then, the results of these simulations were compared in terms of time-averaged wall shear stress (TAWSS), as well as the velocity profile in different planes. Figure 4.9 shows the results of TAWSS for the two mentioned simulations. The front and back view of the aorta are shown in this figure. As shown in Figure 4.9, the results of TAWSS for the coarse and fine timesteps are in good qualitative agreements. The most difference between the results of TAWSS for the coarse and fine timesteps can be observed on the back view of the aorta near the outlet of the aortic arch branches. This difference may be due to the high roughness of the aortic wall in these regions. This roughness resulting from cutting the geometry in these regions can lead to generating the mesh with less desirable quality. The inlet boundary of the ascending aorta, as well as outlet boundary in the descending aorta region, also have this roughness; however, the TAWSS in these regions is not high enough to make the difference between TAWSS for the coarse and fine timesteps visible. Since the aortic arch branches are not the regions of interest in this study, the difference mentioned above in these regions was neglected, and the results of the two timesteps were accepted to be in good agreement overall.

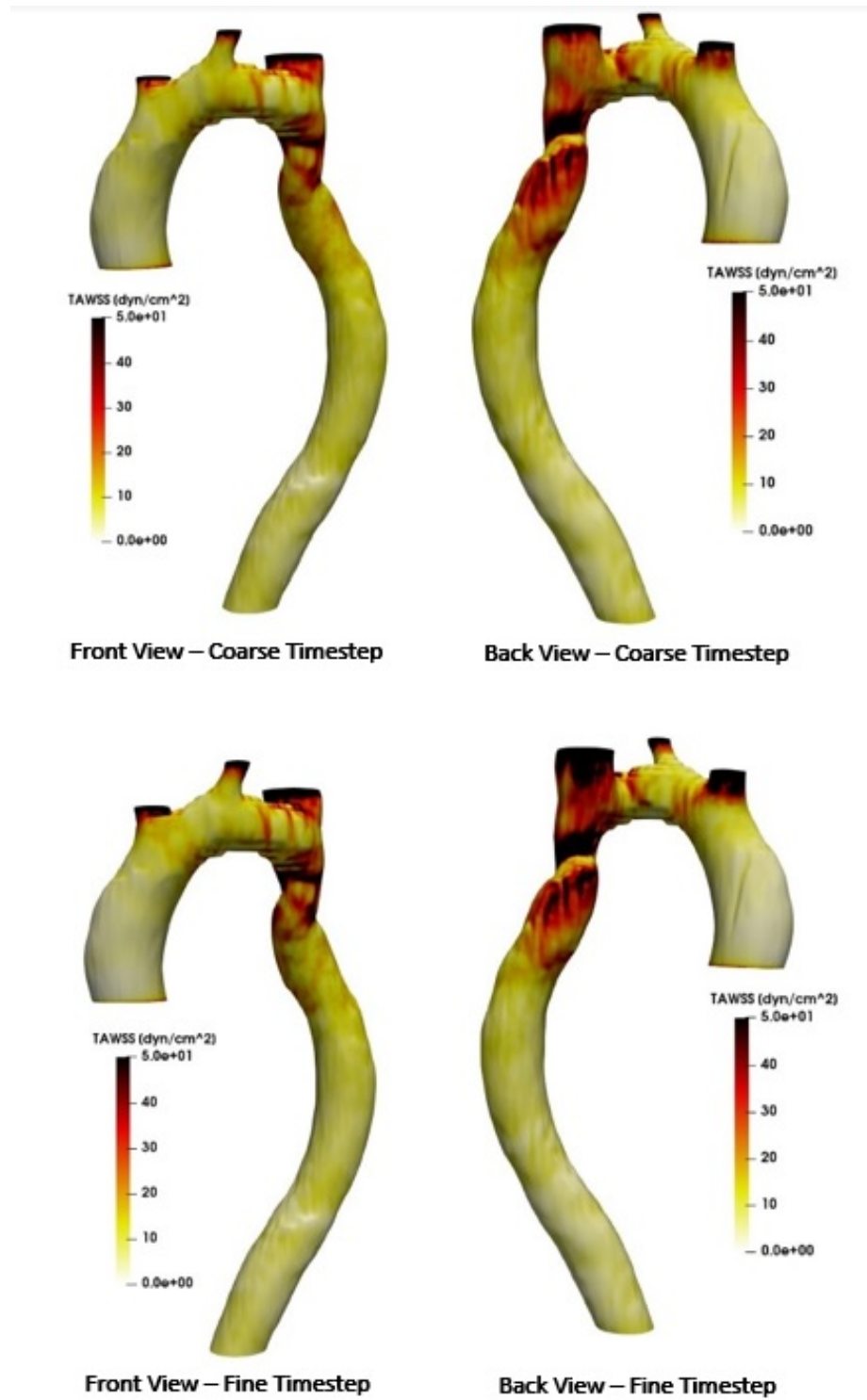


Figure 4.9: Simulation results of the TAWSS for the pre-intervention case using the coarse and fine timesteps

Figure 4.10 shows the velocity profile in various slices for two mentioned timesteps using the coarse grid of the pre-intervention case. The results are presented at 0.22s of the cardiac cycle. This time interval is in the peak systole. Two different slices are selected in a way that they include ascending aorta, aortic arch, descending aorta, and the site of the coarctation. The velocity magnitude over a line was plotted for two slices, comparing the simulation results using the coarse and fine time steps. The results are shown in this figure for the time instant of 0.2s, which is near peak systole. Comparing the simulation results for other time intervals also showed a similar agreement. The root mean square errors for the simulation results are shown in this figure. As shown in these pictures, the results of the coarse and fine timestep are in good agreement. More agreement between the coarse and fine timesteps required applying finer timesteps, which increases the computational costs.

4.4.2 Timestep Independence: Post-intervention Case

Timestep independence study was also performed for the post-intervention case, mesh No.1. Two timesteps of $4\text{E-}6$ s (fine timestep) and $8\text{E-}6$ s (coarse timestep) were applied to run the simulations. Then, the simulations' results were compared in terms of the TAWSS and velocity profile in various planes. Figure 4.11 shows the results of TAWSS for two simulations. Comparing the results of the TAWSS for the mentioned timesteps for the front and back view of the geometry shows that the coarctation site and the necking area were subjected to high TAWSS in both simulation results. The results of the finer timestep show a bit higher TAWSS in some areas; however, comparing the results of simulations for the two timesteps shows good agreement, overall. Figure 4.12 compares the results of the velocity magnitude

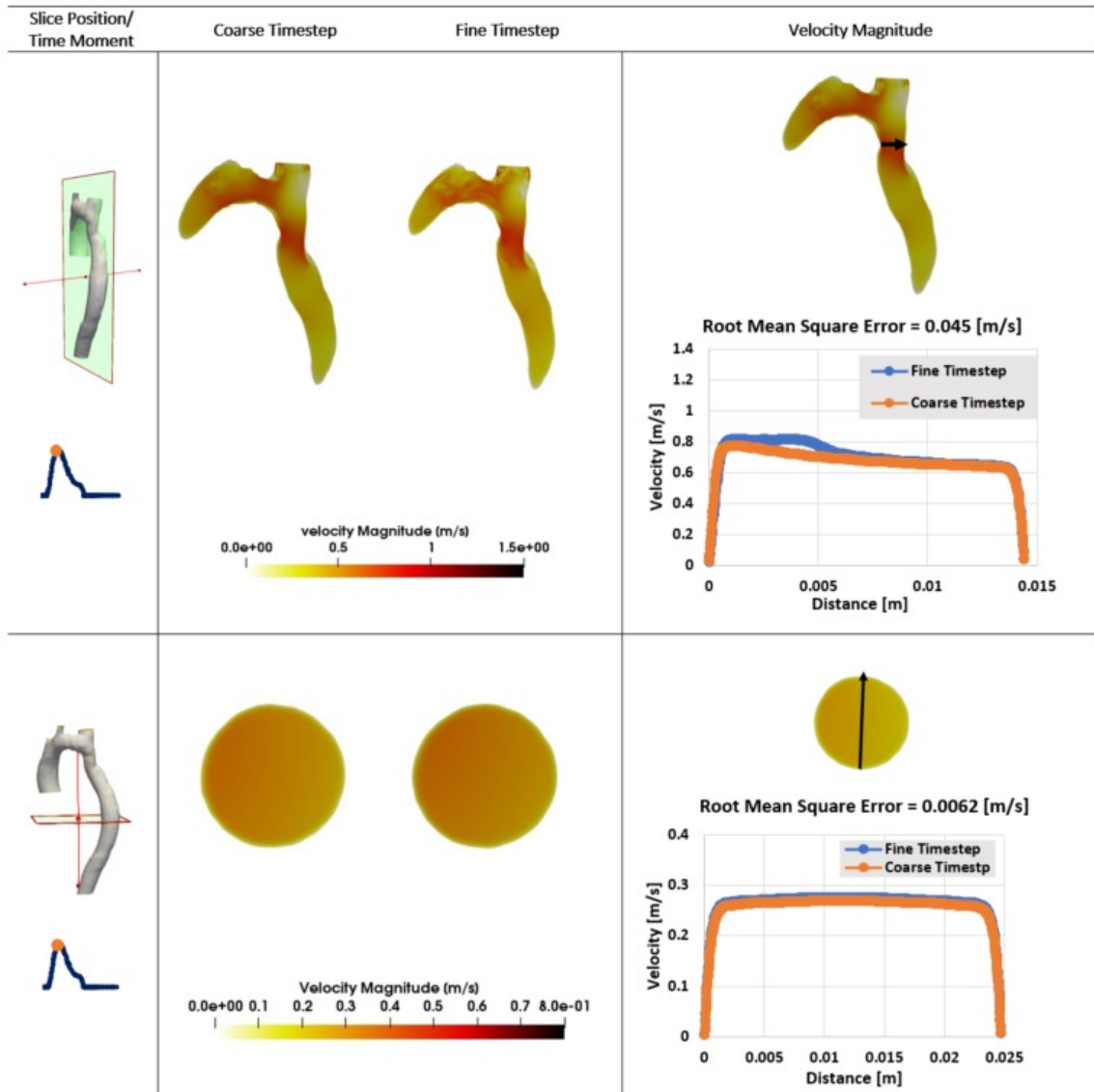


Figure 4.10: Simulation results of the velocity profile in two planes for the pre-intervention case using the coarse and fine timesteps

over the two planes for the coarse and fine timesteps. The results for two planes and the diagrams of the velocity magnitude are shown in this figure. The results show good agreement; however, a slight time lag of 0.02 s was observed in the results of the velocity magnitude.

4.4.3 Grid Independence: Pre-intervention Case

To assess the grid dependence, simulations were run for two mesh sizes, as described in Table 4.5. For the pre-intervention case, two mesh sizes of 6,959,518 cells and 23,377,281 cells were applied using the timestep of 8E-6 s. The results of the simulations were compared in terms of the TAWSS and velocity profile. Figure 4.13 shows the results of TAWSS for these two simulations for the pre-intervention case. Good qualitative agreement between the results of these grids shows the grid independence for the TAWSS assessment. Figure 4.14 shows the quantitative grid independence study in terms of the velocity magnitude in the same slices used in the time dependence study for the pre-intervention case. Although the same time lag exists between the results of the coarse and fine grids, the results are in good quantitative agreement, proving that the coarse grid is fine enough to show the aortic hemodynamics in the pre-intervention case.

4.4.4 Grid Independence: Post-intervention Case

Like for the pre-intervention case, the grid independence study was performed for the post-intervention case. Two mesh sizes of the 10,743,464 cells and 17,803,815 cells were applied as the coarse and fine grids, respectively. The timestep using to run these simulations is 8E-6 s. Figure 4.15 shows the front view and back view of

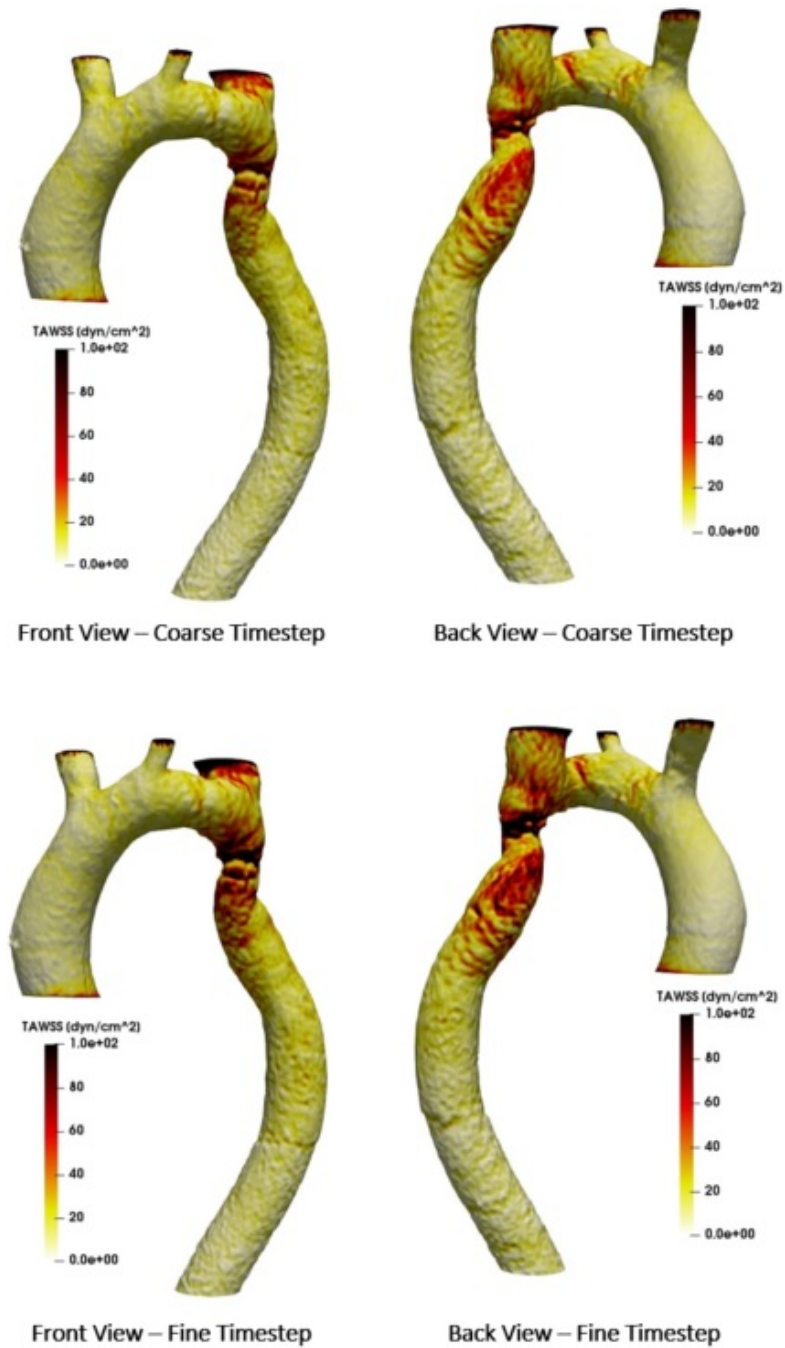


Figure 4.11: Simulation results of the TAWSS for the post-intervention case using the coarse and fine timesteps

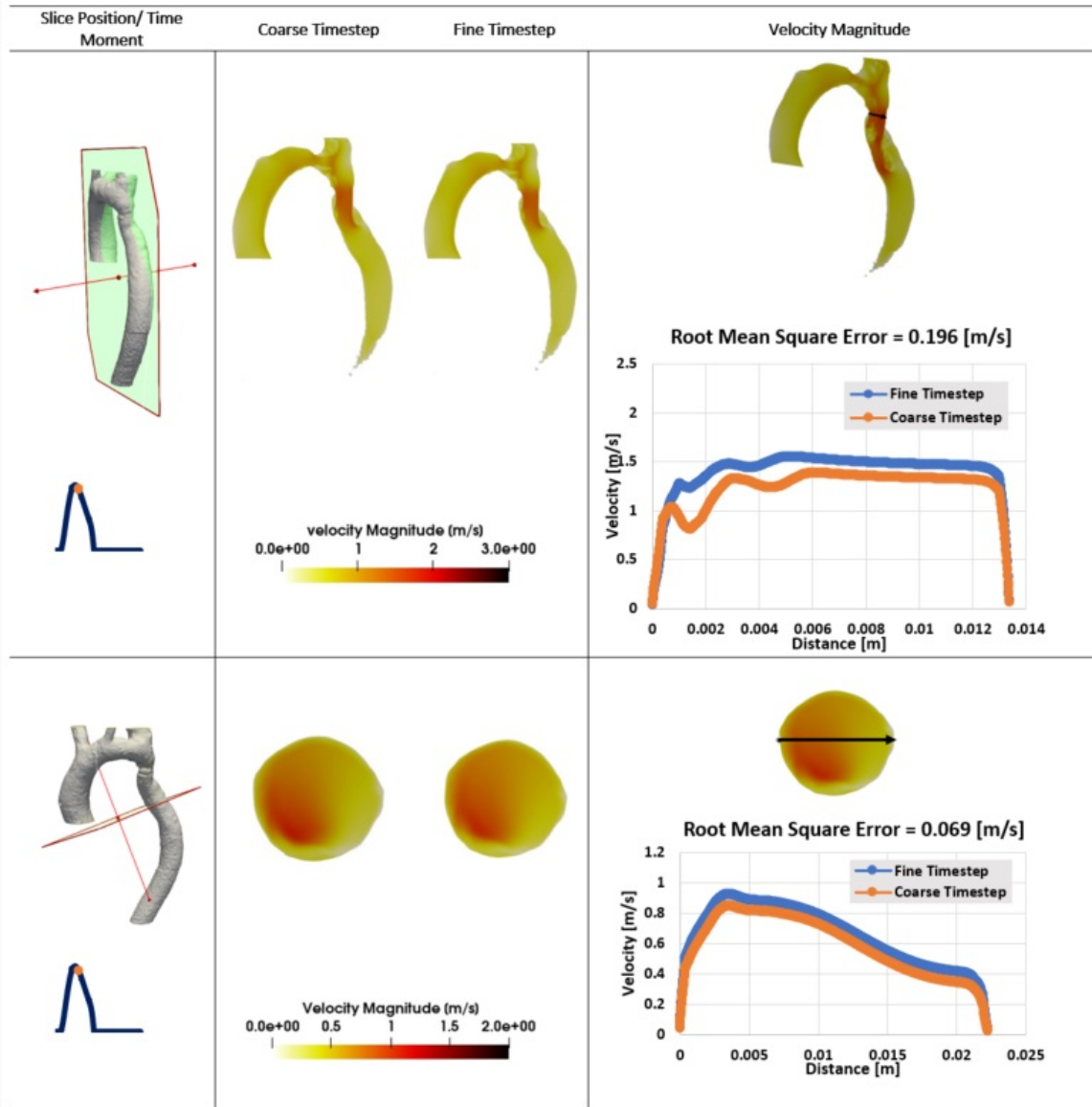


Figure 4.12: Simulation results of the velocity profile in two planes for the post-intervention case using the coarse and fine timesteps

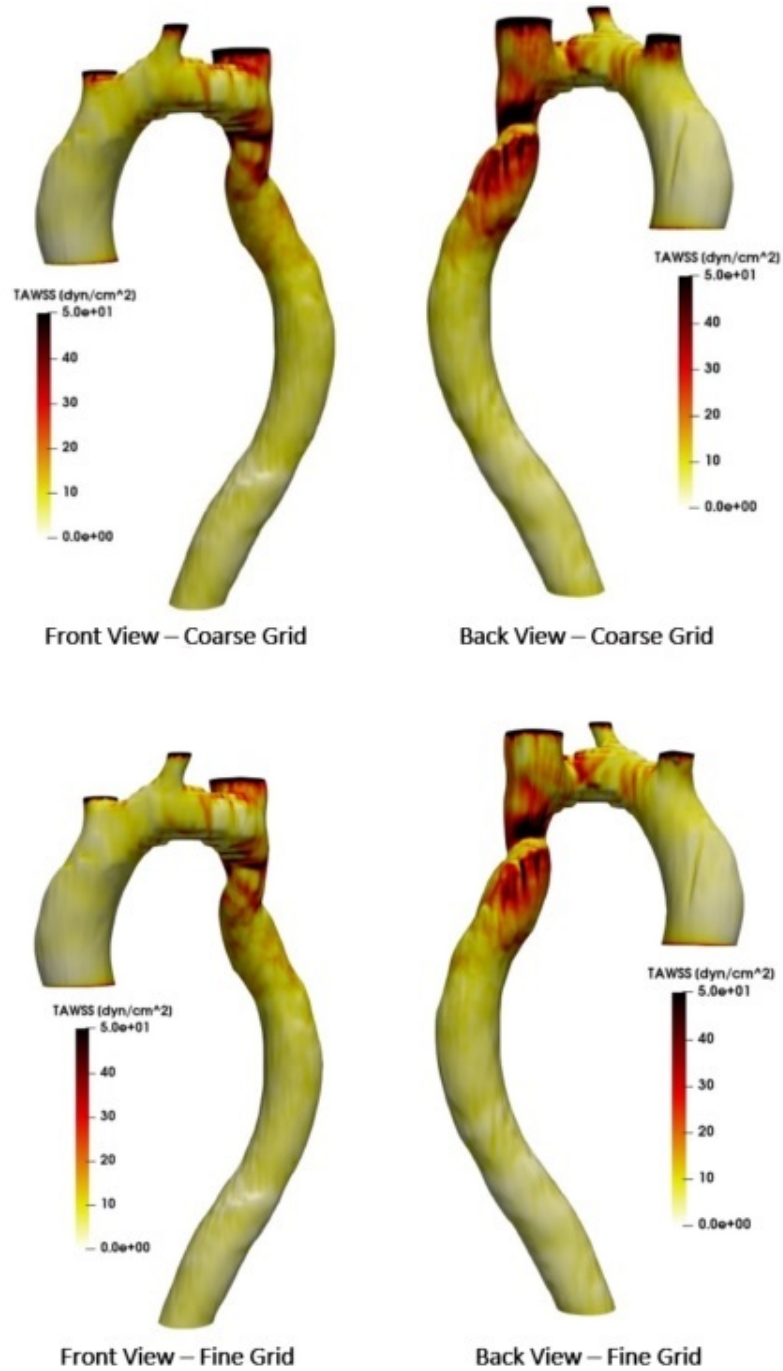


Figure 4.13: Simulation results of the TAWSS for the pre-intervention case using the coarse and fine grids

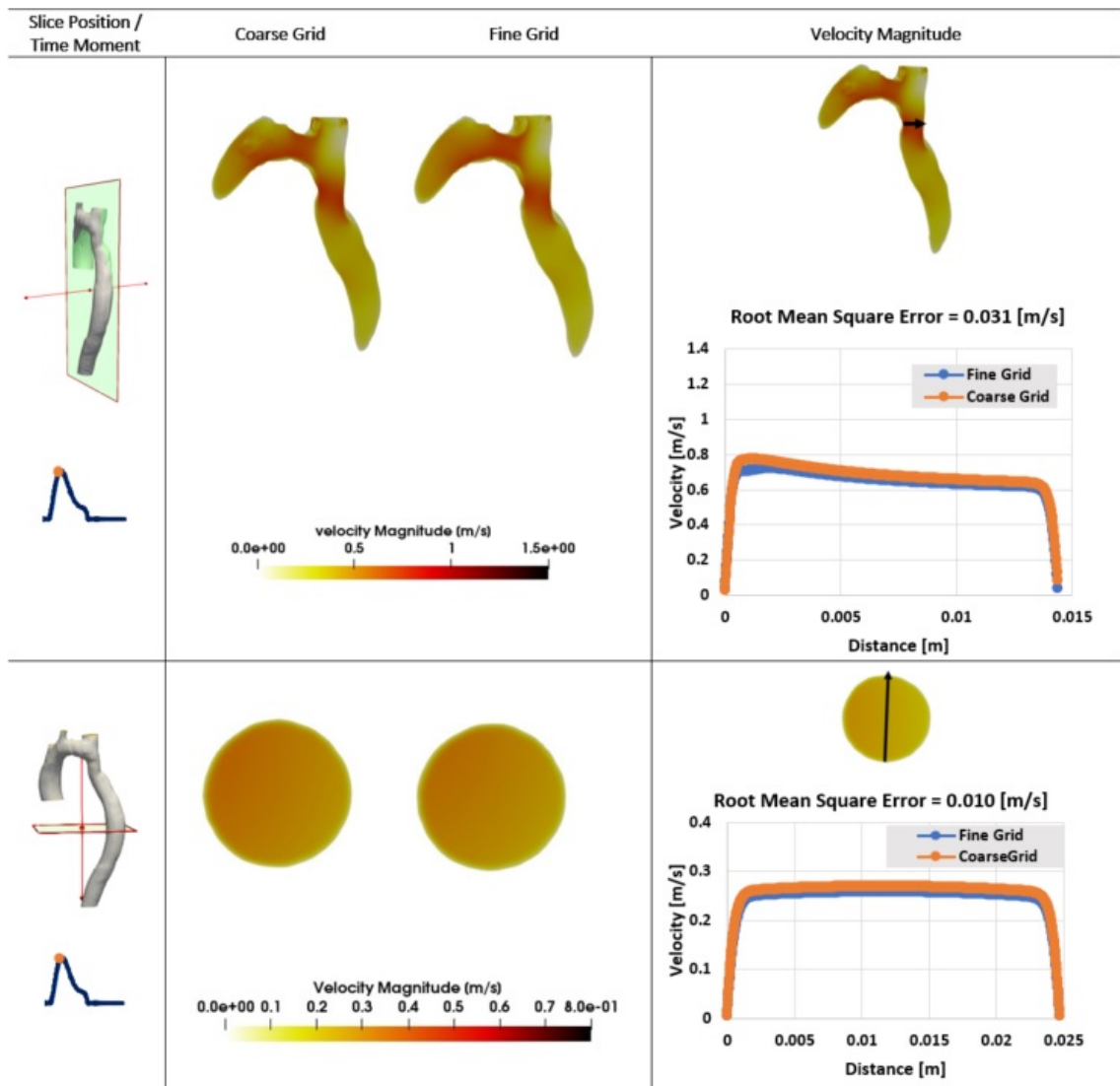


Figure 4.14: Simulation results of the velocity profile in two planes for the pre-intervention case using the coarse and fine grids

the resulted TAWSS for these two grids. As shown in this figure, the qualitative agreement can be seen between the results of the coarse and fine grids. Figure 4.16 is allocated to compare the results of velocity magnitude for the coarse and fine grid in the same slices as used in the time independence study for the post-intervention case. The velocity magnitude was plotted across a line in each of the slices. These lines are in the exact position as the lines used for assessing the time independence study of the post-intervention case. As the plots show, the blood velocity magnitude for the coarse and fine grids are in good agreement for the post-intervention case, showing that the coarse grid is fine enough to depict the blood hemodynamic in this geometry.

4.5 Summary

In this chapter, the geometries utilized for computational modeling of the aortic hemodynamics were presented. In addition, the initial and boundary conditions used in this study were explained, and the meshing method and mesh quality were discussed. The time independence study and mesh independence study were presented for the pre- and post-intervention states to ensure the results are independent of the selected time step and grid size. TAWSS and velocity magnitude in different slices were illustrated for pre- and post-intervention cases to investigate the mesh and time dependence study. In both pre- and post-intervention states, slices were selected in a way that they include the ascending aorta, aortic arch, coarctation site, and descending aorta. These regions are regions of interest in studying the hemodynamics of coarctation of the aorta. Comparing the results of the TAWSS for pre- and post-intervention states showed good qualitative agreement for both grid and time dependence study. The

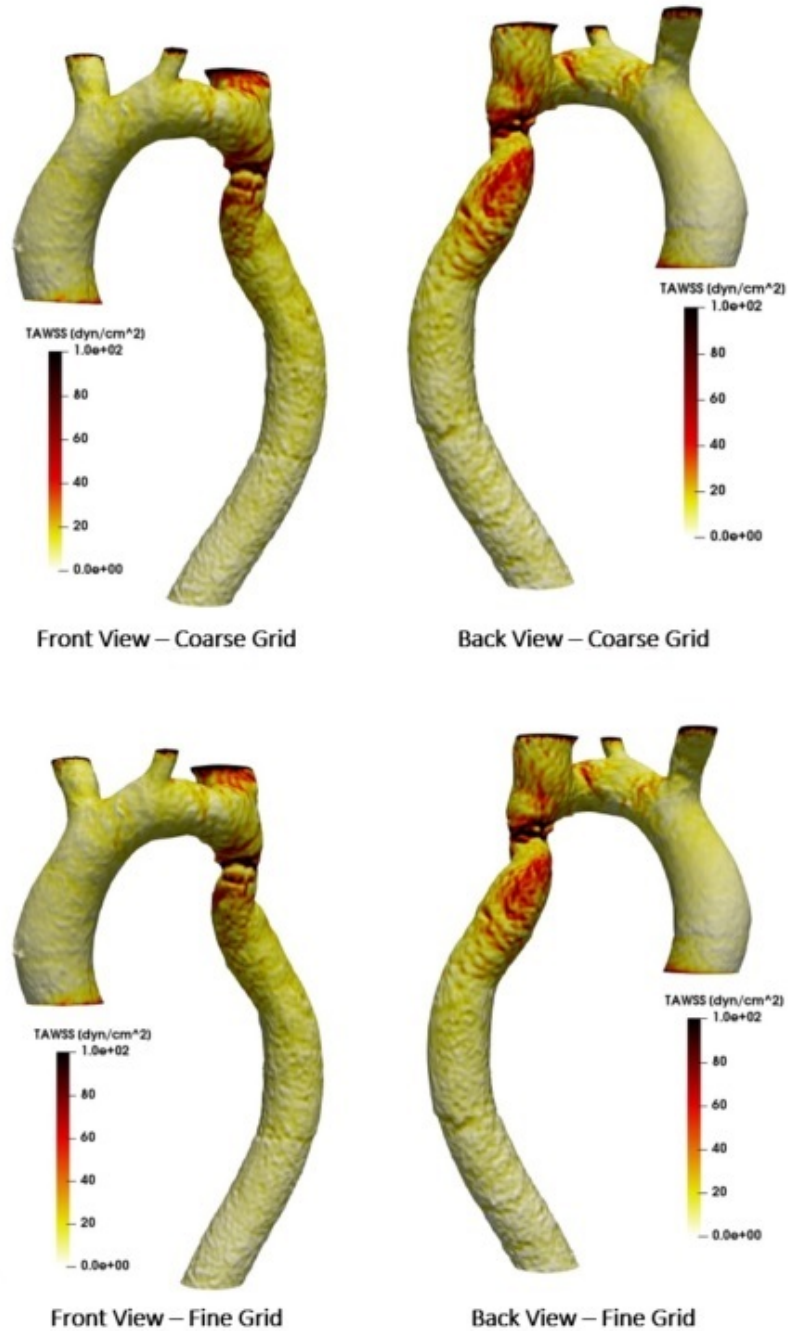


Figure 4.15: Simulation results of the TAWSS for the post-intervention case using the coarse and fine grids

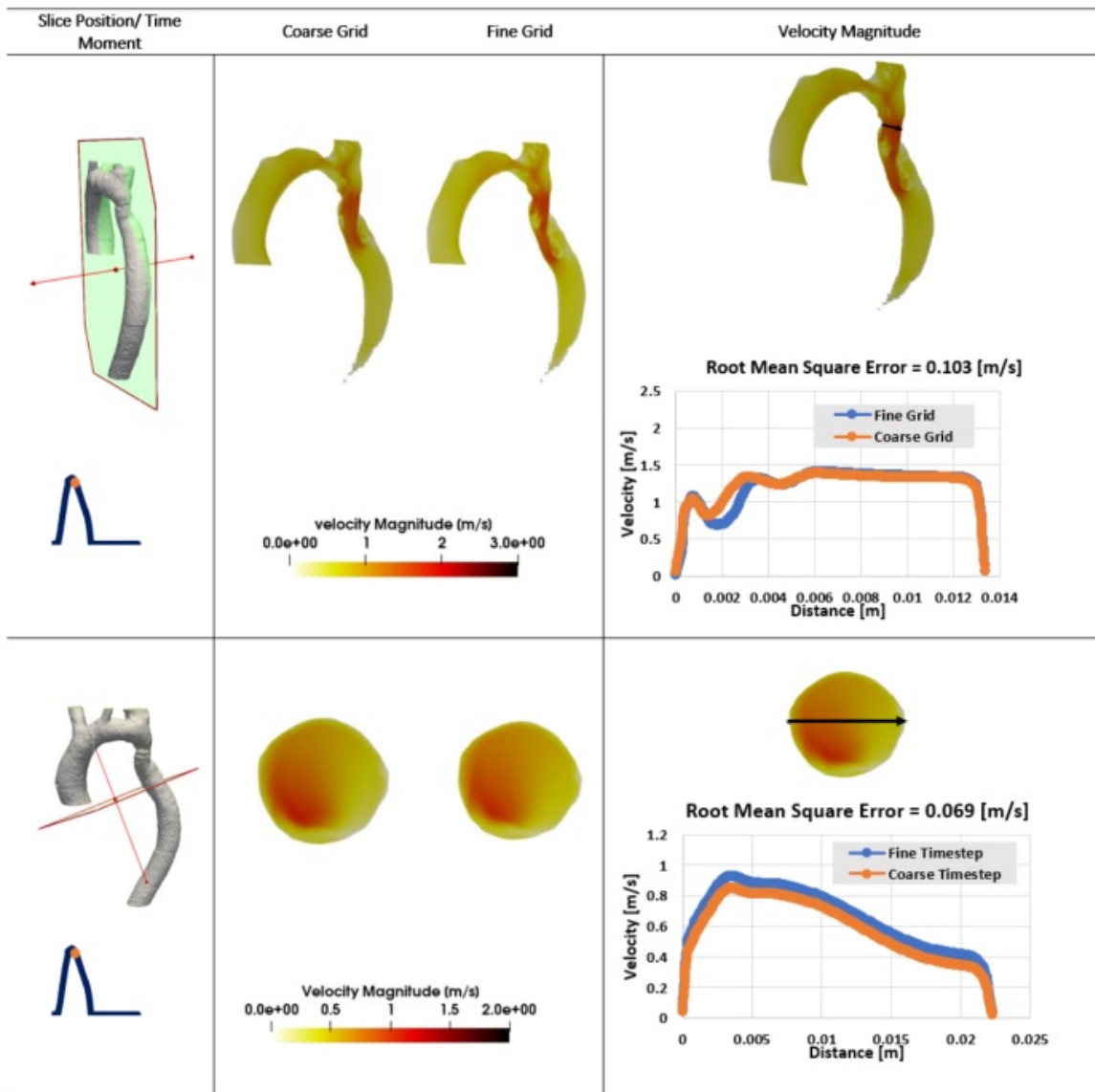


Figure 4.16: Simulation results of the velocity profile in two planes for the post-intervention case using the coarse and fine grids

velocity magnitude was also plotted across different lines for qualitative comparison between the pre- and post-intervention states. The results of the velocity magnitude were in good quantitative agreement for the grid and time dependence study.

Chapter 5

Results and Analysis

Stent-graft implantation is a standard treatment for repairing the coarctation of the aorta. As mentioned earlier, in this method, a catheter is inserted in the coarctation side while carrying a stent graft. The stent is placed and expanded in the coarctation site to keep the aortic wall open. This intervention can alter aortic hemodynamics. Parameters like velocity, pressure, and wall shear stress distribution can be utilized to show this alteration and to assess the success or failure of stent deployment in CoA patients. This chapter represents the results of the computational simulation of the aortic hemodynamics in a patient-specific model for pre- and post-intervention states. These results help us assess the success or failure of stent deployment in this patient with mild coarctation.

The boundary condition applied in the current work is obtained from our in house LPM algorithm [60, 41, 59, 63]. This code was validated against catheter, Echocardiography and MRI data in various publications such as [28, 41, 60, 59, 62]. The code structure utilized in the present study is the same as the one used in [41] for the finite volume simulations. This code structure has been validated against Doppler

echocardiography and catheter data [60, 41, 59, 63].

The convergence criterion is considered less than 10^{-6} for all the residuals during the simulation. Also, all the simulations were checked for the maximum Courant number and $y+$ value. $y+$ is a dimensionless distance normal to the wall, showing the location of the first mesh node near the wall. It is defined as:

$$y+ = \frac{yu_\tau}{\nu} \quad (5.1)$$

where y , u_τ , and ν are the normal distance to the wall, friction velocity, and kinematic viscosity, respectively. The friction velocity is defined as:

$$u_\tau = \sqrt{\frac{\tau_w}{\rho}} \quad (5.2)$$

where τ_w (see equation 5.3) and ρ are wall shear stress and fluid density, respectively. To ensure that the first node center is located inside the viscous sublayer, $y+$ is required to be preferably less than 1. Appendix B represents $y+$ distribution at three time instants of the cardiac cycle for both pre- and post-intervention states. As the simulated results show, $y+$ values are almost always less than 1, guaranteeing acceptable resolution near the vessel wall. The only exception is cutting edges of the three aortic arch branches where are not of our interests.

Appendix C shows the maximum courant number (Co) over a cardiac cycle for pre- and post-intervention states. the cutting edges explained above are exempted from the simulated results. As the graphs show, the maximum courant numbers for both states are less than 1, improving the accuracy of the simulated results.

5.1 Velocity Distribution

Aorta is characterized by a complex morphology and structure. It contains branching (Brachiocephalic Artery, Left Common Carotid Artery, and Left Subclavian Artery), tapering, and curving. These structural complexities alongside the pulsatile nature of the blood flow make the hemodynamics factors like the velocity distribution in the aorta a complex phenomenon. This complexity is even more in the presence of aortic diseases like coarctation of the aorta. Aortic flow distribution is identified as a parameter that may affect the cellular development of the aortic wall [2]. So, studying the hemodynamics of arterial blood flow is of paramount importance in diagnostic and treatment procedures. This section aims to investigate the velocity distribution of the blood flow in a patient-specific aorta in the presence of mild coarctation. In this regard, the time-varying trans-plane velocity distribution and the blood flow streamline are presented and compared in the pre- and post-intervention states.

5.1.1 Trans-plane Instantaneous Velocity Distribution

The impact of highly disturbed blood on aortic diseases has been proved in several studies [160, 161, 162]. This correlation is remarkable in the aortic arch branches and bending of the descending aorta, which are characterized by highly disturbed hemodynamic factors [26]. The simulated results of the velocity distribution in longitudinal cutting planes are presented in Figure 5.1 for pre- and post-intervention states to investigate the impact of the intervention on the hemodynamic factors. These planes cut the middle of the coarctation site, crossing the ascending and descending aorta. The velocity distribution is shown at three time instants: t_1 (at acceleration phase), t_2 (at peak systole), and t_3 (at deceleration phase).

The simulation results show that the velocity is characterized by time-varying and asymmetric distribution across the cutting planes in both geometries. The highest values of velocity magnitude are found at the peak systole and late systole in both states. Aortic arch and coarctation site are presenting the highest velocity magnitude in both states. The post-intervention state even presents a much higher maximum velocity magnitude during the cardiac cycle in these locations. Also, the velocity magnitude at the necking of the coarctation site is remarkably higher at the peak systole and late systole following the intervention. The curvatures in the aortic arch and descending aorta pushes the blood flow towards the outer wall due to the centrifugal forces. However, coarctation in the aorta forms a high-velocity flow jet right after the obstruction that hinders the flow to exactly follow the outer wall curvature. Figure 5.1 shows this jet in both states at the peak systole. The maximum jet velocities after the coarctation site are $1.35 \left[\frac{m}{s} \right]$ and $1.71 \left[\frac{m}{s} \right]$ for pre- and post-intervention states, respectively. These results show a 26.7% increase in the maximum velocity magnitude following the intervention. Generally, the simulation results do not show improvement in the reduction of velocity magnitude across the coarctation site in the post-intervention state, raising the concern of applying successive intervention in this patient.

5.1.2 Instantaneous Blood Flow Streamline

As discussed in chapter 2, the flow patterns in a healthy aorta during the cardiac cycle range from axial pattern during the early systole, to complex helical shapes during the mid to late systolic phase. Forming the helical flow pattern in the aorta is hypothesized by several factors: 1) position of LV muscle fibers that results in a

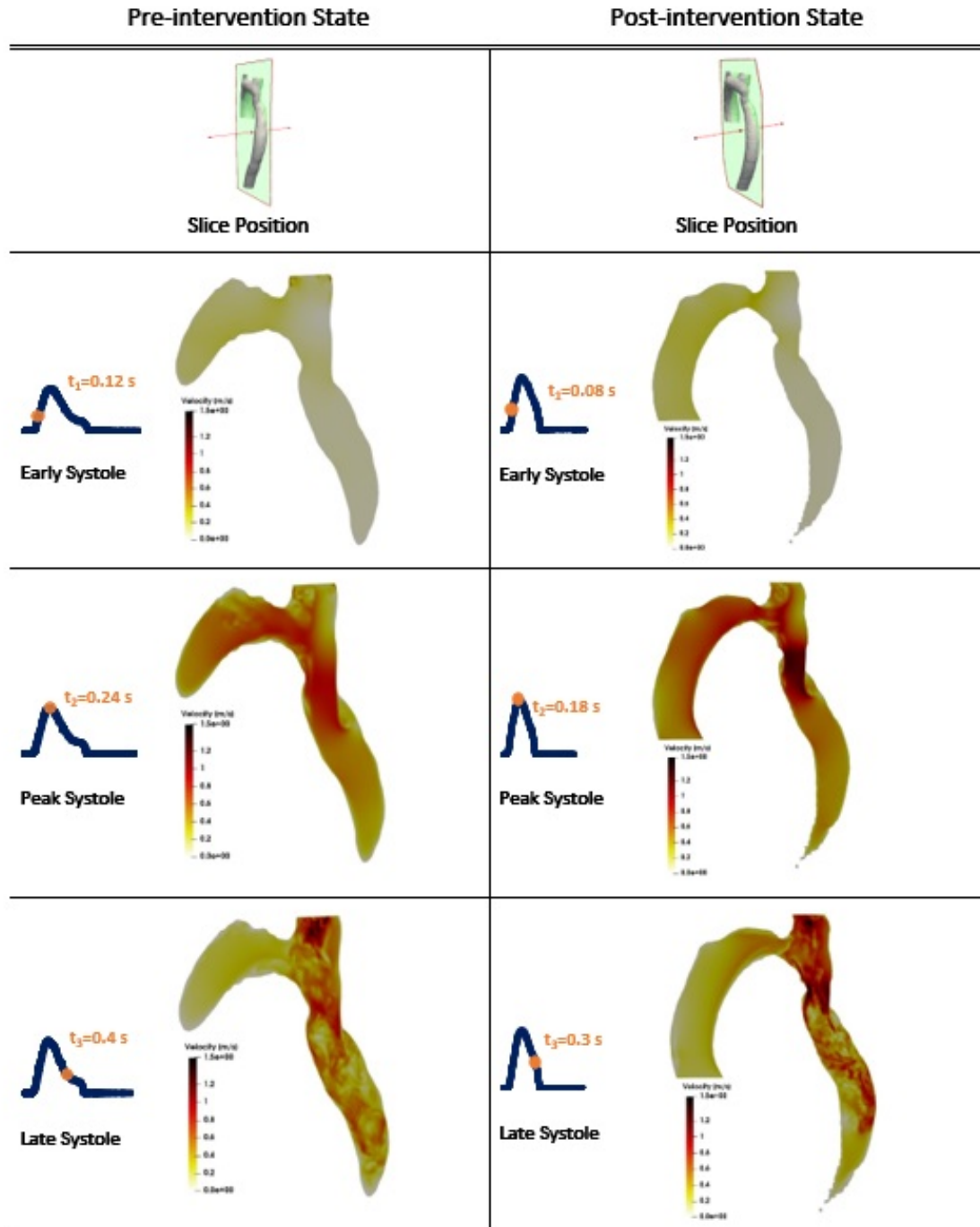


Figure 5.1: Simulation results of instantaneous velocity distribution in the longitudinal cutting plane for pre- and post-intervention states - velocity magnitude ranges from 0 to $1.5 \left[\frac{m}{s} \right]$ in all the images presented here.

counterclockwise twist of these muscles during systole and their clockwise return during diastole, 2) aortic valve opening and closure, and 3) anatomical complexity of the aorta [2]. Although the helical flow pattern is expected in a healthy aorta, additional helical velocity components may impact endothelial cell alignment, development of atherosclerosis, and aortic dissection [163]. It can also affect the pathogenesis of atheroma in the aortic arch [164]. The effect of radial velocity component on the adhesion of monocytes to the vessel wall is another concern investigated in some studies [165].

Figure 5.2 shows the results of the simulated velocity streamlines in pre- and post-intervention states at three time instants: t_1 (at acceleration phase), t_2 (at peak systole), and t_3 (at deceleration phase). In early systole, the difference between the flow streamlines before and after the intervention is not considerable. At this time, velocity streamlines follow an axial pattern almost everywhere in the aorta. However, remarkable differences can be seen between the velocity pattern and magnitude before and after the intervention states in peak systole and late systole. In peak systole, the velocity magnitude in the aortic arch and coarctation site is much higher than in other places in the aorta in the pre-intervention state. These sites with the high-velocity magnitude expand to the ascending aorta and descending aorta following the intervention during the peak systole. Also, simulation results show the increase in the velocity magnitude in these places after the intervention. In the late systole, helical flows are a noticeable phenomenon primarily occurring around the coarctation site. As Figure 5.2 shows, the velocity magnitude increases in the coarctation site following the intervention, and the helical flow occupies more regions in the descending aorta. In the distal part of the descending aorta, axial flow pattern exists in both states;

however, the simulation results show a rise in the velocity magnitude in this part of the aorta after stent implantation.

5.2 Wall Shear Stress Distribution

Endothelial cells (ECs) form the inner lining of the arterial wall. Since these cells are in contact with the blood flow, responses of these cells alter by changing the local hemodynamic factors like wall shear stress [2]. WSS is defined as the shear stress imposed by the blood flow on the vessel wall:

$$\tau_w = \mu \left(\frac{\partial u}{\partial y} \right)_{y=0} \quad (5.3)$$

where μ , u , and y are the dynamic viscosity, flow velocity parallel to the wall, and normal distance to the wall, respectively. Various studies have reported the influence of changes in WSS on arterial wall diseases. Some of them point to the effect of high WSS as a stimulator for the arteriogenesis (growth of collateral arteries) [161]. Another studies show the impact of low WSS on the incidence of atherosclerosis (plaque build-up inside arteries that leads to the hardening and narrowing of the arteries) [166]. Plaque fracture that may lead to embolization and arterial occlusion is another problem that can be induced by the WSS [102]. Thromboembolic and hemolysis are other possible complications associated with high levels of WSS [79]. Considering the importance of WSS on cardiovascular diseases, this section aims to compare the pre- and post-intervention WSS and its corresponding parameters to assess the success of stent deployment in a patient with CoA.

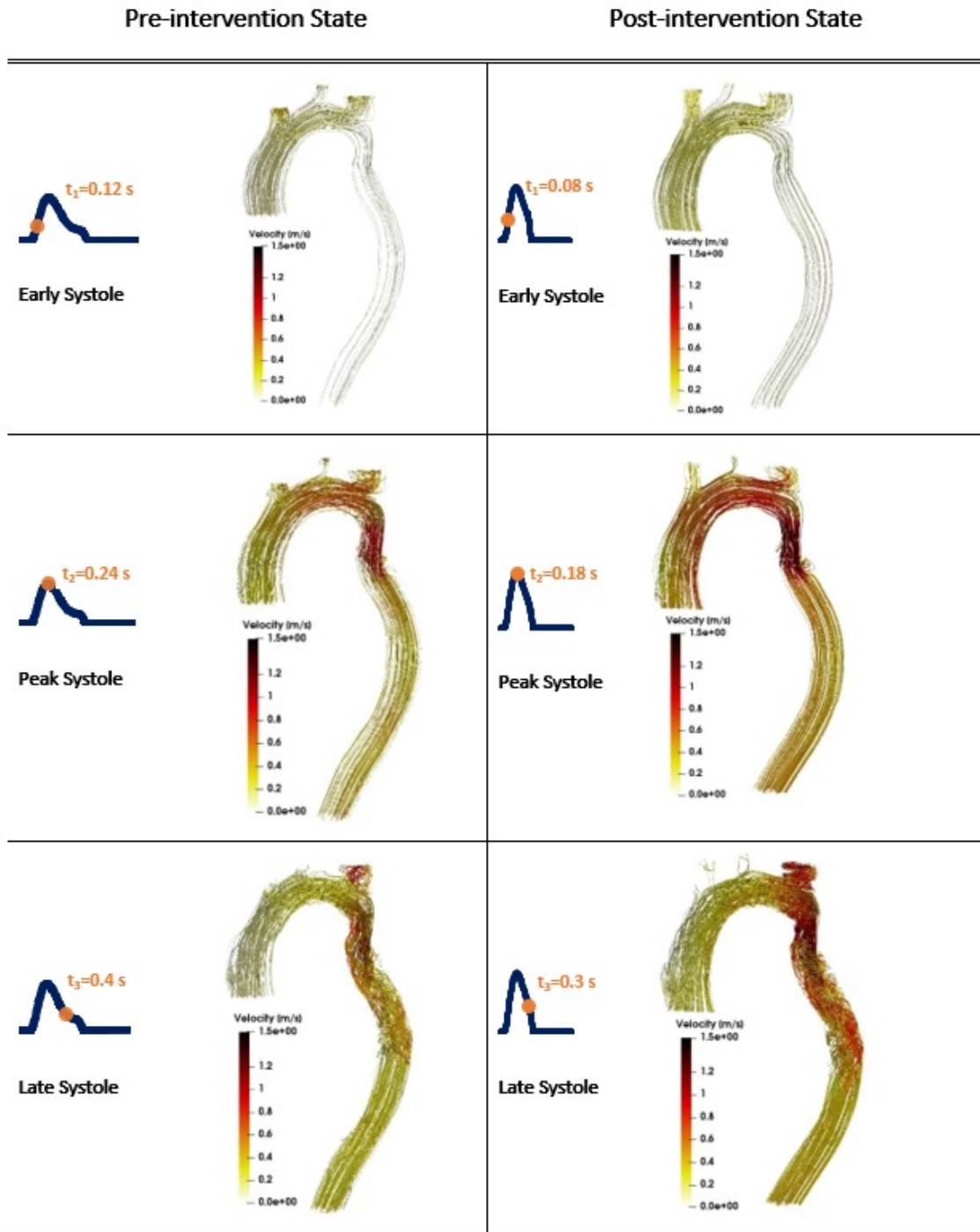


Figure 5.2: Simulation results of instantaneous velocity streamlines in three various time instants for pre- and post-intervention states - velocity magnitude ranges from 0 to 1.5 $\left[\frac{m}{s}\right]$ in all the images presented here.

5.2.1 Time-varying Spatial Distribution of Wall Shear Stress

As discussed above, WSS has a considerable effect on arterial wall diseases. So, many studies have attempted to address WSS distribution on the arterial wall during the cardiac cycle. Given that MRI has a limited temporal resolution, attempts to calculate WSS with MRI data are accompanied by limited success [4, 167, 168]. So CFD can be a viable alternative to imaging data for obtaining WSS in patient-specific arterial walls. The results of WSS for the pre- and post-intervention cases using CFD simulation are presented in Figure 5.3. The results are compared in three different time instants: t_1 (at acceleration phase), t_2 (at peak systole), and t_3 (at deceleration phase). Comparing the results shows that the post-intervention state is accompanied by the overall increase in WSS in three mentioned time instants. The difference is more noticeable at the peak systole and deceleration phase between pre- and post-intervention states. As these figures show, the coarctation site witnesses a high value of the WSS in both pre- and post-intervention cases.

As reported in [4], peak wall shear stress that can be seen in the aortic arch and branches in the early systole and peak systole are 150 and 260 $\left[\frac{\text{dyn}}{\text{cm}^2}\right]$, respectively. Pre- and post-intervention cases were studied here to see the peak WSS values during the early systole and peak systole shown in Figure 5.3 at three time instants. The simulation results are summarized in Table 5.1 to be compared with the results reported in [4]. Note that the tips of the aortic arch branches were ignored from the analysis to avoid the errors associated with cutting the tip of the branches. As shown in this table, the typical peak WSS values were higher than all the WSS values for the pre- and post-intervention cases except for the peak systole in the post-intervention case. This comparison shows that peak WSS exceeds the typical peak WSS shown in

Table 5.1: Peak WSS in the aortic arch and branches in the pre-intervention, and post-intervention states in current study, as well as the typical values of WSS in a healthy thoracic aorta model (as reported in [4])

| <i>Time</i> | <i>Peak WSS</i> $[\frac{dyn}{cm^2}]$ <i>in</i> <i>Pre-intervention State</i> | <i>Peak WSS</i> $[\frac{dyn}{cm^2}]$ <i>in</i> <i>Post-intervention State</i> | <i>Typical Peak WSS</i> $[\frac{dyn}{cm^2}]$ |
|----------------------|---|--|---|
| <i>Early Systole</i> | 77 | 96 | 150 |
| <i>Peak Systole</i> | 237 | 346 | 260 |

this table following the intervention.

5.2.2 Spatial Distribution of time-averaged Wall Shear Stress

Time-averaged wall shear stress is defined as the averaged shear stress exerted on the inner layer of the aorta over the whole cardiac cycle:

$$TAWSS = \frac{1}{T} \int_0^T |\tau_w| dt \quad (5.4)$$

where T and τ_w are the cardiac cycle period and instantaneous wall shear stress, respectively. TAWSS for the pre- and post-intervention states are presented in Figure 5.4 a and b. Comparing the results of TAWSS for pre- and post-intervention states show the overall increase in TAWSS values in the post-intervention state. This increase is more considerable in the areas of interest around the coarctation site and is shown by dash lines in these figures. The comparison between the TAWSS values in these areas of pre-intervention and post-intervention states is presented in a histogram in Figure 5.4 c. As this histogram shows, the percentage of areas exposed by

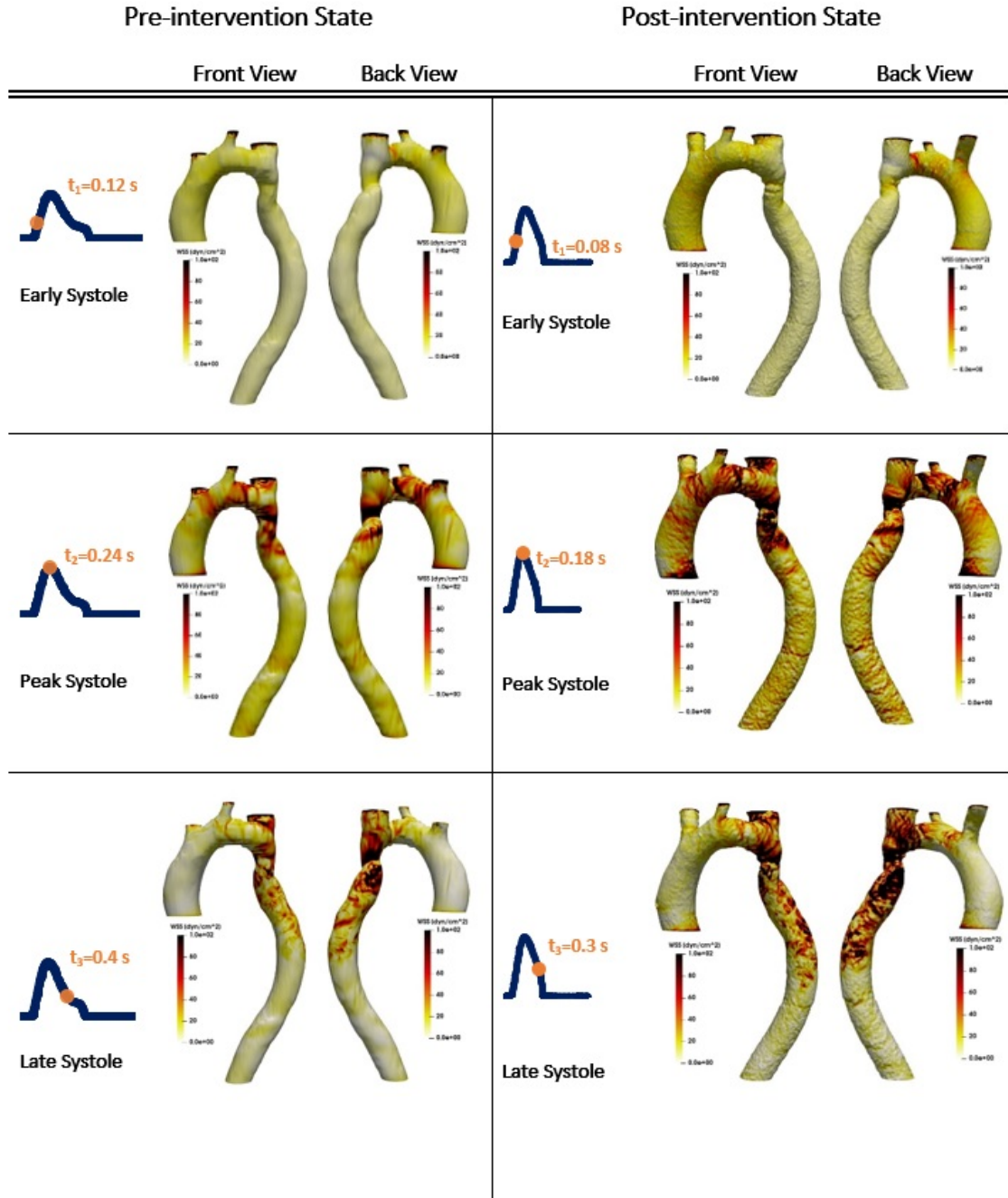


Figure 5.3: Simulation results of WSS in three various time instants for pre- and post-intervention states – WSS magnitude ranges from 0 to 100 $\left[\frac{dyn}{cm^2} \right]$ in all the images presented here.

the TAWSS values less than $40 \left[\frac{\text{dyn}}{\text{cm}^2} \right]$ is almost identical between the pre- and post-intervention states. The only exception is the decrease in the percentage of areas with TAWSS values between 10 and $20 \left[\frac{\text{dyn}}{\text{cm}^2} \right]$ for the post-intervention state. However, the results show a remarkable increase in the percentage of areas exposed by TAWSS values of more than $40 \left[\frac{\text{dyn}}{\text{cm}^2} \right]$ for the post-intervention state. This increase in the areas with high TAWSS values results in a higher risk of damage to the vessel wall due to rupture, aneurysm, or dissection. The peak of TAWSS in the area of interest for the pre- and post-intervention states were 91 and $186 \left[\frac{\text{dyn}}{\text{cm}^2} \right]$, respectively. The increase in the peak TAWSS values in the areas of interest confirms the higher risk of damage to the vessel wall following the intervention.

5.2.3 Space-averaged Time-averaged Wall Shear Stress

To further assessment of the effects of the intervention, TAWSS was spatially averaged as follows:

$$SA - TAWSS = \frac{1}{A_{Ao}} \sum_{i=1}^n (TAWSS_i \times A_{mi}) \quad (5.5)$$

where the A_{Ao} , i , and A_{mi} are the total area of the aortic wall, the index of the surface mesh, and the area of the i th mesh surface, respectively.

Post-processing of the simulation results shows that the spaced-averaged time-averaged wall shear stress (SA-TAWSS) exerted on the whole aorta for the pre- and post-intervention states are 12.8 and $14 \left[\frac{\text{dyn}}{\text{cm}^2} \right]$, respectively. Comparing these values indicates the overall increase in spatio-temporal wall shear stress following the intervention. Figure 5.5 shows the SA-TAWSS values for the ascending aorta, aortic arch, and descending aorta before and after the intervention. The results of SA-TAWSS of the aortic arch and descending aorta are much larger than that of the ascending

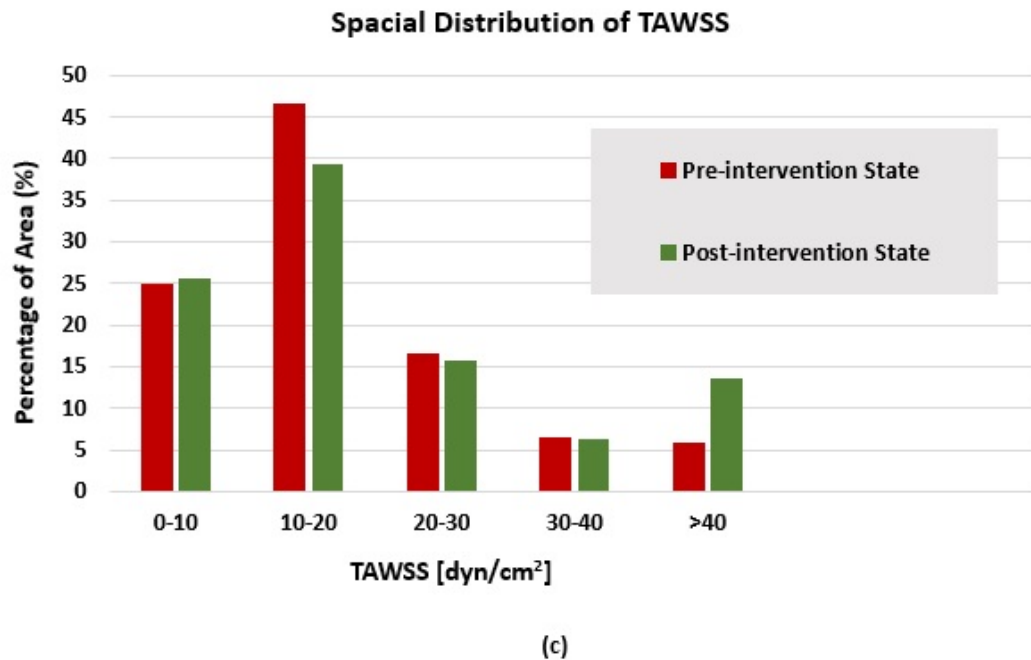
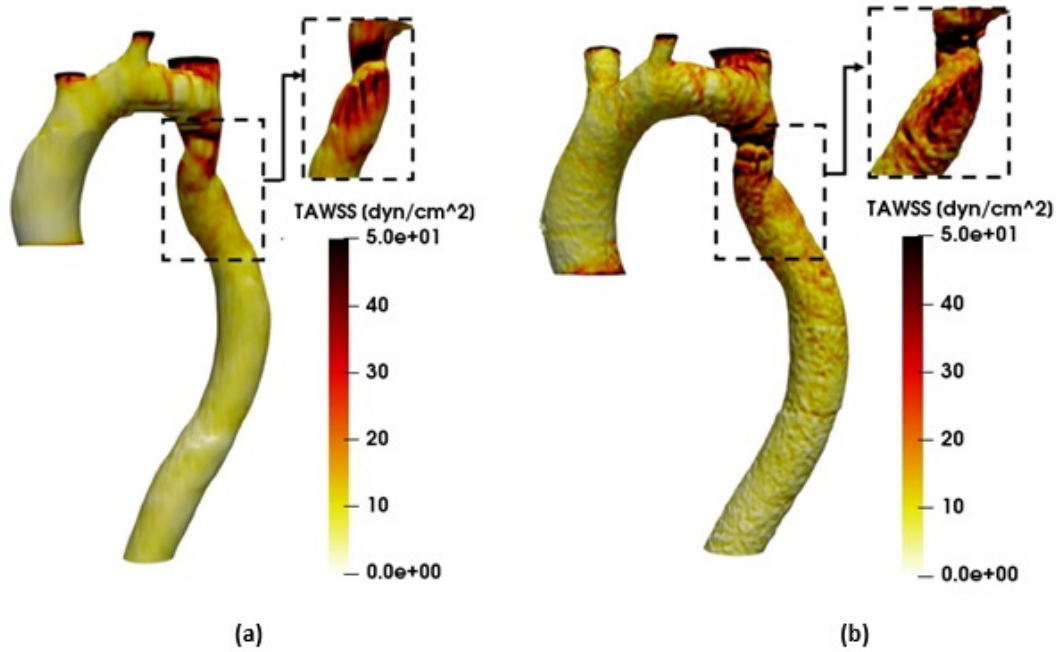


Figure 5.4: Simulation results of a) TAWSS in the pre-intervention state, b) TAWSS in the post-intervention state, and c) spatial distribution of TAWSS in areas shown by dash lines for pre- and post-intervention states – WSS magnitude ranges from 0 to 50 ($\frac{dyn}{cm^2}$) in all the images presented here.

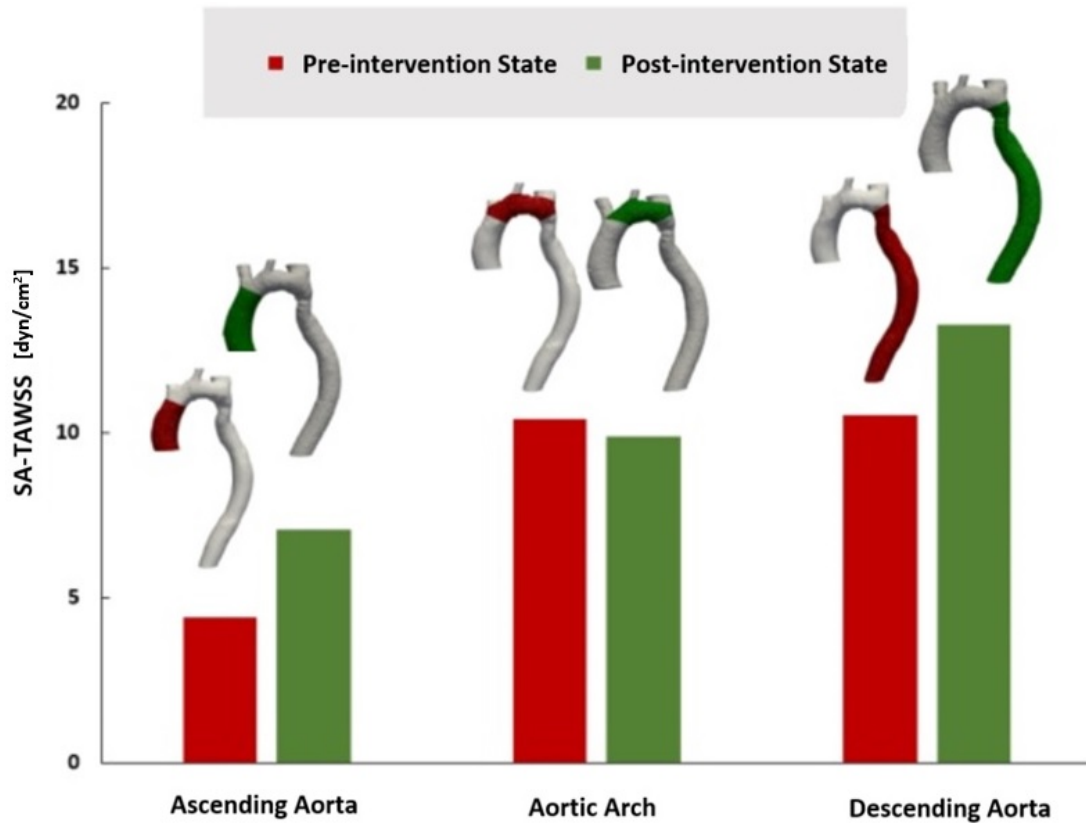


Figure 5.5: Simulation results of SA-TAWSS in ascending aorta, aortic arch, and descending aorta for pre- and post-intervention cases

aorta in each of the pre- and post-intervention cases. As this histogram shows, the SA-TAWSS value of the aortic arch for the post-intervention state decreased slightly. However, SA-TAWSS for the ascending aortic and descending aortic segments increased remarkably.

5.3 Pressure Distribution

Pressure distribution across the aorta is a major hemodynamic factor in assessing the patient's health condition. In CoA patients, the obstruction in the aorta results in a

pressure drop across the coarctation site. This pressure drop imposes more load on the LV to transfer the oxygen-rich blood through the aorta to the body organs. This extra workload may even lead to heart failure in some patients. For clinical diagnosis purposes, the pressure gradient of more than 20 [mmHg] is the hallmark of the presence of severe coarctation. Cardiac catheterization is utilized for the evaluation of the peak systolic pressure gradient across the coarctation site clinically. However, this method is invasive and associated with the risk of rupture or damage to the vessel wall. So, this method is not practical for all patients in their recurrent follow-up examinations. These limitations underscore the importance of CFD study in non-invasive assessment of the severity of CoA, evaluation of treatments, and deciding about the timing of the intervention. This section is allocated to present the CFD results of pressure distribution and pressure gradient in a CoA patient for pre- and post-intervention states.

5.3.1 Trans-plane Time-varying Spatial Pressure Distribution

The simulation results of time-varying pressure distribution for the pre- and post-intervention cases are presented in Figure 5.6. In this figure, the pressure distribution in a plane crossing the coarctation site is shown in three different time instants: t_1 (at acceleration phase), t_2 (at peak systole), and t_3 (at deceleration phase). The planes were selected in a way that they contain the coarctation site and far as possible from the vessel wall to eliminate the effects of boundary conditions on the simulation results. As this figure shows, the blood pressure reduces after passing the coarctation site. Comparing the simulation results for pre- and post-intervention states show that

the pressure reduction did not improve following the intervention.

5.3.2 Maximum Trans-coarctation Pressure Gradient

Maximum pressure gradient across the coarctation site has a crucial role in the evaluation of coarctation severity in CoA patients. Patients with a maximum systolic pressure gradient of more than 20 [$mmHg$] are possible candidates for the interventional treatments. As mentioned earlier, cardiac catheterization is an invasive method with high risks and expense to evaluate the coarctation severity. Therefore, CFD analysis may be a viable alternative to imaging modalities for obtaining pressure gradient in patient-specific arterial walls.

The maximum systolic pressure gradient was obtained in the present study by calculating the maximum pressure drop before and after the coarctation site over a cardiac cycle in pre- and post-intervention states. The calculation results are presented in Figure 5.7. As this figure shows, the maximum pressure drop occurs in the systolic phase for both pre- and post- intervention states. Comparing the results of the two states shows that the pressure gradient slightly reduced following the intervention. The maximum trans-coarctation pressure gradient for the pre- and post-coarctation states are 8.3 and 6.5 [$mmHg$], respectively. The results reveal that the stent deployment could not remove the pressure drop completely. This might be due to problems like malapposition of the stent and inappropriate stent expansion. A decrease in the vessel wall compliance and distensibility following stent implantation may also affect the desirable results.

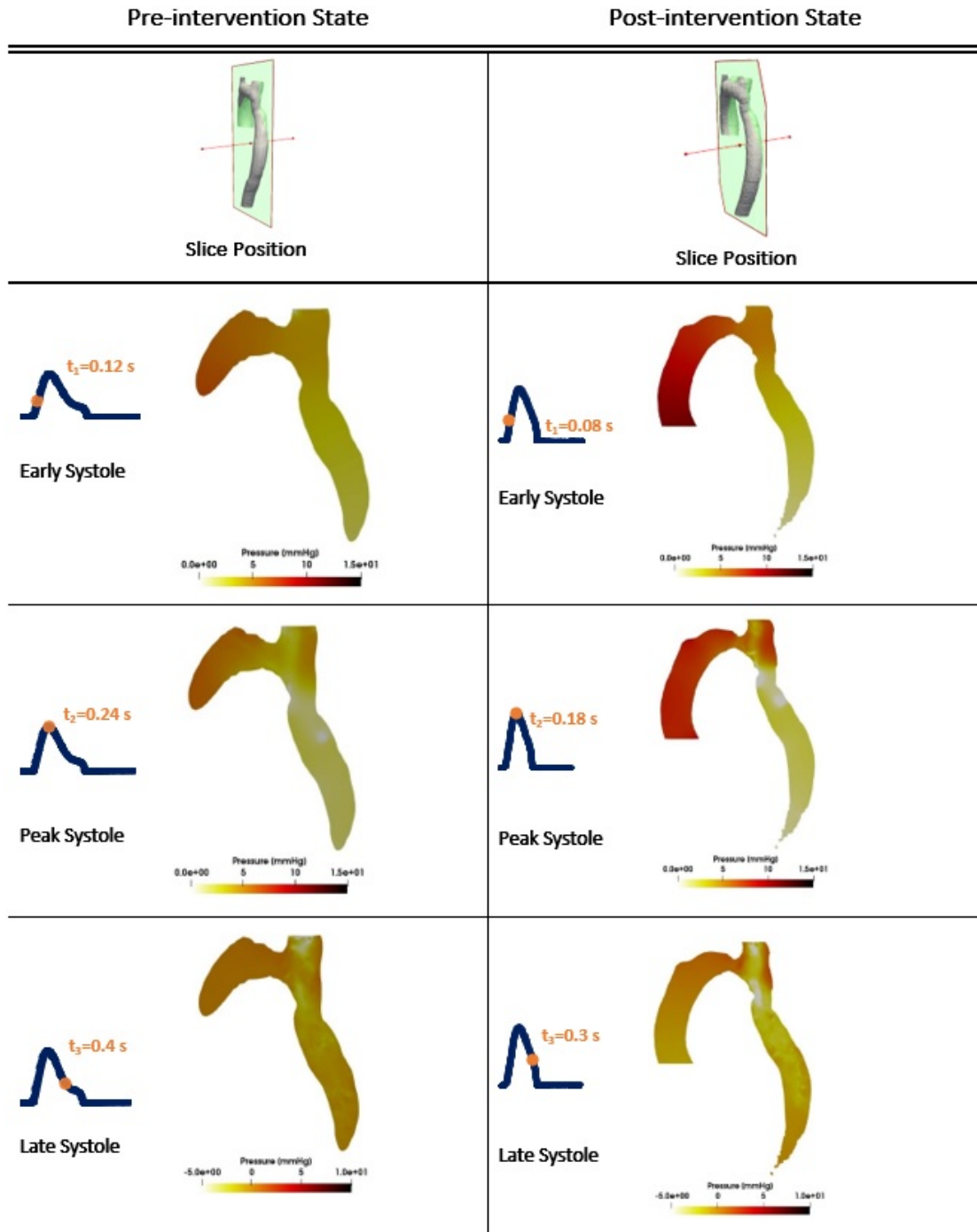


Figure 5.6: Simulation results of instantaneous pressure distribution in in longitudinal cutting plane for pre- and post-intervention states - pressure magnitude ranges from 0 to 15 [mmHg] in early systole and peak systole, and from 0 to 10 [mmHg] in late systole

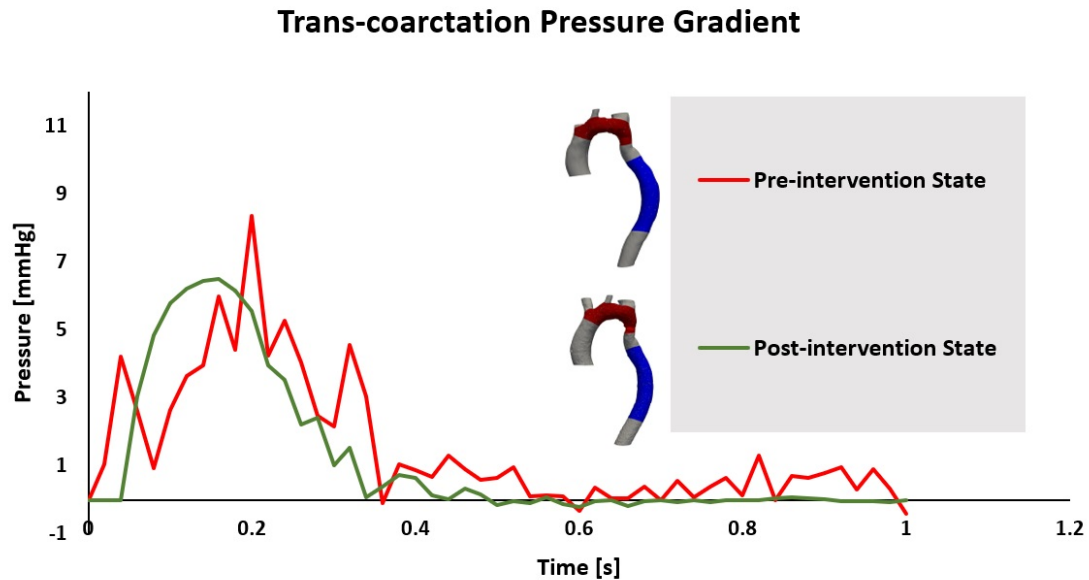


Figure 5.7: Simulation results for the pressure gradient across the coarctation site over a cardiac cycle for pre- and post-intervention cases

5.4 Summary of Results

This chapter was allocated to investigate the effects of stent deployment on aortic hemodynamics in a patient with mild coarctation of the aorta. In this regard, first, the influence of hemodynamics factors such as velocity distribution, wall shear stress, and pressure drop on aortic diseases was explained. Then, simulated results of these hemodynamics factors were illustrated, and the results in pre- and post-intervention states were compared. As the results show, despite a slight decrease in the trans-coarctation pressure gradient in the post-intervention state, velocity and wall shear stress distribution do not show overall improvement following the intervention, raising the concern of applying a successful intervention in this patient with mild coarctation.

Chapter 6

Conclusions and Recommendations

6.1 Conclusions

Although stent deployment is a standard treatment in CoA patients, it is associated with several problems that affect the intervention's success. Stent displacement, inappropriate expansion of the stent, and applying a stent with the wrong size are examples of the mentioned problems. The unique aortic geometry of a patient and the coarctation index are also important parameters in selecting the suitable treatment. The present study investigated the effect of stent implantation in a patient with mild coarctation of the aorta.

First, the velocity distribution in this patient was investigated as a crucial hemodynamic factor in the progression of aortic diseases. The simulation results reveal that post-intervention velocity magnitude in the aortic arch and coarctation site is generally larger than that of the pre-intervention states in these locations. Besides,

maximum velocity magnitude after the coarctation site shows a 26.7% increase following the intervention. Studying the velocity streamlines before and after the intervention indicates that although these two states have similar axial flow pattern during early systole, noticeable differences in terms of the velocity magnitude and pattern between the two states are evident in peak and late systole.

Time-averaged wall shear stress was calculated in the vicinity of the coarctation for the pre- and post-intervention states. Comparing the results shows that more areas around the coarctation in the post-intervention state are subject to TAWSS values more than 40 [dyn/cm²]. This finding reveals that the post-intervention state is associated with a higher risk of rupture in the vessel wall around the coarctation site. Also, the peak TAWSS value in these areas was higher in the post-intervention state, which confirms the higher risk of damage to the vessel wall. The simulation results of the SA-TAWSS were compared for the pre- and post-intervention states. The results show a 9.3% increase in the SA-TAWSS values over the whole aorta following the intervention. Also, the aortic arch segment shows a slight decrease in SA-TAWSS after the intervention; however, the ascending aorta and descending aorta witnessed a considerable increase in the SA-TAWSS values following the intervention.

Maximum trans-coarctation pressure drop was evaluated over the cardiac cycle for both pre- and post-intervention states. As the simulated results show, the maximum pressure drop occurs during the systolic phase for both states. Simulated results also show a slight reduction in the maximum pressure drop following the intervention.

Although results indicated a slight decrease in the maximum pressure drop across the coarctation site in the post-intervention state, the results of wall shear stress and velocity distribution did not improve following the intervention. Based on the

presented results, the stent deployment was not successful as it could not considerably improve the aortic hemodynamic conditions. So, further treatment is suggested in this patient to improve the cardiac function. The results also show the ability of computational fluid dynamics, as an alternative tool, to assist the clinical diagnosis and compensate for imaging modalities' limitations. Using the CFD, hemodynamic parameters like wall shear stress and pressure drop can be evaluated, and the success or failure of stent deployment can be assessed. This research also raises the concern of stent deployment in patients with the mild coarctation of the aorta. However, studies on a large group of patients with mild coarctation of the aorta and long-term follow-up in these patients are required to improve decision-making strategies for the suitable treatment of choice in these patients.

6.2 Limitations and Future work

The current work is subject to some limitations as follows:

1. Aortic blood hemodynamics was investigated in one patient with mild coarctation in this work. Considering the high sensitivities of aortic hemodynamics to the patient-specific aortic morphology and boundary conditions, the results of the present study cannot be fully applicable to other cases with mild coarctation. As a result, more studies should be performed on a large group of patients with mild coarctation to assess the success of stent deployment in this group of patients.
2. Simulations were run over one cardiac cycle. Running the simulations for more than one cardiac cycle is required to eliminate the effects of initial conditions.
3. In the present work, blood was assumed as a Newtonian fluid with a dynamic viscosity of 3.15 E-3 [Pa.s] . More investigations should be done to see the effects of

considering the blood as a non-Newtonian fluid and different dynamic viscosity values on the simulation results.

4. The assumption of a rigid wall is considered in this thesis. This assumption is proved to be a realistic one in literature, especially in CoA patients who are usually subject to hypertension and reduced compliance in the aorta. However, there is still room for investigating the effects of considering the fluid-structure interaction model on the simulation results for patients with mild coarctation of the aorta.

Appendix A

Mesh Skewness and Orthogonal Quality

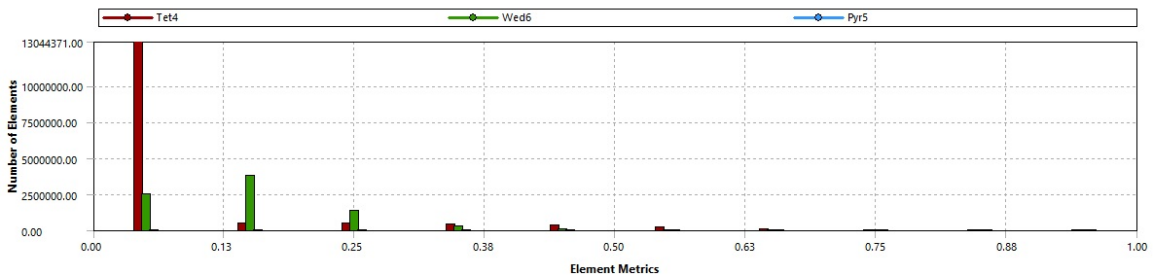


Figure A.1: Mesh Skewness for Pre-intervention Case, Mesh No. 2

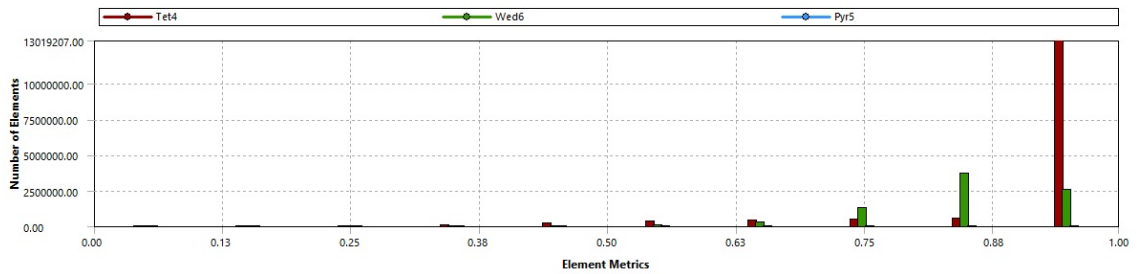


Figure A.2: Mesh Orthogonal Quality for Pre-intervention Case, Mesh No. 2

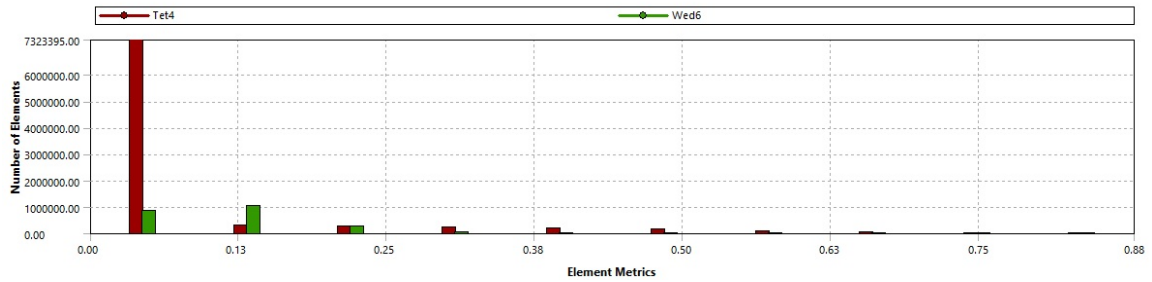


Figure A.3: Mesh Skewness for Post-intervention Case, Mesh No. 1

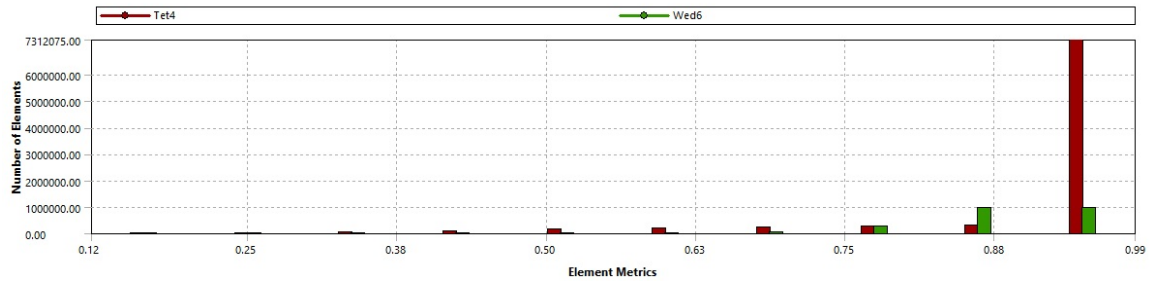


Figure A.4: Mesh Orthogonal Quality for post-intervention Case, Mesh No. 1

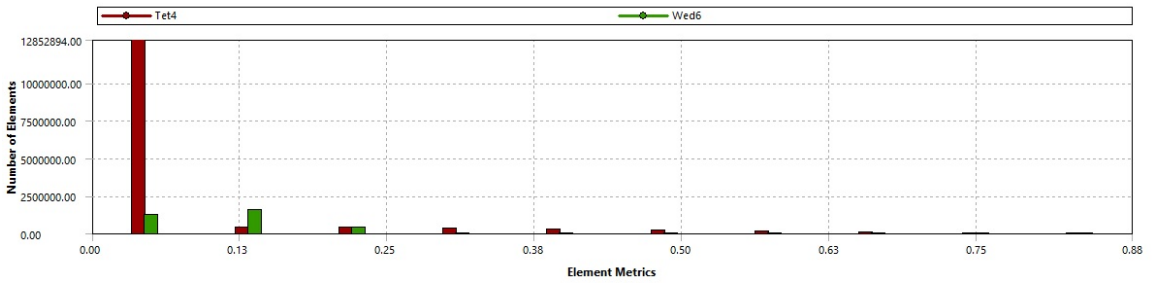


Figure A.5: Mesh Skewness for Post-intervention Case, Mesh No. 2

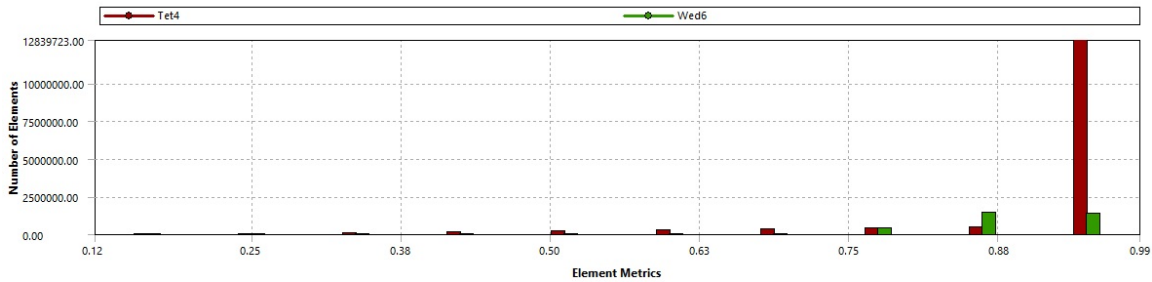


Figure A.6: Mesh Orthogonal Quality for post-intervention Case, Mesh No. 2

Appendix B

y_+ Distribution

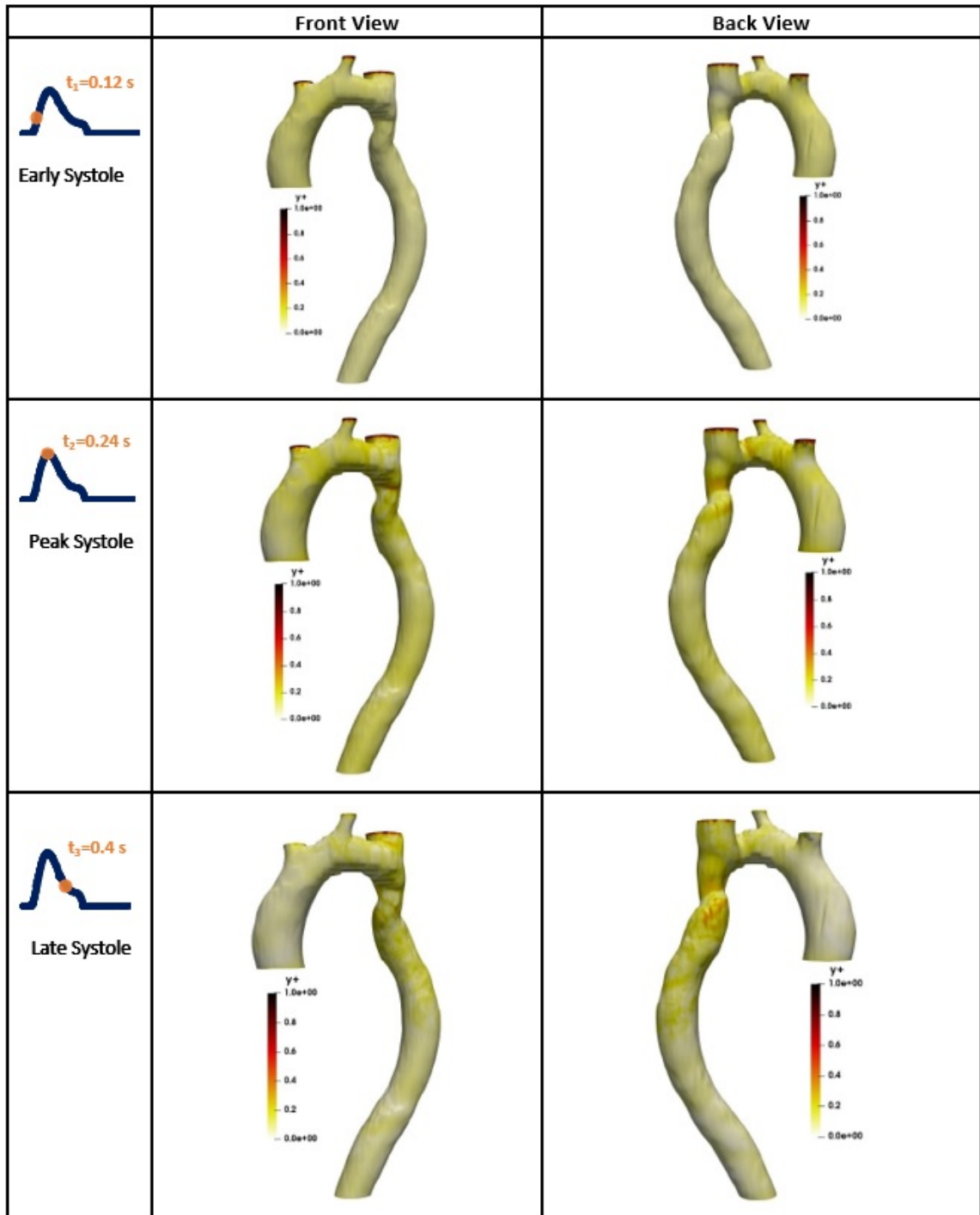


Figure B.1: y^+ Distribution for Pre-intervention state, Mesh No. 1, Time Step = $0.8\text{E-}6\text{ s}$ - y^+ ranges from 0 to 1 in all the images presented here.

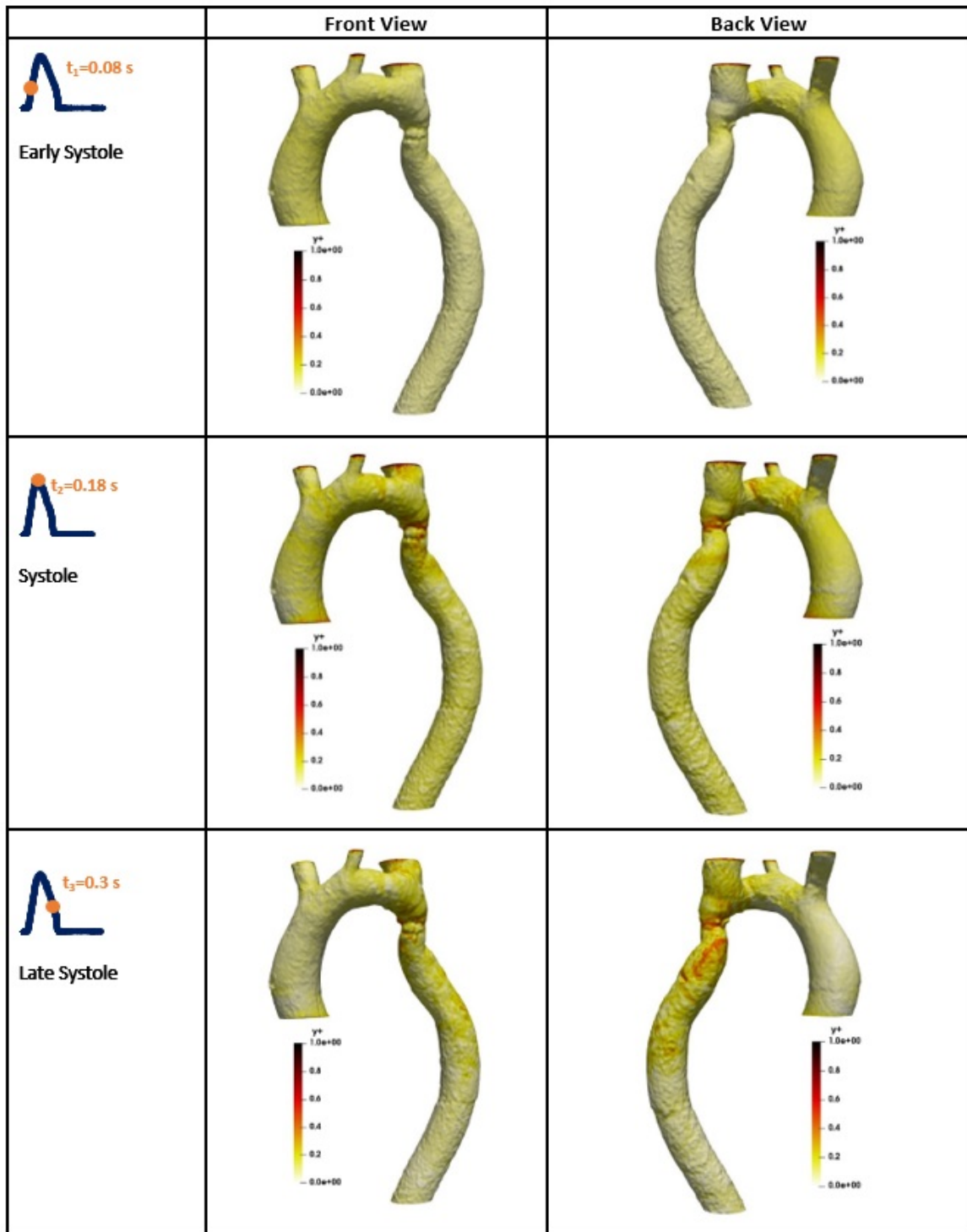


Figure B.2: y^+ Distribution for Post-intervention state, Mesh No. 1, Time Step = $0.8E-6$ s - y^+ ranges from 0 to 1 in all the images presented here.

Appendix C

Maximum Courant Number

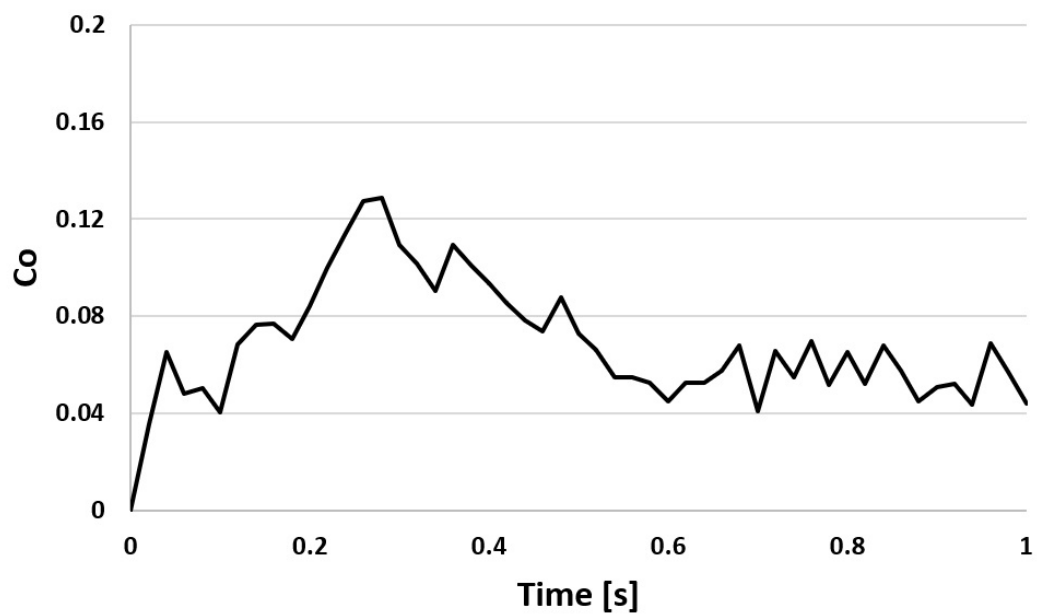


Figure C.1: Maximum Co for Pre-intervention state, Mesh No. 1, Time Step = 0.8E-6 s

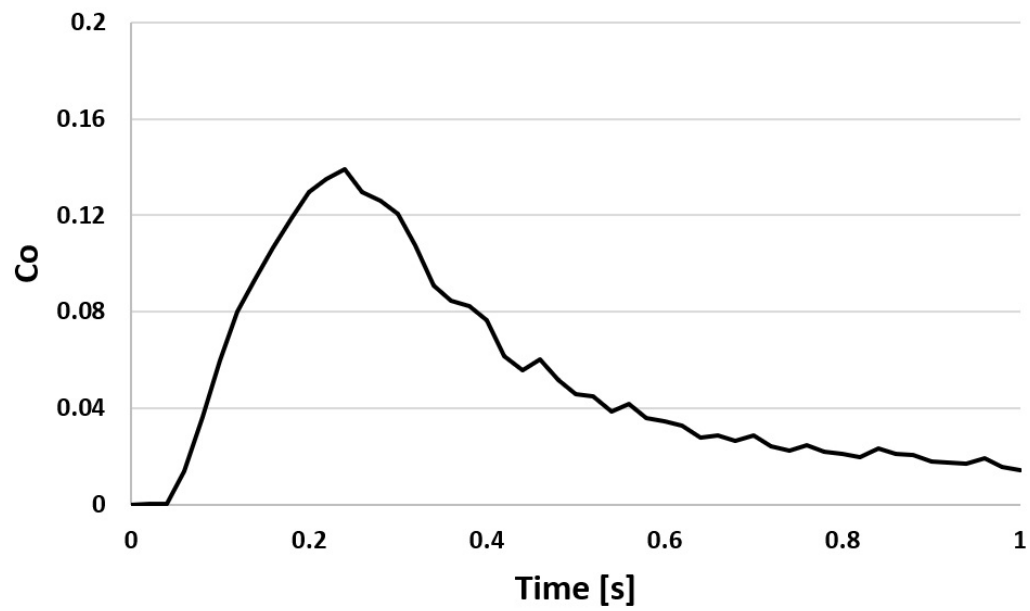


Figure C.2: Maximum Co for Post-intervention state, Mesh No. 1, Time Step = $0.8E-6$ s

Bibliography

- [1] João Janela, Alexandra Moura, and Adélia Sequeira. A 3d non-newtonian fluid–structure interaction model for blood flow in arteries. *Journal of Computational and applied Mathematics*, 234(9):2783–2791, 2010.
- [2] AD Caballero and S Laín. A review on computational fluid dynamics modelling in human thoracic aorta. *Cardiovascular Engineering and Technology*, 4(2):103–130, 2013.
- [3] Charalambos Vlachopoulos, Michael O’Rourke, and Wilmer W Nichols. *McDonald’s blood flow in arteries: theoretical, experimental and clinical principles*. CRC press, 2011.
- [4] Suzie Brown. *Computational Fluid Dynamic Modeling of Aortic Blood Flow*. PhD thesis, 2014.
- [5] L Morris, P Delassus, A Callanan, M Walsh, F Wallis, P Grace, and T McGloughlin. 3-d numerical simulation of blood flow through models of the human aorta. *Journal of biomechanical engineering*, 127(5):767–775, 2005.

- [6] N Shahcheraghi, HA Dwyer, AY Cheer, AI Barakat, and T Rutaganira. Unsteady and three-dimensional simulation of blood flow in the human aortic arch. *J. Biomech. Eng.*, 124(4):378–387, 2002.
- [7] Lijian Xu, Lekang Yin, Youjun Liu, and Fuyou Liang. A computational study on the influence of aortic valve disease on hemodynamics in dilated aorta. *Mathematical biosciences and engineering: MBE*, 17(1):606–626, 2019.
- [8] Loke Kok Foong, Majid Zarringhalam, Davood Toghraie, Niloufar Izadpanahi, Shu-Rong Yan, and Sara Rostami. Numerical study for blood rheology inside an artery: The effects of stenosis and radius on the flow behavior. *Computer methods and programs in biomedicine*, 193:105457, 2020.
- [9] Davood Toghraie, Navid Nasajpour Esfahani, Majid Zarringhalam, Nima Shirani, and Sara Rostami. Blood flow analysis inside different arteries using non-newtonian sisko model for application in biomedical engineering. *Computer Methods and Programs in Biomedicine*, 190:105338, 2020.
- [10] Loke Kok Foong, Nima Shirani, Davood Toghraie, Majid Zarringhalam, and Masoud Afrand. Numerical simulation of blood flow inside an artery under applying constant heat flux using newtonian and non-newtonian approaches for biomedical engineering. *Computer Methods and Programs in Biomedicine*, 190:105375, 2020.
- [11] Jie Chen and Xi-Yun Lu. Numerical investigation of the non-newtonian pulsatile blood flow in a bifurcation model with a non-planar branch. *Journal of biomechanics*, 39(5):818–832, 2006.

- [12] Nigel B Wood, Simon J Weston, Philip J Kilner, A David Gosman, and David N Firmin. Combined mr imaging and cfd simulation of flow in the human descending aorta. *Journal of Magnetic Resonance Imaging: An Official Journal of the International Society for Magnetic Resonance in Medicine*, 13(5):699–713, 2001.
- [13] Armin Leuprecht, Sebastian Kozerke, Peter Boesiger, and Karl Perktold. Blood flow in the human ascending aorta: a combined mri and cfd study. *Journal of engineering mathematics*, 47(3-4):387–404, 2003.
- [14] C Alberto Figueroa, Irene E Vignon-Clementel, Kenneth E Jansen, Thomas JR Hughes, and Charles A Taylor. A coupled momentum method for modeling blood flow in three-dimensional deformable arteries. *Computer methods in applied mechanics and engineering*, 195(41-43):5685–5706, 2006.
- [15] Feng GAO, Zhihong GUO, Masahiro WATANABE, and Teruo MATSUZAWA. Loosely coupled simulation for aortic arch model under steady and pulsatile flow. *Journal of Biomechanical Science and Engineering*, 1(2):327–341, 2006.
- [16] Joan M Greve, Andrea S Les, Beverly T Tang, Mary T Draney Blomme, Nathan M Wilson, Ronald L Dalman, Norbert J Pelc, and Charles A Taylor. Allometric scaling of wall shear stress from mice to humans: quantification using cine phase-contrast mri and computational fluid dynamics. *American Journal of Physiology-Heart and Circulatory Physiology*, 291(4):H1700–H1708, 2006.
- [17] Ryan L Spilker, Jeffrey A Feinstein, David W Parker, V Mohan Reddy, and Charles A Taylor. Morphometry-based impedance boundary conditions for

- patient-specific modeling of blood flow in pulmonary arteries. *Annals of biomedical engineering*, 35(4):546–559, 2007.
- [18] Manosh C Paul, Md Mamun Molla, and Giles Roditi. Large-eddy simulation of pulsatile blood flow. *Medical engineering & physics*, 31(1):153–159, 2009.
- [19] FPP Tan, A Borghi, RH Mohiaddin, NB Wood, S Thom, and XY Xu. Analysis of flow patterns in a patient-specific thoracic aortic aneurysm model. *Computers & Structures*, 87(11-12):680–690, 2009.
- [20] Z Cheng, FPP Tan, CV Riga, CD Bicknell, MS Hamady, RGJ Gibbs, NB Wood, and XY Xu. Analysis of flow patterns in a patient-specific aortic dissection model. *Journal of biomechanical engineering*, 132(5), 2010.
- [21] Chih-Yung Wen, An-Shik Yang, Li-Yu Tseng, and Jyh-Wen Chai. Investigation of pulsatile flowfield in healthy thoracic aorta models. *Annals of biomedical engineering*, 38(2):391–402, 2010.
- [22] Zahra Keshavarz-Motamed, Julio Garcia, and Lyes Kadem. Mathematical, numerical and experimental study in the human aorta with coexisting models of bicuspid aortic stenosis and coarctation of the aorta. In *2011 Annual International Conference of the IEEE Engineering in Medicine and Biology Society*, pages 182–185. IEEE, 2011.
- [23] Jonas Lantz, Johan Renner, and Matts Karlsson. Wall shear stress in a subject specific human aorta—influence of fluid-structure interaction. *International Journal of Applied Mechanics*, 3(04):759–778, 2011.

- [24] AF Stalder, Z Liu, J Hennig, JG Korvink, KC Li, and M Markl. Patient specific hemodynamics: combined 4d flow-sensitive mri and cfd. In *Computational Biomechanics for Medicine*, pages 27–38. Springer, 2011.
- [25] Alistair G Brown, Yubing Shi, Alberto Marzo, Cristina Staicu, Isra Valverde, Philipp Beerbaum, Patricia V Lawford, and D Rodney Hose. Accuracy vs. computational time: translating aortic simulations to the clinic. *Journal of biomechanics*, 45(3):516–523, 2012.
- [26] Jonas Lantz, Roland Gårdhagen, and Matts Karlsson. Quantifying turbulent wall shear stress in a subject specific human aorta using large eddy simulation. *Medical engineering & physics*, 34(8):1139–1148, 2012.
- [27] Marco Midulla, Ramiro Moreno, Adil Baali, Ming Chau, Anne Negre-Salvayre, Franck Nicoud, Jean-Pierre Pruvo, Stephan Haulon, and Hervé Rousseau. Haemodynamic imaging of thoracic stent-grafts by computational fluid dynamics (cfd): presentation of a patient-specific method combining magnetic resonance imaging and numerical simulations. *European radiology*, 22(10):2094–2102, 2012.
- [28] Zahra Keshavarz-Motamed, Julio Garcia, and Lyes Kadem. Fluid dynamics of coarctation of the aorta and effect of bicuspid aortic valve. *PLoS one*, 8(8):e72394, 2013.
- [29] Philippe Reymond, Paolo Crosetto, Simone Deparis, Alfio Quarteroni, and Nikos Stergiopoulos. Physiological simulation of blood flow in the aorta: comparison of hemodynamic indices as predicted by 3-d fsi, 3-d rigid wall and 1-d models. *Medical engineering & physics*, 35(6):784–791, 2013.

- [30] Kwong Ming Tse, Rong Chang, Heow Pueh Lee, Siak Piang Lim, Sudhakar Kundapur Venkatesh, and Pei Ho. A computational fluid dynamics study on geometrical influence of the aorta on haemodynamics. *European Journal of Cardio-Thoracic Surgery*, 43(4):829–838, 2013.
- [31] Koichi Sugimoto, Yoshiharu Takahara, Kenji Mogi, Kenji Yamazaki, Ken’ichi Tsubota, Fuyou Liang, and Hao Liu. Blood flow dynamic improvement with aneurysm repair detected by a patient-specific model of multiple aortic aneurysms. *Heart and vessels*, 29(3):404–412, 2014.
- [32] Andrew Callington, Quan Long, Prashant Mohite, Andre Simon, and Tarun Kumar Mittal. Computational fluid dynamic study of hemodynamic effects on aortic root blood flow of systematically varied left ventricular assist device graft anastomosis design. *The Journal of thoracic and cardiovascular surgery*, 150(3):696–704, 2015.
- [33] Satoshi Numata, Keiichi Itatani, Keiichi Kanda, Kiyoshi Doi, Sachiko Yamazaki, Kazuki Morimoto, Kaichiro Manabe, Koki Ikemoto, and Hitoshi Yaku. Blood flow analysis of the aortic arch using computational fluid dynamics. *European Journal of Cardio-Thoracic Surgery*, 49(6):1578–1585, 2016.
- [34] Jiling Feng, Meiwen An, Sravanthi Sashikumar, and Weiyi Chen. 3d computational fluid dynamic modelling for pulsatile blood wave propagation in the event of car crash. *International journal of crashworthiness*, 22(4):394–400, 2017.
- [35] Sudharsan Madhavan and Erica M Cherry Kemmerling. The effect of inlet and outlet boundary conditions in image-based cfd modeling of aortic flow. *Biomedical engineering online*, 17(1):66, 2018.

- [36] Rodrigo M Romarowski, Adrien Lefieux, Simone Morganti, Alessandro Veneziani, and Ferdinando Auricchio. Patient-specific cfd modelling in the thoracic aorta with pc-mri–based boundary conditions: A least-square three-element windkessel approach. *International journal for numerical methods in biomedical engineering*, 34(11):e3134, 2018.
- [37] Mohamad Shukri Zakaria, Farzad Ismail, Masaaki Tamagawa, Ahmad Fazli Abdul Aziz, Surjatin Wiriadidjaja, Adi Azrif Basri, and Kamarul Arifin Ahmad. A cartesian non-boundary fitted grid method on complex geometries and its application to the blood flow in the aorta using openfoam. *Mathematics and Computers in Simulation*, 159:220–250, 2019.
- [38] Kathrin Bäumlner, Vijay Vedula, Anna M Sailer, Jongmin Seo, Peter Chiu, Gabriel Mistelbauer, Francis P Chan, Michael P Fischbein, Alison L Marsden, and Dominik Fleischmann. Fluid–structure interaction simulations of patient-specific aortic dissection. *Biomechanics and Modeling in Mechanobiology*, pages 1–22, 2020.
- [39] Liang Liang, Wenbin Mao, and Wei Sun. A feasibility study of deep learning for predicting hemodynamics of human thoracic aorta. *Journal of Biomechanics*, 99:109544, 2020.
- [40] Ramón Pons, A Guala, José F Rodríguez-Palomares, JC Cajas, Lydia Dux-Santoy, Gisela Teixidó-Tura, José Javier Molins, Mariano Vázquez, Arturo Evangelista, and Jordi Martorell. Fluid–structure interaction simulations outperform computational fluid dynamics in the description of thoracic aorta

- haemodynamics and in the differentiation of progressive dilation in marfan syndrome patients. *Royal Society Open Science*, 7(2):191752, 2020.
- [41] Reza Sadeghi, Seyedvahid Khodaei, Javier Ganame, and Zahra Keshavarz-Motamed. towards non-invasive computational-mechanics and imaging-based diagnostic framework for personalized cardiology for coarctation. *Scientific Reports*, 10(1):1–19, 2020.
- [42] Liam Swanson, Benjamin Owen, Amir Keshmiri, Amin Deyranlou, Thomas Aldersley, John Lawrenson, Paul Human, Rik De Decker, Barend Fourie, George Comititis, et al. A patient-specific cfd pipeline using doppler echocardiography for application in coarctation of the aorta in a limited resource clinical context. *Frontiers in Bioengineering and Biotechnology*, 8:409, 2020.
- [43] TJ Pedley. The fluid mechanics of large blood vessels, cambridge university press, cambridge, 1980.
- [44] WA Seed and NB Wood. Velocity patterns in the aorta. *Cardiovascular research*, 5(3):319–330, 1971.
- [45] Herman L Falsetti, Kenneth M Kiser, Gerald P Francis, and Edward R Belmore. Sequential velocity development in the ascending and descending aorta of the dog. *Circulation Research*, 31(3):328–338, 1972.
- [46] Daisuke Mori and Takami Yamaguchi. Computational fluid dynamics modeling and analysis of the effect of 3-d distortion of the human aortic arch. *Computer Methods in Biomechanics & Biomedical Engineering*, 5(3):249–260, 2002.

- [47] T Kim, AY Cheer, and HA Dwyer. A simulated dye method for flow visualization with a computational model for blood flow. *Journal of biomechanics*, 37(8):1125–1136, 2004.
- [48] Zhuo Cheng, Nigel B Wood, Richard GJ Gibbs, and Xiao Y Xu. Geometric and flow features of type b aortic dissection: initial findings and comparison of medically treated and stented cases. *Annals of biomedical engineering*, 43(1):177–189, 2015.
- [49] Patrick Segers, Nikos Stergiopoulos, and Nico Westerhof. Quantification of the contribution of cardiac and arterial remodeling to hypertension. *Hypertension*, 36(5):760–765, 2000.
- [50] Patrick Segers, Nikos Stergiopoulos, and Nico Westerhof. Relation of effective arterial elastance to arterial system properties. *American Journal of Physiology-Heart and Circulatory Physiology*, 282(3):H1041–H1046, 2002.
- [51] Patrick Segers, Nikos Stergiopoulos, Nico Westerhof, Patrick Wouters, Philippe Kolh, and Pascal Verdonck. Systemic and pulmonary hemodynamics assessed with a lumped-parameter heart-arterial interaction model. *Journal of engineering mathematics*, 47(3-4):185–199, 2003.
- [52] Damien Garcia, Paul JC Barenbrug, Philippe Pibarot, André LAJ Dekker, Frederik H van der Veen, Jos G Maessen, Jean G Dumesnil, and Louis-Gilles Durand. A ventricular-vascular coupling model in presence of aortic stenosis. *American Journal of Physiology-Heart and Circulatory Physiology*, 288(4):H1874–H1884, 2005.

- [53] David Tanné, Lyes Kadem, Régis Rieu, and Philippe Pibarot. Hemodynamic impact of mitral prosthesis-patient mismatch on pulmonary hypertension: an in silico study. *Journal of Applied Physiology*, 105(6):1916–1926, 2008.
- [54] Jan Engvall, Per Ask, Dan Loyd, and Bengt Wranne. Coarctation of the aorta—a theoretical and experimental analysis of the effects of a centrally located arterial stenosis. *Medical and Biological Engineering and Computing*, 29(3):291–296, 1991.
- [55] Jan Engvall, Matts Karlsson, Per Ask, Dan Loyd, Eva Nylander, and Bengt Wranne. Importance of collateral vessels in aortic coarctation: computer simulation at rest and exercise using transmission line elements. *Medical and Biological Engineering and Computing*, 32(1):S115–S122, 1994.
- [56] Hyun Jin Kim, Irene E Vignon-Clementel, C Alberto Figueroa, John F LaDisa, Kenneth E Jansen, Jeffrey A Feinstein, and Charles A Taylor. On coupling a lumped parameter heart model and a three-dimensional finite element aorta model. *Annals of biomedical engineering*, 37(11):2153–2169, 2009.
- [57] Mona Alimohammadi, Obiekezie Agu, Stavroula Balabani, and Vanessa Díaz-Zuccarini. Development of a patient-specific simulation tool to analyse aortic dissections: assessment of mixed patient-specific flow and pressure boundary conditions. *Medical engineering & physics*, 36(3):275–284, 2014.
- [58] Zahra Keshavarz-Motamed. A diagnostic, monitoring, and predictive tool for patients with complex valvular, vascular and ventricular diseases. *Scientific Reports*, 10(1):1–19, 2020.

- [59] Zahra Keshavarz-Motamed, Elazer R Edelman, Payam K Motamed, Julio Garcia, Nagib Dahdah, and Lyes Kadem. The role of aortic compliance in determination of coarctation severity: Lumped parameter modeling, in vitro study and clinical evaluation. *Journal of biomechanics*, 48(16):4229–4237, 2015.
- [60] Zahra Keshavarz-Motamed, Farhad Rikhtegar Nezami, Ramon A Partida, Kenta Nakamura, Pedro Vinícius Staziaki, Eyal Ben-Assa, Brian Ghoshhajra, Ami B Bhatt, and Elazer R Edelman. Elimination of transcoarctation pressure gradients has no impact on left ventricular function or aortic shear stress after intervention in patients with mild coarctation. *JACC: Cardiovascular Interventions*, 9(18):1953–1965, 2016.
- [61] Z Keshavarz-Motamed, J Garcia, N Maftoon, E Bedard, P Chetaille, and L Kadem. A new approach for the evaluation of the severity of coarctation of the aorta using doppler velocity index and effective orifice area: in vitro validation and clinical implications. *Journal of biomechanics*, 45(7):1239–1245, 2012.
- [62] Zahra Keshavarz-Motamed, Julio Garcia, Emmanuel Gaillard, Nima Maftoon, Giuseppe Di Labbio, Guy Cloutier, and Lyes Kadem. Effect of coarctation of the aorta and bicuspid aortic valve on flow dynamics and turbulence in the aorta using particle image velocimetry. *Experiments in fluids*, 55(3):1696, 2014.
- [63] Zahra Keshavarz-Motamed, Julio Garcia, Philippe Pibarot, E Larose, and Lyes Kadem. Modeling the impact of concomitant aortic stenosis and coarctation of the aorta on left ventricular workload. *Journal of biomechanics*, 44(16):2817–2825, 2011.
- [64] Zahra Keshavarz-Motamed, Seyedvahid Khodaei, Farhad Rikhtegar Nezami,

- Junedh M Amrute, Suk Joon Lee, Jonathan Brown, Eyal Ben-Assa, Tamara Garcia Camarero, Javier Ruano Calvo, Stephanie Sellers, et al. Mixed valvular disease following transcatheter aortic valve replacement: Quantification and systematic differentiation using clinical measurements and image-based patient-specific in silico modeling. *Journal of the American Heart Association*, 9(5):e015063, 2020.
- [65] Eyal Ben-Assa, Jonathan Brown, Zahra Keshavarz-Motamed, M Jose, Benjamin Leiden, Max Olender, Faouzi Kallel, Igor F Palacios, Ignacio Inglessis, Jonathan J Passeri, et al. Ventricular stroke work and vascular impedance refine the characterization of patients with aortic stenosis. *Science translational medicine*, 11(509):eaaw0181, 2019.
- [66] Zahra Keshavarz-Motamed, Julio Garcia, Emmanuel Gaillard, Romain Capoulade, Florent Le Ven, Guy Cloutier, Lyes Kadem, and Philippe Pibarot. Non-invasive determination of left ventricular workload in patients with aortic stenosis using magnetic resonance imaging and doppler echocardiography. *PLoS One*, 9(1):e86793, 2014.
- [67] Emilia Benevento, Abdelghani Djebbari, Zahra Keshavarz-Motamed, Renzo Cecere, and Lyes Kadem. Hemodynamic changes following aortic valve bypass: a mathematical approach. *PloS one*, 10(4):e0123000, 2015.
- [68] Jessica S Coogan, Jay D Humphrey, and C Alberto Figueroa. Computational simulations of hemodynamic changes within thoracic, coronary, and cerebral arteries following early wall remodeling in response to distal aortic coarctation. *Biomechanics and modeling in mechanobiology*, 12(1):79–93, 2013.

- [69] Jessica S Coogan, Frandics P Chan, John F LaDisa Jr, Charles A Taylor, Frank L Hanley, and Jeffrey A Feinstein. Computational fluid dynamic simulations for determination of ventricular workload in aortic arch obstructions. *The Journal of thoracic and cardiovascular surgery*, 145(2):489–495, 2013.
- [70] Paula Giménez Mínguez, Bart Bijmens, Gabriel Bernardino, Èric Lluch, Iris Soveral, Olga Gómez, and Patricia Garcia-Canadilla. Assessment of haemodynamic remodeling in fetal aortic coarctation using a lumped model of the circulation. In *International Conference on Functional Imaging and Modeling of the Heart*, pages 471–480. Springer, 2017.
- [71] Mehran Mirramezani and Shawn C Shadden. A distributed lumped parameter model of blood flow. *Annals of Biomedical Engineering*, pages 1–17, 2020.
- [72] Joong Yull Park, Chan Young Park, Chang Mo Hwang, Kyung Sun, and Byoung Goo Min. Pseudo-organ boundary conditions applied to a computational fluid dynamics model of the human aorta. *Computers in Biology and Medicine*, 37(8):1063–1072, 2007.
- [73] Paritosh Vasava, Payman Jalali, Mahsa Dabagh, and Pertti J Kolari. Finite element modelling of pulsatile blood flow in idealized model of human aortic arch: study of hypotension and hypertension. *Computational and Mathematical Methods in Medicine*, 2012, 2012.
- [74] Johan Renner, Dan Loyd, Toste Länne, and Matts Karlsson. Is a flat inlet profile sufficient for wss estimation in the aortic arch. *WSEAS Transactions on Fluid Mechanics*, 4(4):148–160, 2009.

- [75] Umberto Morbiducci, Raffaele Ponzini, Diego Gallo, Cristina Bignardi, and Giovanna Rizzo. Inflow boundary conditions for image-based computational hemodynamics: impact of idealized versus measured velocity profiles in the human aorta. *Journal of biomechanics*, 46(1):102–109, 2013.
- [76] Michael A Gropper, Ronald D Miller, Lars I Eriksson, Lee A Fleisher, Jeanine P Wiener-Kronish, Neal H Cohen, and Kate Leslie. *Miller’s Anesthesia, Chapter 36, Cardiovascular Monitoring*. Elsevier Health Sciences, 2019.
- [77] Selene Pirola, Baolei Guo, Claudia Menichini, Simone Saitta, Weiguo Fu, Zhihui Dong, and Xiao Yun Xu. 4-d flow mri-based computational analysis of blood flow in patient-specific aortic dissection. *IEEE Transactions on Biomedical Engineering*, 66(12):3411–3419, 2019.
- [78] Paul D Stein and Hani N Sabbah. Turbulent blood flow in the ascending aorta of humans with normal and diseased aortic valves. *Circulation research*, 39(1):58–65, 1976.
- [79] Hans Nygaard, Peter K Paulsen, J Michael Hasenkam, Erik M Pedersen, and Poul E Røvsing. Turbulent stresses downstream of three mechanical aortic valve prostheses in human beings. *The Journal of thoracic and cardiovascular surgery*, 107(2):438–446, 1994.
- [80] Leidulf Segadal and Knut Matre. Blood velocity distribution in the human ascending aorta. *Circulation*, 76(1):90–100, 1987.
- [81] RICHARD H Klipstein, DAVID N Firmin, S RICHARD Underwood, RS Rees,

- and DB Longmore. Blood flow patterns in the human aorta studied by magnetic resonance. *Heart*, 58(4):316–323, 1987.
- [82] Julio Garcia, Alex J Barker, and Michael Markl. The role of imaging of flow patterns by 4d flow mri in aortic stenosis. *JACC: Cardiovascular Imaging*, 12(2):252–266, 2019.
- [83] Susanne Schnell, Pegah Entezari, Riti J Mahadewia, S Chris Malaisrie, Patrick M McCarthy, Jeremy D Collins, James Carr, and Michael Markl. Improved semi-automated 4d-flow mri analysis in the aorta in patients with congenital aortic valve anomalies vs tricuspid aortic valves. *Journal of computer assisted tomography*, 40(1):102, 2016.
- [84] Thomas T Tsai, Marty S Schlicht, Khalil Khanafer, Joseph L Bull, Doug T Valassis, David M Williams, Ramon Berguer, and Kim A Eagle. Tear size and location impacts false lumen pressure in an ex vivo model of chronic type b aortic dissection. *Journal of vascular surgery*, 47(4):844–851, 2008.
- [85] Ikuo Fukuda, Shingo Fujimori, Kazuyuki Daitoku, Hideki Yanaoka, and Takao Inamura. Flow velocity and turbulence in the transverse aorta of a proximally directed aortic cannula: hydrodynamic study in a transparent model. *The Annals of thoracic surgery*, 87(6):1866–1871, 2009.
- [86] JAMES E Moore Jr, STEPHAN E Maier, DAVID N Ku, and PETER Boesiger. Hemodynamics in the abdominal aorta: a comparison of in vitro and in vivo measurements. *Journal of Applied Physiology*, 76(4):1520–1527, 1994.
- [87] Bin Xiao and Yuwen Zhang. Numerical simulation of pulsatile turbulent flow

- in tapering stenosed arteries. *International Journal of Numerical Methods for Heat & Fluid Flow*, 2009.
- [88] Hermann Schlichting and Klaus Gersten. *Boundary-layer theory*. Springer, 2017.
- [89] RM Nerem and WA Seed. An in vivo study of aortic flow disturbances. *Cardiovascular research*, 6(1):1–14, 1972.
- [90] Diego Gallo, Gianluca De Santis, Federica Negri, Daniele Tresoldi, Raffaele Ponzini, Diana Massai, MA Deriu, Patrick Segers, Benedict Verheghe, Giovanna Rizzo, et al. On the use of in vivo measured flow rates as boundary conditions for image-based hemodynamic models of the human aorta: implications for indicators of abnormal flow. *Annals of biomedical engineering*, 40(3):729–741, 2012.
- [91] S Pirola, Z Cheng, OA Jarral, DP O’Regan, JR Pepper, T Athanasiou, and XY Xu. On the choice of outlet boundary conditions for patient-specific analysis of aortic flow using computational fluid dynamics. *Journal of biomechanics*, 60:15–21, 2017.
- [92] Iman Borazjani, Liang Ge, and Fotis Sotiropoulos. High-resolution fluid–structure interaction simulations of flow through a bi-leaflet mechanical heart valve in an anatomic aorta. *Annals of biomedical engineering*, 38(2):326–344, 2010.
- [93] C Canstein, P Cachot, A Faust, AF Stalder, J Bock, A Frydrychowicz, J Küffer, J Hennig, and Michael Markl. 3d mr flow analysis in realistic rapid-prototyping

- model systems of the thoracic aorta: comparison with in vivo data and computational fluid dynamics in identical vessel geometries. *Magnetic Resonance in Medicine: An Official Journal of the International Society for Magnetic Resonance in Medicine*, 59(3):535–546, 2008.
- [94] W Fu, B Chu, Yu Chang, and A Qiao. Construction and analysis of human thoracic aorta based on ct images. In *World Congress on Medical Physics and Biomedical Engineering, September 7-12, 2009, Munich, Germany*, pages 322–325. Springer, 2009.
- [95] JF Mustard, EA Murphy, HC Rowsell, and HG Downie. Factors influencing thrombus formation in vivo. *The American journal of medicine*, 33(5):621–647, 1962.
- [96] JM Hasenkam, H Nygaard, M Giersiepen, H Reul, and H Stødkilde-Jørgensen. Turbulent stress measurements downstream of six mechanical aortic valves in a pulsatile flow model. *Journal of biomechanics*, 21(8):631–645, 1988.
- [97] JO Hinze. Turbulence mcgraw-hill book company. *Inc., New York, NY*, page 488, 1959.
- [98] JM Robertson and JF Herrick. Turbulence in blood flow. *Department of Theoretical and Applied Mechanics Report*, (401), 1975.
- [99] John KJ Li. Laminar and turbulent flow in the mammalian aorta: Reynolds number. *Journal of theoretical biology*, 135(3):409–414, 1988.
- [100] Daniel Hershey and Chi Soon Im. Critical reynolds number for sinusoidal flow of water in rigid tubes. *AIChE Journal*, 14(5):807–809, 1968.

- [101] Turgut Sarpkaya. Experimental determination of the critical reynolds number for pulsating poiseuille flow. 1966.
- [102] R Mittal, SP Simmons, and HS Udaykumar. Application of large-eddy simulation to the study of pulsatile flow in a modeled arterial stenosis. *J. Biomech. Eng.*, 123(4):325–332, 2001.
- [103] David N Ku. Blood flow in arteries. *Annual review of fluid mechanics*, 29(1):399–434, 1997.
- [104] WW Nichols, MF O’Rourke, and W Larry Kenney. McDonald’s blood flow in arteries: Theoretical, experimental and clinical principles, ed. 3, 1991.
- [105] Chi Wei Ong, Ian Wee, Nicholas Syn, Sheryl Ng, Hwa Liang Leo, Arthur Mark Richards, and Andrew MTL Choong. Computational fluid dynamics modeling of hemodynamic parameters in the human diseased aorta: A systematic review. *Annals of Vascular Surgery*, 63:336–381, 2020.
- [106] Farzan Ghalichi, Xiaoyan Deng, Alain De Champlain, Yvan Douville, Martin King, and Robert Guidoin. Low reynolds number turbulence modeling of blood flow in arterial stenoses. *Biorheology*, 35(4-5):281–294, 1998.
- [107] Sonu S Varghese and Steven H Frankel. Numerical modeling of pulsatile turbulent flow in stenotic vessels. *J. Biomech. Eng.*, 125(4):445–460, 2003.
- [108] J Ryval, AG Straatman, and DA Steinman. Two-equation turbulence modeling of pulsatile flow in a stenosed tube. *J. Biomech. Eng.*, 126(5):625–635, 2004.
- [109] AC Benim, A Nahavandi, A Assmann, D Schubert, P Feindt, and SH Suh.

- Simulation of blood flow in human aorta with emphasis on outlet boundary conditions. *Applied Mathematical Modelling*, 35(7):3175–3188, 2011.
- [110] Robert S Rogallo and Parviz Moin. Numerical simulation of turbulent flows. *Annual review of fluid mechanics*, 16(1):99–137, 1984.
- [111] Sonu S Varghese, Steven H Frankel, and Paul F Fischer. Modeling transition to turbulence in eccentric stenotic flows. *Journal of biomechanical engineering*, 130(1), 2008.
- [112] FPP Tan, NB Wood, G Tabor, and XY Xu. Comparison of les of steady transitional flow in an idealized stenosed axisymmetric artery model with a rans transitional model. *Journal of biomechanical engineering*, 133(5), 2011.
- [113] Roland Gårdhagen, Fredrik Carlsson, and Matts Karlsson. Large eddy simulation of pulsating flow before and after coa repair: Cfd for intervention planning. *Advances in Mechanical Engineering*, 7(2):971418, 2015.
- [114] Jonas Lantz and Matts Karlsson. Large eddy simulation of ldl surface concentration in a subject specific human aorta. *Journal of biomechanics*, 45(3):537–542, 2012.
- [115] Russell Ross and Laurence Harker. Hyperlipidemia and atherosclerosis. *Science*, 193(4258):1094–1100, 1976.
- [116] Henry F Hoff and William D Wagner. Plasma low density lipoprotein accumulation in aortas of hypercholesterolemic swine correlates with modifications in aortic glycosaminoglycan composition. *Atherosclerosis*, 61(3):231–236, 1986.

- [117] Jonas Lantz, Tino Ebbers, Jan Engvall, and Matts Karlsson. Numerical and experimental assessment of turbulent kinetic energy in an aortic coarctation. *Journal of biomechanics*, 46(11):1851–1858, 2013.
- [118] Magnus Andersson, Jonas Lantz, Tino Ebbers, and Matts Karlsson. Quantitative assessment of turbulence and flow eccentricity in an aortic coarctation: impact of virtual interventions. *Cardiovascular engineering and technology*, 6(3):281–293, 2015.
- [119] Suzie Brown, Jing Wang, Harvey Ho, and Stephen Tullis. Numeric simulation of fluid–structure interaction in the aortic arch. In *Computational Biomechanics for Medicine*, pages 13–23. Springer, 2013.
- [120] James S Lowe, Peter G Anderson, and Susan I Anderson. *Stevens & Lowe’s Human Histology-E-Book*. Elsevier Health Sciences, 2018.
- [121] Jeremy PT Ward and Roger WA Linden. *Physiology at a Glance*. John Wiley & Sons, 2017.
- [122] Paul A Iaizzo. *Handbook of cardiac anatomy, physiology, and devices*. Springer Science & Business Media, 2009.
- [123] DP Acharjya et al. A hybrid scheme for heart disease diagnosis using rough set and cuckoo search technique. *Journal of Medical Systems*, 44(1):27, 2020.
- [124] Neil Herring and David J Paterson. *Levick’s introduction to cardiovascular physiology*. CRC Press, 2018.
- [125] Irving P Herman. *Physics of the human body*. Springer, 2016.

- [126] Pornhatai Komutrattananont, Pasuk Mahakkanukrauh, and Srijit Das. Morphology of the human aorta and age-related changes: anatomical facts. *Anatomy & cell biology*, 52(2):109–114, 2019.
- [127] FRANK Cikach, MILIND Y Desai, ERIC E Roselli, and V Kalahasti. Thoracic aortic aneurysm: how to counsel, when to refer. *Cleve Clin J Med*, 85(6):481–492, 2018.
- [128] John K Triedman and Jane W Newburger. Trends in congenital heart disease: the next decade. *Circulation*, 133(25):2716–2733, 2016.
- [129] Timothy M Maus. Thoracic aorta. In *Essential Echocardiography*, pages 183–203. Springer, 2016.
- [130] Monica M Matsumoto and Ross Milner. Three stage hybrid approach for congenital aortic coarctation and bicuspid aortic valve with severe aortic stenosis in an adult patient. *EJVES short reports*, 45:26–29, 2019.
- [131] Christoph Sinning, Elvin Zengin, Rainer Kozlik-Feldmann, Stefan Blankenberg, Carsten Rickers, Yskert von Kodolitsch, and Evaldas Girdauskas. Bicuspid aortic valve and aortic coarctation in congenital heart disease—important aspects for treatment with focus on aortic vasculopathy. *Cardiovascular diagnosis and therapy*, 8(6):780, 2018.
- [132] Elles J Dijkema, Tim Leiner, and Heynric B Grotenhuis. Diagnosis, imaging and clinical management of aortic coarctation. *Heart*, 103(15):1148–1155, 2017.
- [133] Goncalo Cardoso, Miguel Abecasis, Rui Anjos, Marta Marques, Giovanna Koukoulis, Carlos Aguiar, and José Pedro Neves. Aortic coarctation repair

- in the adult. *Journal of Cardiac Surgery: Including Mechanical and Biological Support for the Heart and Lungs*, 29(4):512–518, 2014.
- [134] Trevor Huff and Kunal Mahajan. Anatomy, thorax, heart ductus arteriosus. In *StatPearls [Internet]*. StatPearls Publishing, 2019.
- [135] G Ottaviani and LM Buja. Congenital heart disease: pathology, natural history, and interventions. In *Cardiovascular pathology*, pages 611–647. Elsevier, 2016.
- [136] Zahra Keshavarz-Motamed. *Flow Dynamics in Human Aorta with Coexisting Models of Bicuspid Aortic Stenosis and Coarctation of the Aorta*. PhD thesis, Concordia University, 2011.
- [137] Leslie DeLong and Nancy W Burkhart. *General and oral pathology for the dental hygienist*. Jones & Bartlett Learning, 2020.
- [138] Bethany L Wisotzkey, Christoph P Hornik, Amanda S Green, and Piers CA Barker. Comparison of invasive and non-invasive pressure gradients in aortic arch obstruction. *Cardiology in the Young*, 25(7):1348, 2015.
- [139] Gerald R Marx and Hugh D Allen. Accuracy and pitfalls of doppler evaluation of the pressure gradient in aortic coarctation. *Journal of the American College of Cardiology*, 7(6):1379–1385, 1986.
- [140] RK Wyse, PJ Robinson, JE Deanfield, DS Tunstall Pedoe, and FJ Macartney. Use of continuous wave doppler ultrasound velocimetry to assess the severity of coarctation of the aorta by measurement of aortic flow velocities. *Heart*, 52(3):278–283, 1984.

- [141] L Swan, S Goyal, C Hsia, S Hechter, G Webb, and MA Gatzoulis. Exercise systolic blood pressures are of questionable value in the assessment of the adult with a previous coarctation repair. *Heart*, 89(2):189–192, 2003.
- [142] Philip A Araoz, Gautham P Reddy, Harold Tarnoff, Claude L Roge, and Charles B Higgins. Mr findings of collateral circulation are more accurate measures of hemodynamic significance than arm-leg blood pressure gradient after repair of coarctation of the aorta. *Journal of Magnetic Resonance Imaging*, 17(2):177–183, 2003.
- [143] Mehdi Ghaderian and Mojdeh Gheysari. Medium term follow up treatment of severe native coarctation of aorta using of balloon angioplasty in young infants less than one year’s age. *J Cardiol & Cardiovasc Ther*, 2(1):555580, 2016.
- [144] Pradyumna Agasthi, Sai Harika Pujari, Andrew Tseng, Joseph N Graziano, Francois Marcotte, David Majdalany, Farouk Mookadam, Donald J Hagler, and Reza Arsanjani. Management of adults with coarctation of aorta. *World Journal of Cardiology*, 12(5):167–191, 2020.
- [145] Ana Maria Gaca, James J Jagers, L Todd Dudley, and George S Bisset III. Repair of congenital heart disease: a primer—part 2. *Radiology*, 248(1):44–60, 2008.
- [146] Clarence Crafoord. Correction of aortic coarctation. *The Annals of thoracic surgery*, 30(3):300–302, 1980.
- [147] K Vossschulte. Plastic surgery of the isthmus in aortic isthmus stenosis. *Thoraxchirurgie*, 4(5):443, 1957.

- [148] John A Waldhausen. Repair of coarctation of the aorta with a subclavian flap. *J Thorac Cardiovasc Surg*, 51:532–533, 1966.
- [149] JAMES E Lock, Theresa Niemi, BA Burke, Stanley Einzig, and WILFRIDO R Castaneda-Zuniga. Transcutaneous angioplasty of experimental aortic coarctation. *Circulation*, 66(6):1280–1286, 1982.
- [150] JOHN L GIBBS. Treatment options for coarctation of the aorta, 2000.
- [151] Martin P O’Laughlin, Stanton B Perry, James E Lock, and Charles E Mullins. Use of endovascular stents in congenital heart disease. *Circulation*, 83(6):1923–1939, 1991.
- [152] Rachel D Torok, Michael J Campbell, Gregory A Fleming, and Kevin D Hill. Coarctation of the aorta. In *Diseases of the Aorta*, pages 111–125. Springer, 2019.
- [153] Raasti Naseem, Ligu Zhao, Yang Liu, and Vadim V Silberschmidt. Experimental and computational studies of poly-l-lactic acid for cardiovascular applications: recent progress. *Mechanics of Advanced Materials and Modern Processes*, 3(1):13, 2017.
- [154] Z Keshavarz-Motamed and L Kadem. 3d pulsatile flow in a curved tube with coexisting model of aortic stenosis and coarctation of the aorta. *Medical engineering & physics*, 33(3):315–324, 2011.
- [155] Costas C Hamakiotes and Stanley A Berger. Periodic flows through curved tubes: the effect of the frequency parameter. *Journal of Fluid Mechanics*, 210:353–370, 1990.

- [156] T Naruse and K Tanishita. Large curvature effect on pulsatile entrance flow in a curved tube: model experiment simulating blood flow in an aortic arch. 1996.
- [157] Moreno Cecconi, Marcello Manfrin, Alessandra Moraca, Raffaele Zanolì, Pier Luigi Colonna, Maria Grazia Bettuzzi, Stefano Moretti, Domenico Gabrielli, and Gian Piero Perna. Aortic dimensions in patients with bicuspid aortic valve without significant valve dysfunction. *The American journal of cardiology*, 95(2):292–294, 2005.
- [158] Tuija Poutanen, Tero Tikanoja, Heikki Sairanen, and Eero Jokinen. Normal aortic dimensions and flow in 168 children and young adults. *Clinical physiology and functional imaging*, 23(4):224–229, 2003.
- [159] Johan Svensson, Roland Gårdhagen, Einar Heiberg, Tino Ebbers, Dan Loyd, Toste Länne, and Matts Karlsson. Feasibility of patient specific aortic blood flow cfd simulation. In *International Conference on Medical Image Computing and Computer-Assisted Intervention*, pages 257–263. Springer, 2006.
- [160] Charles R White and John A Frangos. The shear stress of it all: the cell membrane and mechanochemical transduction. *Philosophical Transactions of the Royal Society B: Biological Sciences*, 362(1484):1459–1467, 2007.
- [161] Nitzan Resnick, Hava Yahav, Ayelet Shay-Salit, Moran Shushy, Shay Schubert, Limor Chen Michal Zilberman, and Efrat Wofovitz. Fluid shear stress and the vascular endothelium: for better and for worse. *Progress in biophysics and molecular biology*, 81(3):177–199, 2003.
- [162] Michael A Gimbrone Jr, James N Topper, Tobi Nagel, Keith R Anderson, and

- GUILLERMO GARCIA-CARDEÑA. Endothelial dysfunction, hemodynamic forces, and atherogenesis a. *Annals of the New York Academy of Sciences*, 902(1):230–240, 2000.
- [163] Lee J Frazin, Michael J Vonesh, Krishnan B Chandran, Tanya Shipkowitz, Adel S Yaacoub, and David D McPherson. Confirmation and initial documentation of thoracic and abdominal aortic helical flow: An ultrasound study. *ASAIO journal*, 42(6):951–956, 1996.
- [164] Philip J Kilner, Guang Z Yang, Raad H Mohiaddin, David N Firmin, and Donald B Longmore. Helical and retrograde secondary flow patterns in the aortic arch studied by three-directional magnetic resonance velocity mapping. *Circulation*, 88(5):2235–2247, 1993.
- [165] Mauro Grigioni, Carla Daniele, Umberto Morbiducci, Costantino Del Gaudio, Giuseppe D’Avenio, Antonio Balducci, and Vincenzo Barbaro. A mathematical description of blood spiral flow in vessels: application to a numerical study of flow in arterial bending. *Journal of Biomechanics*, 38(7):1375–1386, 2005.
- [166] DP Giddens, CK Zarins, and S Glagov. The role of fluid mechanics in the localization and detection of atherosclerosis. 1993.
- [167] Thomas A Hope and Robert J Herfkens. Imaging of the thoracic aorta with time-resolved three-dimensional phase-contrast mri: a review. In *Seminars in thoracic and cardiovascular surgery*, volume 20, pages 358–364. Elsevier, 2008.

- [168] Alex Frydrychowicz, Aurélien F Stalder, Maximilian F Russe, Jelena Bock, Simon Bauer, Andreas Harloff, Alexander Berger, Mathias Langer, Jürgen Hennig, and Michael Markl. Three-dimensional analysis of segmental wall shear stress in the aorta by flow-sensitive four-dimensional-mri. *Journal of Magnetic Resonance Imaging: An Official Journal of the International Society for Magnetic Resonance in Medicine*, 30(1):77–84, 2009.